



Faculteit Wetenschappen
Departement Fysica
Theorie van Kwantumsystemen en Complexe Systemen

**Microcavity polaritons in presence of a two-dimensional
electron gas**

**Microcaviteit polaritonen in aanwezigheid van een
tweedimensionaal elektronengas**

Proefschrift voorgelegd tot het behalen van de graad van
doctor in de Wetenschappen aan de Universiteit Antwerpen
te verdedigen door Maarten Baeten

Promotor: prof. dr. Michiel Wouters

Antwerpen, 15 July 2015

Members of the jury

- | | | |
|--------------------------------|---|----------------------------------|
| Prof. dr. Michiel Wouters | - | Universiteit Antwerpen |
| Prof. dr. Paul Scheunders | - | Universiteit Antwerpen |
| Prof. dr. Sabine Van Doorslaer | - | Universiteit Antwerpen |
| Prof. dr. Francois Peeters | - | Universiteit Antwerpen |
| Prof. dr. Ataç Imamoğlu | - | ETH Zürich |
| Prof. dr. Maxime Richard | - | Institut NÉEL-CNRS/UJF, Grenoble |

Summary

This theoretical work investigates the strong light-matter coupling between an optical mode inside a planar microcavity and an embedded doped quantum well. In particular, the properties of the resulting quasi particles, the (exciton or trion)-polaritons being a coherent superposition of a photon and exciton (trion), are studied as a function of electron density. Over the last decade, polaritons have attracted a lot of attention because of their strong optical non-linearity and their bosonic character. Initiated by the milestone experiment that realized a Bose-Einstein condensate of polaritons, much progress has been made on polaritons and their superfluid properties. More recently, the possibility for quantum information processing with polaritons is exploited and engineering microcavity polaritons to use them as a single photon source is of major interest. The thesis only focusses on the linear properties of the polaritons, meaning that polariton-polariton interactions are not considered here.

In the first introductory chapter, an historical survey through the many possibilities for realizing strong light-matter coupling is presented. We also give an overview of what kind of experiments have been performed on this systems to characterize the polaritons. The basic concepts and relevant quantities are presented to set the stage for more elaborate approaches used later on. In particular, we will introduce the microcavity, the quantum well and its elementary excitations, the exciton and trion. The exciton-polariton as a coupled two level is introduced in the planar microcavity set-up. Then, we put the focus on the addition of extra charge carriers inside the quantum well. Several interesting many-body effects, such as the Fermi edge singularity (FES) and Anderson Orthogonality Catastrophe (AOC) are briefly discussed to motivate this work. Chapter 2 discusses the polariton formation between an optical mode and a highly doped quantum well containing a quantum degenerate two-dimensional electron gas. Here, highly doped means that the average inter-electron distance is less than the exciton Bohr radius. The most difficult ingredient in describing the linear polariton properties turns out to be the calculation of the optical properties of the two-dimensional electron gas; due to the absorption of a photon, a valence band hole and conduction band electron are created within the quantum well. The valence band hole then acts as an attractive potential for all the electrons. Within some approximations, we compute the 2DEG optical susceptibility, fully taking into account the above mentioned many-body effects of the FES and AOC. In a second stage we couple the 2DEG with the electromagnetic field. The resulting eigenmodes of the coupled system are discussed and their single particle properties, such as the effective mass and the Rabi frequency are elucidated.

An important assumption in the second chapter is for the valence band hole to have infinite mass. The latter is generally not true and we use a perturbative calculation in chapter 3 to take into account this finite hole mass. The Mahan exciton will be introduced and we calculate a lowest order contribution in the Lindhard polarization of the 2DEG for the lifetime of the Mahan polaritons. In general, i.e. even without taking into account the finite mass, the results in this chapter will be accurate if the Fermi time exceeds the period of the Rabi oscillations. When lowering the electron density, there will be a regime in which the average electron distance exceeds the exciton Bohr radius. The exciton can then be described as a single bosonic entity, from which the electrons can scatter. Chapter 4 introduces this effective description of the

exciton and the trion quasiparticle as an electron bound to an exciton. Again, the 2DEG optical susceptibility is computed within this particular model and we investigate the trion-polariton, being the coherent superposition of the optical mode inside the cavity and the trion inside the quantum well. It will be shown that this model captures some major experimentally observed features such as the transfer of oscillator strength and asymmetric lineshapes. The coupling with the photon field is then discussed. We also focus on the spatial structure ('the size') of the trionic component in the trion-photon superposition as a function of Fermi energy and Rabi frequency. The latter is an important quantity to set the stage for further research on polariton-polariton interactions, where it was pointed out that the electrons could enhance the polariton interaction strength. By computing the size of the trion, we obtain a first estimate of how polaritons could interact in presence of a 2DEG.

Contents

1	Introduction	9
1.1	Historical overview	9
1.2	Microcavity	10
1.2.1	Effective photon mass	11
1.2.2	Q-factor and photon lifetime	12
1.3	Semiconductor quantum well	12
1.4	Hamiltonian of the coupled system	15
1.5	Exciton-polariton for an empty quantum well: coupled two-level system	16
1.6	Doped quantum well	19
1.6.1	Non-interacting 2DEG	19
1.6.2	Fermi sea	20
1.6.3	Excited Fermi sea	21
1.6.4	Fermi edge singularity	21
1.6.5	Trion quasiparticle	21
1.7	Research question	22
2	Exciton-polaritons in presence of a non-interacting 2DEG	25
2.1	Kubo's linear response theory and general susceptibility	25
2.2	2DEG optical response: quench dynamics	26
2.2.1	Exact result for the optical response: Combescot and Nozières	28
2.2.2	Short time behaviour $t\varepsilon_F \ll 1$ and Elliot formula for absorption	30
2.3	2DEG optical response: model potential and results	31
2.4	Polariton as 'dressed photon'	35
2.4.1	Dyson series	35
2.4.2	Two-level system revisited	37
2.5	Polariton properties in a highly degenerate 2DEG	38
2.5.1	Polariton energies and linewidth	38
2.5.2	Rabi splitting vs density	40
2.5.3	Spectral weights	42
2.5.4	Lower polariton effective mass	42
3	Finite hole mass: recoil effects	45
3.1	Determinants by means of Feynman diagrams	45
3.2	Wannier equation	46
3.2.1	Ladder diagrams	46
3.2.2	Variational ansatz	49
3.2.3	Validity of the result	50
3.3	Mahan exciton	51
3.4	Valence band hole recoil and the lifetime of 'Mahan polaritons'	52

4	The trion-polariton	57
4.1	Optical response using an effective trion model	57
4.1.1	Hamiltonian	57
4.1.2	Optical absorption in the zero angular momentum channel	58
4.1.3	Oscillator strength	61
4.1.4	Higher angular momentum channels	62
4.1.5	Finite temperature	64
4.2	Trion-polariton	64
4.3	Spatial structure of the lower trion-polariton: towards the polariton blockade . .	66
5	Closing	71
5.1	Conclusion and outlook	71
5.2	Scientific contributions	72
A	Angular-momentum basis for the optical susceptibility	75
A.1	Matrix $\lambda_{\mathbf{k}\mathbf{q}}(t)$ in angular momentum basis	75
A.2	Light-matter coupling in the electron-hole basis	76
B	Dynamical self energy for the valence band hole	79
C	Stationary electron distribution in the lower trion-polariton state	83
	Nederlandstalige samenvatting	87
	Bibliography	88

Chapter 1

Introduction

This first chapter has the goal of introducing the basic concepts and quantities needed to understand the physics of light-matter coupling. They will be illustrated with the simplest model of an empty quantum well embedded in a planar microcavity. We introduce the experimental structures (from a theorist's viewpoint) of a microcavity and a quantum well. The elementary excitations in a quantum well are discussed and the important many-body physics of the Fermi edge singularity and Anderson Orthogonality Catastrophe, inherent in a quantum degenerate electron gas is shortly discussed. The overall formalism for describing many-electron wave functions is also given. But first things first, to appreciate the relevance of the thesis and putting it in a broader context, we start with a short historical survey on the subject of light-matter coupling.

1.1 Historical overview

An excited atom in free space will return to its ground state by spontaneous emission of photons, where the rate of emission is governed by the coupling of the atom with the continuum of modes of the electromagnetic field. Already in 1946, Purcell [1] discovered that putting the very same atom inside a cavity could seriously alter the spontaneous emission rate of the atom, and thus the coupling with the electromagnetic field ('light-matter coupling'). Eventually, if one has a cavity in which the photon lifetime is larger than the atomic emission rate, the photon gets absorbed and emitted a few times by the atom before leaving the cavity. Then, the system is said to be in the so-called strong coupling regime. The new eigenmodes inside the cavity, which are now hybrid light-matter excitations, are the so-called polaritons.

The theoretical concept of a polariton has been introduced in a seminal paper by Hopfield in 1958 [2], who calculated the optical modes propagating through a bulk crystal. There, the eigenmodes were shown to be a coherent superposition of a photon and an exciton in the crystal, a (three-dimensional) exciton-polariton. Naively, one might expect absorption due to the creation of excitons, but this is not true due to the formation of polaritons, which is quite counterintuitive. It lasted until 1973 to experimentally verify their existence in bulk GaAs [3]. The discovery of Purcell actually set the stage for the so-called cavity quantum electrodynamics experiments. These experiments are composed of an interacting electromagnetic field and any electronic system (atom, semiconductor, ...) in a regime in which the quantum nature of the excitations is important. The strong coupling regime with Rydberg atoms inside a cavity has been realized in Refs. [4, 5] and recently, the physics Nobelprize has been rewarded to S. Haroche [6] for his cavity QED experiments and corresponding quantum non-demolition measurements: by sending Rydberg atoms through the cavity, the optical mode is not destroyed but the change in the Rydberg state, due to the interaction with the photon, contains information on the optical mode. In this way, Haroche was able to construct and detect Schrödinger cat

states.

It is a well-known property of low-dimensional systems that they strongly increase the binding energy of bound states as compared to higher dimensional structures. This makes lower-dimensional semiconductor structures very interesting for studying optical properties, because the excitations are stable at higher temperatures and thus easier to observe. The coupling with the photon field and the observation of polaritons in a two-dimensional semiconductor microcavity has been performed for the first time by Weisbuch in 1993 [7]. By confining the electromagnetic field inside a pair of Bragg mirrors, forming a microcavity, and putting a quantum well inside, the formation of two-dimensional microcavity polaritons was achieved. Since then, strong coupling has been realized in many differently engineered configurations, such as one-dimensional microwires [8, 9], zero-dimensional micropillars [10] and quantum dots embedded inside a photonic crystal [11]. Nowadays, the most artificial analogon of the previous systems is offered by the circuit QED experiments [12, 13]. Besides working in another part of the electromagnetic spectrum (microwaves vs (near)-infrared), these experiments form a nice example for quantum information processing and are promising candidates for future quantum computation.

Within the planar microcavity set-up only, many different experiments have been carried out by changing one or more parameters to the original system. Different anorganic semiconductor materials (e.g. GaAs, ZnO, CdTe, ...) are used to increase the exciton binding energy, as well as organic quantum wells in which the elementary excitations are Frenkel excitons (localized) as compared to Wannier excitons (delocalized) [14, 15]. The polariton properties have been modified by putting stress on the quantum well [16], adding extra charge carriers in the quantum well [17, 18, 19] and eventually put it in a magnetic field [20, 21]. Placing the polaritons in a periodic in-plane potential results in the formation of bloch bands for the polariton dispersion [22].

Increasing the laser intensity opened the door towards the non-linear regime in which polaritons interactions start to become significant [23, 24, 25]. A very appealing feature of microcavity polaritons is their strong optical nonlinearity, allowing the creation of an interacting polariton quantum ‘fluid’. Several interesting effects due to polariton interactions include the formation of a polariton superfluid [26] and the formation of quantized vortices [27], parametric scattering [28, 29] and many others. In particular, a solid state equivalent of a Bose-Einstein condensate of polaritons in a planar microcavity has been realized in the milestone experiment by Kaspzrak *et al.* in 2006 [30]. Bose-Einstein condensation of polaritons and their superfluid properties have been investigated in detail both experimentally and theoretically [31]. Many experiments nowadays try to realize the polariton blockade [32], but in the current state of the art microcavities the single photon nonlinearities are too weak in order to enter this polariton blockade regime. Recently, a Feshbach resonance mechanism for enhancing the polariton interactions has been investigated [33]. Hopefully, this could lead one day to the microcavity-quantum well system as a single photon source [34, 35].

1.2 Microcavity

Throughout this work we will investigate the polaritons in a planar microcavity embedding a quantum well, see Fig. 1.1. First, the system contains a microcavity, basically consisting of a pair of two distributed Bragg reflectors. They are placed micrometers apart from each other, i.e. of the order of the wave length of visible/(near)-infrared light. Both mirrors can be either dielectric or metallic. The allowed photon modes inside the cavity have to form standing waves along the z -direction, i.e. perpendicular to the mirrors. Their energies can therefore only yield discrete values. If the energy separation between the mode of interest and the next mode is larger than any other energy scale of relevance in the system, spatial confinement effects in the

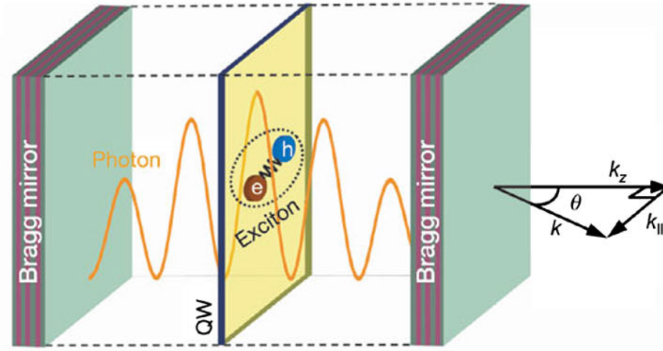


Figure 1.1: Strong light-matter coupling in a system containing a microcavity embedding a quantum well. The system oscillates coherently between the state with a photon in the microcavity and the state with an exciton in the quantum well. Figure taken from Ref. [30].

z -direction occur. In the planar direction, however, there is no confinement and we have a continuum of energy states.

1.2.1 Effective photon mass

Because of the confinement, the photon now acquires an effective mass. To have standing waves inside the cavity, the wave length λ_c of the photon should satisfy

$$\frac{n\lambda_c}{2} = d,$$

if d is the distance between the mirrors and $n \in \mathbb{N}$. Writing wavelengths in terms of wavenumbers we obtain

$$k_z = \frac{n\pi}{d}.$$

The energy $\varepsilon^{(\text{cav})}$ of a cavity mode with momentum \mathbf{k} is given by

$$\begin{aligned} \varepsilon_{\mathbf{k}}^{(\text{cav})} &= \hbar c |\mathbf{k}| \\ &= \hbar c \sqrt{k_z^2 + \mathbf{k}_{\parallel}^2} \end{aligned}$$

where \mathbf{k}_{\parallel} is the component of the momentum vector parallel with the mirrors ('in-plane momentum') and c is the speed of light in the material. Combining the above expressions and assuming $k_{\parallel} \ll k_z$, we immediately obtain

$$\varepsilon_{\mathbf{k}_{\parallel}}^{(\text{cav})} = m_c c^2 + \frac{\hbar^2 k_{\parallel}^2}{2m_c}. \quad (1.1)$$

The latter is a quadratic dispersion as a function k_{\parallel} . The effective photon mass is given by

$$m_c = n \frac{\pi \hbar}{cd}. \quad (1.2)$$

In an experiment the number of nodes n is fixed and the z -component of the photon field is frozen in. The relevant degrees of freedom are now the in-plane components of the momentum, which makes the photon field an effective two-dimensional field in this set-up.

1.2.2 Q-factor and photon lifetime

Another quantity that characterizes the microcavity is determined by asking the following question: ‘how many times does the photon bounces back and forth between the mirrors before it gets lost?’ Because the mirrors are not perfect, it will happen that after a while the photon does not reflect onto a mirror but rather passes through and thus leaves the cavity. The dimensionless number for quantifying this, is the so-called quality factor (Q -factor) of the cavity, defined as

$$Q = \frac{\omega_c}{\gamma_c}.$$

Here, ω_c is the resonant frequency of the cavity, i.e. the frequency at which a standing wave inside the cavity is formed and γ_c is the linewidth of the resonance. The latter is proportional to the inverse lifetime τ_c (time the photon stays inside the cavity) of the photon mode, i.e. $\tau_c \sim \gamma_c^{-1}$. In experiments, the cavity linewidth is determined by examining the absorption spectrum of the cavity. In this work, which will be of theoretical nature, we will use for the cavity lifetime some given number, compatible with experimentally obtained values.

If the mirrors were to be perfectly reflective one would have $\gamma_c = 0$ and a quality factor of $Q = \infty$. The photon would then stay infinitely long inside the cavity. However, in practice, the mirrors are leaky and the loss of photons is inevitable. Current state-of-the art microcavities have a photon lifetime ranging from 1ps [36] for the worst cavities to several 100ps for the best GaAs microcavities [37, 38]. With the help of Planck’s formula we can introduce the typical time and energy scales in polariton physics. From

$$t = \frac{\hbar}{E},$$

one finds that a linewidth of 1meV corresponds to a lifetime of about 0,65ps. In the best microcavities with a lifetime of 100ps, one immediately finds using the inverse relation, that the linewidth of the corresponding resonance is approximately 6,5 μ eV.

The number to remember is that it typically takes a few picoseconds before the photon is lost! This is very important to notice, in particular if one wants to have permanently some photons inside the cavity, for example to make a Bose-Einstein condensate of polaritons [30]. Then, one needs to actively pump photons into the system, making it a truly non-equilibrium system, because it needs to be pumped and it has radiative losses through the mirrors.

1.3 Semiconductor quantum well

Now, a semiconductor quantum well can be placed inside the cavity. A semiconductor quantum well (QW) is a semiconductor structure serving to restrict the degrees of freedom of charge carriers in the well to a planar direction, making the system quasi two-dimensional. A common way to make these QW’s is by evaporating different semiconductor materials on top of each other. For example, a widely used structure is AlAs-GaAs-AlAs, put on top of each other in the z -direction, see Fig. 1.2. Because GaAs has a smaller bandgap than AlAs, an effective potential well inside the GaAs is formed (blue solid lines) [39]. If the width of the GaAs layer is comparable to the de Broglie wave length of the charge carriers, the effective potential only allows for discrete states (blue dashed lines). Again, the z -component of charge carriers is frozen and their motion inside the semiconductor structure has effectively become two-dimensional.

The QW is placed in one of the anti-nodes of the photon field, where its amplitude is largest. This is done in order to induce the strongest possible coupling between the photon and the QW. The lowest energy excitation in the QW consists of a valence band hole and a conduction band electron, bound with each other through the Coulomb interaction. This is called an exciton

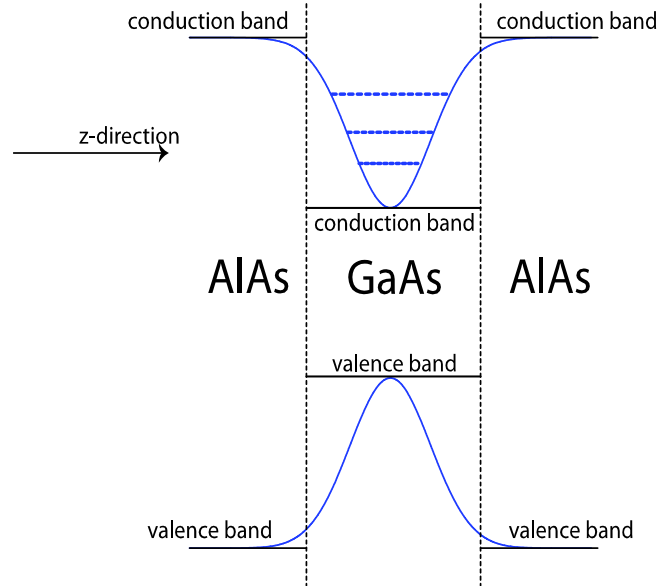


Figure 1.2: Stacking several semiconductor materials with different bandgaps allows for the creation of a quantum well. In this example, the electron motion in the z -direction gets quantized, resulting in discrete energy levels, if the width of the GaAs layer is comparable to the de Broglie wave length of the electrons.

and it corresponds to a hydrogenlike atom in the $1s$ state. The exciton states correspond to the solution of the stationary Schrödinger equation for the electron-hole pair,

$$H_X(\mathbf{r}_e, \mathbf{r}_h) \Psi(\mathbf{r}_e, \mathbf{r}_h) = \varepsilon_X \Psi(\mathbf{r}_e, \mathbf{r}_h)$$

with

$$H_X(\mathbf{r}_e, \mathbf{r}_h) = -\frac{\hbar^2}{2m_e^*} \Delta_{\mathbf{r}_e} - \frac{\hbar^2}{2m_h^*} \Delta_{\mathbf{r}_h} - \frac{e^2}{4\pi\varepsilon |\mathbf{r}_e - \mathbf{r}_h|}.$$

Defining the center of mass coordinate \mathbf{R} and relative coordinate \mathbf{r} as

$$\begin{aligned} \mathbf{R} &= \frac{m_e^* \mathbf{r}_e + m_h^* \mathbf{r}_h}{m_e^* + m_h^*} \\ \mathbf{r} &= \mathbf{r}_e - \mathbf{r}_h, \end{aligned}$$

we obtain for the Hamiltonian in the new variables

$$H_X(\mathbf{R}, \mathbf{r}) = -\frac{\hbar^2}{2M} \Delta_{\mathbf{R}} - \frac{\hbar^2}{2\mu^*} \Delta_{\mathbf{r}} - \frac{e^2}{4\pi\varepsilon |\mathbf{r}|},$$

where $M = m_e^* + m_h^*$ is the exciton mass and $1/\mu^* = 1/m_e^* + 1/m_h^*$ is the effective reduced mass of the electron-hole pair (with m^* being the band mass). The eigenstates of the Hamiltonian are given by

$$\Psi(\mathbf{R}, \mathbf{r}) = \frac{e^{i\mathbf{K}\mathbf{R}}}{\sqrt{S}} \psi_n(\mathbf{r}),$$

where the center of mass wave function is given by a plane wave normalized to the area of the system S and it has an energy $\varepsilon_{\text{COM}}(\mathbf{K}) = \frac{\hbar^2 K^2}{2M}$.

The bound state solutions in angular momentum and radial components are given by [40]

$$\psi_{n,m}(r, \theta) = \frac{1}{\sqrt{\mathcal{N}}} \frac{1}{(n - \frac{1}{2})^m} \times \left(\frac{r}{a_X}\right)^m \times e^{-\frac{r}{a_X} \frac{1}{2n-1}} \times L_{n-m-1}^{2m} \left(\frac{1}{n - \frac{1}{2}} \frac{r}{a_X}\right) \times \frac{e^{im\theta}}{\sqrt{2\pi}}. \quad (1.3)$$

	$\varepsilon/\varepsilon_0$	m_e^*/m_e	m_h^*/m_e	m_e^*/m_h^*	R_X [meV]	a_X [nm]	m_X/m_c
GaAs	12.9	0.067	0.34	0.20	18.3	6.1	$\sim 10^5$
CdTe	10.4	0.090	0.81	0.11	41	3.4	$\sim 10^5$
ZnO	8.0	0.280	0.59	0.47	160	1.1	$\sim 10^5$

Table 1.1: Material parameters for some semiconductor materials often used for microcavities.

Here, $n \geq 1$ is the principal quantum number, $m \in \{0, \pm 1, \pm 2, \dots, \pm(n-1)\}$ the azimuthal quantum number and $L_\alpha^\beta(x)$ the associated Laguerre polynomials. The normalization constant is $\mathcal{N} = 2 \left(n - \frac{1}{2}\right)^3 \frac{(n+m-1)!}{(n-m-1)!}$. Finally, the spectrum in units of the two-dimensional exciton Rydberg R_X is given by

$$\frac{\varepsilon_n}{R_X} = -\frac{1}{(2n-1)^2}.$$

There is a twofold difference with the usual hydrogen atom: First, there is a difference in dimensionality, as the exciton lives in a two-dimensional quantum well as compared to the usual three-dimensional hydrogen atom. Second, there is also a quantitative difference in the sense that the exciton Bohr radius and binding energy are renormalized with respect to vacuum, because of the effective dielectric constant of the semiconductor material and the effective bandmasses. In particular, we have

$$R_X = \frac{\hbar^2}{2\mu^* a_X^2} \quad (1.4)$$

and the effective Bohr radius is given by

$$a_X = \frac{2\pi\varepsilon\hbar^2}{e^2\mu^*}.$$

Here, ε is the dielectric constant of the semiconductor material. In table 1.1 the values for the exciton binding energy, Bohr radius and exciton mass are given for some semiconductor materials which are often used as microcavities [41]. Also the electron and heavy hole band mass (denoted with stars) are given in the table.

The photon mass for the different materials is calculated from Eq. (1.2) for a cavity with length $d = 2\mu\text{m}$ and $n = 1$, while the exciton mass was taken $m_X = m_e^* + m_h^*$. Since the lattice spacing in the above semiconductor materials is of the order of 0.1 nm, the exciton extends over multiple lattice sites within the material: these kind of excitons are called Wannier excitons (as opposed to Frenkel excitons, which are localized onto a single atom).

Also note that the definition of the two-dimensional Bohr radius is reduced by a factor of two as compared to the three-dimensional case. This means for the 1s binding energy

$$\frac{R_X}{R_X^{3D}} = 4.$$

Due to the confinement of the exciton motion to two dimensions, the binding energy has increased by a factor of 4 as compared to the bulk exciton binding energy.

Finally, note that if we want to speak about a well-defined exciton, we must ensure to work with temperatures much smaller than the exciton binding energy, such that thermal fluctuations cannot break up the electron-hole pair. Since we have $1\text{K} \sim 1\text{meV}$, we should have $T \ll 20\text{K}$ for GaAs which can be obtained by standard cooling techniques. Of course, for other materials such as ZnO one can afford to work with much higher temperatures, even room temperature, as the exciton binding energy is much larger. Throughout this work we will consider only zero temperature, unless mentioned otherwise.

1.4 Hamiltonian of the coupled system

We now have all the ingredients to describe the coupled microcavity - quantum well system. The Hamiltonian of the entire system is given by

$$\hat{H} = \hat{H}_{\text{QW}} + \hat{H}_{\text{photon}} + \hat{V}_{\text{LM}}.$$

The separate Hamiltonians for the two-dimensional quantum well, two-dimensional photon field and the coupling are respectively given by

$$\begin{aligned} \hat{H}_{\text{QW}} &= \sum_{\mathbf{k}} \varepsilon_{\mathbf{k}}^{(v)} \hat{b}_{\mathbf{k}}^{\dagger} \hat{b}_{\mathbf{k}} + \sum_{\mathbf{k}} \varepsilon_{\mathbf{k}}^{(c)} \hat{c}_{\mathbf{k}}^{\dagger} \hat{c}_{\mathbf{k}} - \sum_{\mathbf{K}, \mathbf{k}, \mathbf{Q}} V_{\mathbf{Q}}^C \hat{c}_{\mathbf{K}+\mathbf{Q}}^{\dagger} \hat{b}_{\mathbf{k}-\mathbf{Q}}^{\dagger} \hat{b}_{\mathbf{k}} \hat{c}_{\mathbf{K}} + \sum_{\mathbf{K}, \mathbf{k}, \mathbf{Q}} V_{\mathbf{Q}}^C \hat{c}_{\mathbf{K}+\mathbf{Q}}^{\dagger} \hat{c}_{\mathbf{k}-\mathbf{Q}}^{\dagger} \hat{c}_{\mathbf{k}} \hat{c}_{\mathbf{K}} \\ \hat{H}_{\text{photon}} &= \sum_{\mathbf{k}} \varepsilon_{\mathbf{k}}^{(\text{cav})} \hat{a}_{\mathbf{k}}^{\dagger} \hat{a}_{\mathbf{k}} \\ \hat{V}_{\text{LM}} &= \sum_{\mathbf{k}, \mathbf{q}} g_{\mathbf{k}} \hat{c}_{\mathbf{q}}^{\dagger} \hat{b}_{-\mathbf{q}+\mathbf{k}}^{\dagger} \hat{a}_{\mathbf{k}} + \text{h.c} \end{aligned}$$

with the proper (anti-)commutation relations given by

$$\begin{aligned} [\hat{a}_{\mathbf{k}}, \hat{a}_{\mathbf{q}}^{\dagger}] &= \delta_{\mathbf{k}\mathbf{q}} \\ \{\hat{c}_{\mathbf{k}}, \hat{c}_{\mathbf{q}}^{\dagger}\} &= \delta_{\mathbf{k}\mathbf{q}} \\ \{\hat{b}_{\mathbf{k}}, \hat{b}_{\mathbf{q}}^{\dagger}\} &= \delta_{\mathbf{k}\mathbf{q}}. \end{aligned}$$

The in-plane momentum \mathbf{k} is from now on implicitly assumed to be a two-dimensional vector, hence we do not longer write \mathbf{k}_{\parallel} . Both conduction band electrons and valence band holes (created with momentum \mathbf{k} and energy $\varepsilon_{\mathbf{k}}^{(c,v)}$ with creation operators $\hat{c}_{\mathbf{k}}^{\dagger}$ resp. $\hat{b}_{\mathbf{k}}^{\dagger}$) contribute to the total kinetic energy. We also have a Coulombic electron-hole interaction term and electron-electron interactions, with an amplitude given by the Fourier transform of the Coulomb interaction in real space:

$$\begin{aligned} V^C(\mathbf{q}) &= \int \frac{e^2}{4\pi\epsilon r} \frac{e^{i\mathbf{q}\mathbf{r}}}{\sqrt{S}} d^2r \\ &= \frac{e^2}{2\epsilon\sqrt{S}} \frac{1}{|\mathbf{q}|}. \end{aligned}$$

The Hamiltonian \hat{H}_{photon} represents the energy of the optical field inside the cavity, the dispersion for the photons being given by Eq. (1.1). The light-matter interaction term \hat{V}_{LM} couples both systems. As described in the previous section, the absorption of a photon with momentum \mathbf{k} goes together with the creation of interband electron-hole pair (with center of mass momentum \mathbf{k}). Because of translational symmetry, the in-plane momentum is a conserved quantity in the interaction. The amplitude for a photon to turn into an interband electron-hole pair is given by $g_{\mathbf{k}} = \langle c|\hat{\mathbf{d}}|v\rangle$, where $\hat{\mathbf{d}} = e\hat{\mathbf{r}}$ is the electrical dipole operator and $|c, v\rangle$ denote the conduction/valence band Bloch wave functions. Finally, we also add the hermitian conjugate of the light-matter interaction to the Hamiltonian, describing the reverse process in which an electron-hole pair recombines into a photon.

1.5 Exciton-polariton for an empty quantum well: coupled two-level system

The simplest description of the coupled quantum-well microcavity system starts by introducing the exciton as a bosonic quasiparticle. Let us define the creation operator $\hat{X}_{\mathbf{k}}$ for an exciton with center of mass momentum \mathbf{k} and energy $\varepsilon_{\mathbf{k}}^{(X)}$. If the density of excitons n_X is much smaller than the exciton Bohr radius, $n_X a_X^2 \ll 1$, we can treat the exciton as a bosonic particle, satisfying the commutation relation

$$[\hat{X}_{\mathbf{k}}, \hat{X}_{\mathbf{q}}^\dagger] = \delta_{\mathbf{k}\mathbf{q}}.$$

The Hamiltonian containing the optical field and the excitons is now given by

$$\hat{H} = \sum_{\mathbf{k}} \varepsilon_{\mathbf{k}}^{(\text{cav})} \hat{a}_{\mathbf{k}}^\dagger \hat{a}_{\mathbf{k}} + \sum_{\mathbf{k}} \varepsilon_{\mathbf{k}}^{(X)} \hat{X}_{\mathbf{k}}^\dagger \hat{X}_{\mathbf{k}} + \frac{\hbar\Omega_R}{2} \sum_{\mathbf{k}} \left(\hat{X}_{\mathbf{k}}^\dagger \hat{a}_{\mathbf{k}} + \hat{a}_{\mathbf{k}}^\dagger \hat{X}_{\mathbf{k}} \right) \quad (1.5)$$

$$= \sum_{\mathbf{k}} \begin{pmatrix} \hat{a}_{\mathbf{k}}^\dagger & \hat{X}_{\mathbf{k}}^\dagger \end{pmatrix} \begin{pmatrix} \varepsilon_c(\mathbf{k}) & \frac{\hbar\Omega_R}{2} \\ \frac{\hbar\Omega_R}{2} & \varepsilon_X(\mathbf{k}) \end{pmatrix} \begin{pmatrix} \hat{a}_{\mathbf{k}} \\ \hat{X}_{\mathbf{k}} \end{pmatrix}, \quad (1.6)$$

where the first two terms in the first line describe the energy of the photon field (created with $\hat{a}_{\mathbf{k}}^\dagger$) and excitons. The last term gives the coherent coupling between the exciton and the photon. From the matrix formulation one easily sees that the problem consists of two levels (exciton and photon) being coupled due to the off-diagonal terms. This Hamiltonian can be unitarily transformed to a new basis in which it becomes diagonal:

$$H = \sum_{j \in \{l, u\}} \sum_{\mathbf{k}} \varepsilon_j(\mathbf{k}) \hat{b}_{j, \mathbf{k}}^\dagger \hat{b}_{j, \mathbf{k}}$$

where the transformation has been performed, using two new operators $\hat{b}_{l, \mathbf{k}}$, $\hat{b}_{u, \mathbf{k}}$, given by

$$\hat{b}_{l, u, \mathbf{k}} = X_{l, u}(\mathbf{k}) \hat{X}_{\mathbf{k}} + a_{l, u}(\mathbf{k}) \hat{a}_{\mathbf{k}}. \quad (1.7)$$

The new quasiparticles, created with the operators $\hat{b}_{l, u}^\dagger$ correspond to a coherent superposition of matter degrees of freedom (the exciton) and a photonic component. These new hybrid light-matter quasiparticles are the so-called lower and upper exciton-polariton, labelled with indices resp. l and u . The operators \hat{b}^\dagger (\hat{b}) are called the polariton creation (annihilation) operators. The polariton dispersion relation is given by

$$\varepsilon_{u, l}(\mathbf{k}) = \frac{\varepsilon_{\mathbf{k}}^{(\text{cav})} + \varepsilon_{\mathbf{k}}^{(X)}}{2} \pm \frac{\sqrt{\left(\varepsilon_{\mathbf{k}}^{(\text{cav})} - \varepsilon_{\mathbf{k}}^{(X)}\right)^2 + \hbar^2 \Omega_R^2}}{2}. \quad (1.8)$$

where the \pm sign corresponds to the upper and lower polariton respectively. The polariton dispersion relations are shown in Fig. 1.3 for different exciton-photon detunings Δ at normal incidence (i.e. at $\mathbf{k} = \mathbf{0}$). As can be seen from the figure, the new eigenenergies show the typical avoided crossing, and the minimal splitting $\hbar\Omega_R$ is obtained when $\varepsilon_{\mathbf{k}}^{(\text{cav})} = \varepsilon_{\mathbf{k}}^{(X)}$. This is the so-called Rabi splitting. In the figure, the exciton has been assumed to have a flat dispersion, i.e. $\varepsilon_{\mathbf{k}}^{(X)} = \varepsilon_X$. This is justified because the exciton is a few order of magnitudes heavier than the photon, see table 1.1. As the band curvature is inversely proportional to the particle mass, an infinite heavy particle has a dispersion which is flat in momentum space.

The amplitudes $X_{l, u}(\mathbf{k})$ and $a_{l, u}(\mathbf{k})$ in the linear superposition Eq. (1.7) are the so-called Hopfield coefficients. They are given by

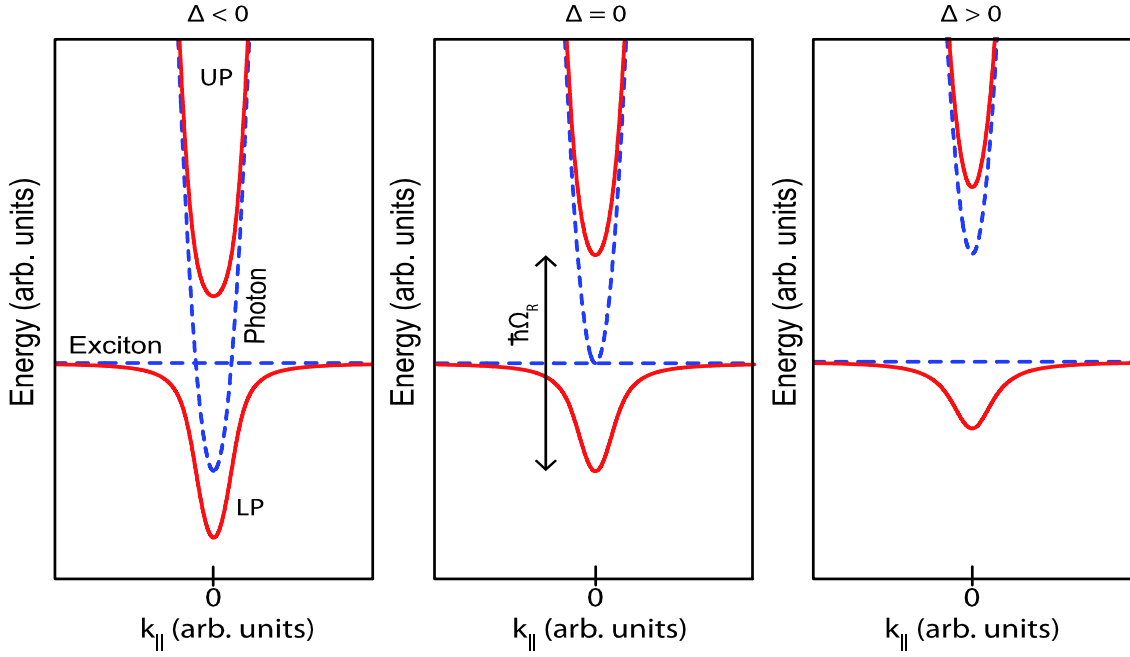


Figure 1.3: Dispersion relation of the uncoupled systems given by the dashed blue lines. Different panels depict different exciton-photon detunings $\Delta = \omega^{(\text{cav})}(\mathbf{k} = \mathbf{0}) - \omega^{(X)}(\mathbf{k} = \mathbf{0})$ at normal incidence. The light-matter interaction admixes the photon and exciton, resulting in a new dispersion relation for the lower and upper polariton (red solid lines). The latter clearly show the avoided crossing.

$$a_u(\mathbf{k}) = \frac{\varepsilon_{\mathbf{k}}^{(\text{cav})} - \varepsilon_{\mathbf{k}}^{(X)} + \sqrt{\left(\varepsilon_{\mathbf{k}}^{(\text{cav})} - \varepsilon_{\mathbf{k}}^{(X)}\right)^2 + 4\Omega_R^2}}{\sqrt{4\Omega_R^2 + \left(\varepsilon_{\mathbf{k}}^{(\text{cav})} - \varepsilon_{\mathbf{k}}^{(X)} + \sqrt{\left(\varepsilon_{\mathbf{k}}^{(\text{cav})} - \varepsilon_{\mathbf{k}}^{(X)}\right)^2 + 4\Omega_R^2}\right)^2}}$$

$$X_u(\mathbf{k}) = \frac{2\Omega_R}{\sqrt{4\Omega_R^2 + \left(\varepsilon_{\mathbf{k}}^{(\text{cav})} - \varepsilon_{\mathbf{k}}^{(X)} + \sqrt{\left(\varepsilon_{\mathbf{k}}^{(\text{cav})} - \varepsilon_{\mathbf{k}}^{(X)}\right)^2 + 4\Omega_R^2}\right)^2}}.$$

Furthermore, $a_l(\mathbf{k}) = -X_u(\mathbf{k})$ and $X_l(\mathbf{k}) = a_u(\mathbf{k})$.

The excitonic and photonic content in the polariton states is determined by $|X_{l,u}(\mathbf{k})|^2$ and $|a_{l,u}(\mathbf{k})|^2$, where due to normalization (unitary transformation) one has $|X_{u,l}(\mathbf{k})|^2 + |a_{u,l}(\mathbf{k})|^2 = 1$. If $\varepsilon_{\mathbf{k}}^{(\text{cav})} = \varepsilon_{\mathbf{k}}^{(X)}$, we have $a_u(\mathbf{k}) = 1/\sqrt{2} = X_u(\mathbf{k})$ and the polaritons are equal superpositions of exciton and photon.

We are now in a situation in which we can define the strong-coupling regime. Taking into account all possible losses, both for the photon (radiative losses through the mirrors) and the exciton (non-radiative decay, for example due to interaction with other charge carriers or phonons) we define the system to be in the strong-coupling regime when

$$\boxed{\text{Strong coupling: } \Omega_R \gg \gamma_c, \gamma_X}$$

with $\gamma_{c,X}$ the photon and exciton linewidth. The Rabi splitting thus should exceed all possible losses in the system. Only then, the system is said to be in the strong coupling regime and the

polaritons are the good quasi particles to describe the system.

Intuitively this means that there should be a high probability for the photon to be reabsorbed by the QW and turn into an exciton and vice versa. This is to be contrasted with the weak coupling, where the photon, once emitted due to electron-hole recombination of the exciton, will never be reabsorbed.

The polariton quasiparticles have several interesting properties which made them very attractive to investigate during the last decade. Below, we list some of the most appealing features of these intriguing particles

- *Polaritons are bosonic quasiparticles* as can be seen from the commutation relations:

$$\begin{aligned} \left[\hat{b}_{l,u}(\mathbf{k}), \hat{b}_{l,u}^\dagger(\mathbf{q}) \right] &= \left[X_{l,u}(\mathbf{k}) \hat{X}_{\mathbf{k}} + a_{l,u}(\mathbf{k}) \hat{a}_{\mathbf{k}}, X_{l,u}^*(\mathbf{q}) \hat{X}_{\mathbf{q}}^\dagger + a_{l,u}^*(\mathbf{q}) \hat{a}_{\mathbf{q}}^\dagger \right] \\ &= X_{l,u}(\mathbf{k}) X_{l,u}^*(\mathbf{q}) \left[\hat{X}_{\mathbf{k}}, \hat{X}_{\mathbf{q}}^\dagger \right] + a_{l,u}(\mathbf{k}) a_{l,u}^*(\mathbf{q}) \left[\hat{a}_{\mathbf{k}}, \hat{a}_{\mathbf{q}}^\dagger \right] \\ &= |X_{l,u}(\mathbf{k})|^2 \delta_{\mathbf{k},\mathbf{q}} + |a_{l,u}(\mathbf{k})|^2 \delta_{\mathbf{k},\mathbf{q}} \\ &= \delta_{\mathbf{k},\mathbf{q}} \end{aligned}$$

where we used $|X_{u,l}(\mathbf{k})|^2 + |a_{u,l}(\mathbf{k})|^2 = 1$, and we treated the excitons to be bosonic as well. The latter is true if the exciton density n_X satisfies $n_X a_X^2 \ll 1$.

- *Small effective mass*: because of the hybridization of the exciton with the photon, the lower polariton inherits the steep dispersion of the photon around $k_{\parallel} = 0$, see Fig. 1.3. This means that the lower polariton has a small effective mass. Together with the bosonic character, this has made the polaritons appropriate quasiparticles for realizing Bose-Einstein condensation in solid state systems, because a small mass tends to increase the temperature below which Bose-Einstein condensation is possible [22, 30, 37].
- *Polariton-polariton interactions* due to matter component: whereas in bulk/vacuum the effective cross section for the interaction between two photons is negligible, the planar microcavity set-up strongly increases the interaction strength between photons. This is due to the matter degree of freedom in the superposition, which has a much larger cross section for interaction. Polaritons interact via their matter component [25, 42, 43].
- *Direct measurement of polariton properties* due to their photonic component: for example, the dispersion relation for the polariton can be directly mapped onto the angle resolved detection of the photons coming out of the microcavity [44]. Another example is the measurement of the spatial correlation between the polaritons inside the cavity through the first order correlation function of the photon field,

$$g^{(1)}(\mathbf{r}_1, t_1; \mathbf{r}_2, t_2) = \frac{\langle \hat{a}^\dagger(\mathbf{r}_1, t_1) \hat{a}(\mathbf{r}_2, t_2) \rangle}{\sqrt{\langle \hat{a}^\dagger(\mathbf{r}_1, t_1) \hat{a}(\mathbf{r}_1, t_1) \rangle \langle \hat{a}^\dagger(\mathbf{r}_2, t_2) \hat{a}(\mathbf{r}_2, t_2) \rangle}}.$$

The nature of the emitted light-field (bunched classical light or non-classical anti-bunched photons) can be characterized through the second order correlation function

$$g^{(2)}(\mathbf{r}_1, t_1; \mathbf{r}_2, t_2) = \frac{\langle \hat{a}^\dagger(\mathbf{r}_1, t_1) \hat{a}^\dagger(\mathbf{r}_2, t_2) \hat{a}(\mathbf{r}_2, t_2) \hat{a}(\mathbf{r}_1, t_1) \rangle}{\langle \hat{a}^\dagger(\mathbf{r}_1, t_1) \hat{a}(\mathbf{r}_1, t_1) \rangle \langle \hat{a}^\dagger(\mathbf{r}_2, t_2) \hat{a}(\mathbf{r}_2, t_2) \rangle}.$$

Both correlation functions can be measured by means of the proper interferometry experiments on the emitted photons.

1.6 Doped quantum well

All of the above results discussing the exciton and exciton-polariton were derived for an undoped quantum well, i.e. with an empty conduction band. An interesting system is offered by adding additional charges inside (we will restrict ourselves to electrons) in the quantum well. This can be done for example by modulation doping techniques in which electrons from a remote donor layer tunnel into the quantum well because of the specific arrangement of different bandstructures [39]. In particular, we will be interested in the case of a quantum degenerate two-dimensional electron gas (2DEG) inside the quantum well, meaning the de Broglie wave length of the electrons is comparable to or larger than the inter-electron distance. In this way, the fermionic statistics of the electrons becomes an essential ingredient in the description of the 2DEG.

1.6.1 Non-interacting 2DEG

Because the non-interacting 2DEG is a central concept in this thesis, we will introduce it here to set the notations.

In first quantization, the Hamiltonian \hat{h}_0 of the free electron gas is given by

$$\hat{h}_0 = \sum_{j=1}^N \hat{p}_j^2, \quad (1.9)$$

which is a sum of the kinetic energies of all the N electrons. Units are such that $\hbar = 1$, $m_e = 1/2$. Whenever a Hamiltonian is sum of N independent terms, the corresponding *many-body* eigenstate Ψ (written with capital Greek letter) is given as a product of the corresponding single particle eigenstates ϕ (small Greek letters) of the Hamiltonian \hat{h}_0 :

$$\Psi_{\mathbf{k}_1, \mathbf{k}_2, \dots, \mathbf{k}_N}(\mathbf{r}_1, \mathbf{r}_2, \dots, \mathbf{r}_N) = \prod_{j=1}^N \phi_{\mathbf{k}_j}(\mathbf{r}_j) \quad (1.10)$$

where one has

$$\hat{h}_0 |k_j\rangle = \varepsilon_{k_j} |k_j\rangle$$

and $\varepsilon_{k_j} = k_j^2$. Here, the quantum numbers \mathbf{k}_j label the single particle states. For a system with translational symmetry, it corresponds to the linear momentum. The real space wave functions are obtained by considering the states $|\mathbf{k}\rangle$ in position representation: $\langle \mathbf{r} | \mathbf{k} \rangle = \phi_{\mathbf{k}}(\mathbf{r})$.

Because we will always consider zero temperature, the electron gas is degenerate: the thermal wave length of the electrons is much larger than their average interparticle distance, hence the statistics comes into play. Taking into account the fermionic character of the electrons, the many-body wave function should be anti-symmetric under the exchange of two arbitrary particles:

$$\Psi(\mathbf{r}_1, \dots, \mathbf{r}_i, \dots, \mathbf{r}_j, \dots, \mathbf{r}_N) = -\Psi(\mathbf{r}_1, \dots, \mathbf{r}_j, \dots, \mathbf{r}_i, \dots, \mathbf{r}_N)$$

where particles i and j are interchanged and we have neglected the spin quantum number for simplicity. This is the so-called Pauli blocking, which states that no two fermions can occupy the same single particle state. In terms of first quantization, this means that an ordinary product as in Eq. (1.10) needs to be generalized as to become an anti-symmetric product. This can be done using the so-called Slater determinant [45]:

$$\Psi_{\mathbf{k}_1, \mathbf{k}_2, \dots, \mathbf{k}_N}(\mathbf{r}_1, \mathbf{r}_2, \dots, \mathbf{r}_N) = \begin{vmatrix} \phi_{\mathbf{k}_1}(\mathbf{r}_1) & \phi_{\mathbf{k}_1}(\mathbf{r}_2) & \dots & \phi_{\mathbf{k}_1}(\mathbf{r}_N) \\ \phi_{\mathbf{k}_2}(\mathbf{r}_1) & \phi_{\mathbf{k}_2}(\mathbf{r}_2) & & \vdots \\ \vdots & & \ddots & \vdots \\ \phi_{\mathbf{k}_N}(\mathbf{r}_1) & \dots & \dots & \phi_{\mathbf{k}_N}(\mathbf{r}_N) \end{vmatrix}. \quad (1.11)$$

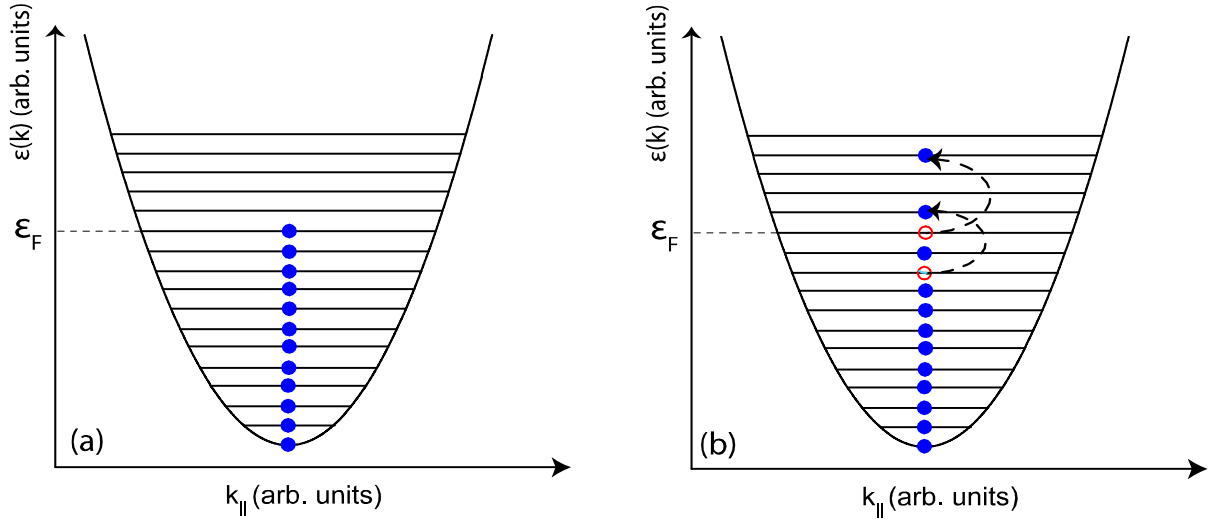


Figure 1.4: a) Ground state of the non-interacting Fermi gas. All single particle states up to the Fermi level are occupied. b) Excited Fermi sea in which two intraband electron-hole pairs (blue full circles and red open circles) are created near the Fermi level. The deep levels far below the Fermi energy are less probably excited due to Pauli blocking and the large cost in energy for creating them.

1.6.2 Fermi sea

Using Pauli's exclusion principle, the many-body ground state can be constructed by putting the N electrons into the N lowest energy single particle states $|\mathbf{k}\rangle$. This state is called the Fermi sea, and the highest occupied energy level ε_F is the Fermi energy. The corresponding wave vector is the Fermi wave vector k_F . In occupation number representation the Fermi sea $|\Psi_0\rangle$ is given as

$$|\Psi_0\rangle = |1, 1, 1, \dots, 1, 0, 0, 0, \dots 0\rangle, \quad (1.12)$$

$\varepsilon_{k_1} \quad \varepsilon_{k_2} \quad \varepsilon_{k_3} \quad \varepsilon_{k_F}$

where the states with energy $\varepsilon_k \leq \varepsilon_{k_F} \equiv \varepsilon_F$ are each occupied by a single electron (neglecting spin degeneracy), see figure 1.4 a).

In second quantization, the Hamiltonian reads

$$\hat{H}_0 = \sum_{\mathbf{k}} \varepsilon_{\mathbf{k}} \hat{c}_{\mathbf{k}}^{\dagger} \hat{c}_{\mathbf{k}}, \quad (1.13)$$

where $\hat{c}_{\mathbf{k}}^{\dagger}$ creates an electron with momentum \mathbf{k} and energy $\varepsilon_{\mathbf{k}}$. The dimensionless operators \hat{c} satisfy the anti-commutation relations

$$\{\hat{c}_{\mathbf{q}}, \hat{c}_{\mathbf{k}}^{\dagger}\} = \delta_{\mathbf{k}\mathbf{q}}$$

such that the operator $\hat{n}_{\mathbf{k}} = \hat{c}_{\mathbf{k}}^{\dagger} \hat{c}_{\mathbf{k}}$ counts the number of quanta in mode $|\mathbf{k}\rangle$. The ground state energy can now be found by calculating the expectation value of \hat{H}_0 in the state $|\Psi_0\rangle$. Since a Slater determinant is an eigenstate of the number operator $\hat{n}_{\mathbf{k}}$ we immediately find

$$E_0 = \langle \Psi_0 | \hat{H}_0 | \Psi_0 \rangle = \sum_{\varepsilon_k < \varepsilon_F} \varepsilon_k. \quad (1.14)$$

Finally, note that for an unpolarized Fermi sea, in which all electrons have the same spin, the electron density can be related with the Fermi energy as (using the units from above)

$$n_e = \frac{k_F^2}{4\pi} = \frac{\varepsilon_F}{4\pi}.$$

1.6.3 Excited Fermi sea

Throughout this work, we will be interested in the effects of some external perturbation on the Fermi sea. In many-body language the perturbation of the state is equivalent to the creation of intraband electron-hole pairs, i.e. within the conduction band: electrons from within the Fermi sea are excited towards unoccupied states above the Fermi level, leaving behind a conduction band hole. The smoothest way to change the many-body state is by creating excitations at low energies. These excitations correspond to intraband pairs created in the vicinity of the Fermi level. The deep levels near the bottom of the conduction band remain unaltered because the cost to excite them on top of the Fermi sea becomes too large. This is shown in figure 1.4b.

To appreciate the importance of the fermionic statistics and the corresponding important role of the Fermi level, imagine the same Fermi sea as being built up with bosonic particles. Then, a perturbation could lead to the creation of intraband pairs within the ‘Fermi sea’ itself, because a single particle state can be occupied multiple times in the bosonic case: there is no need to excite the bosonic particles above the ‘Fermi’ level. Thus for a bosonic state, all filled states contribute in the change of the many-body state.

1.6.4 Fermi edge singularity

There are several reasons why it is interesting to investigate the many-body physics contained in a degenerate 2DEG. The calculation of the absorption spectrum of a *non-interacting* 2DEG is a theoretical problem originally studied by Mahan [46] [47] in the late 60’s and which has been further elaborated by Nozières and many others [48, 49, 50, 51]. It is known that the corresponding absorption spectrum exhibits the so-called ‘Fermi-edge singularity’: the lineshapes are asymmetrical around the Fermi edge (to be defined in later chapters) with a density-dependent power law decay to higher frequencies, see Fig. 1.5 for a qualitative picture. Skolnick *et al.* were the first to clearly observe the Fermi edge singularity in a doped quantum well [52]. This shows that, despite the assumption of the electrons being non-interacting, there is a lot of non-trivial ongoing many-body physics in describing the optical response of the many-body electron wave function. Nowadays, the Fermi edge singularity still attracts a lot of attention, especially in the community working with ultracold atoms [53, 54, 55].

1.6.5 Trion quasiparticle

Another feature of a 2DEG is the possibility to form trion quasiparticles. Under an optical transition, an interband electron-hole pair is created similar to the description of exciton formation. However, due to the electron gas already present in the quantum well, there is now a scenario in which two electrons could bind to the valence band hole, resulting in the so-called trion quasi particle. The latter has been predicted long time ago by Lampert [56]. Trions have been first observed experimentally in 1993 [57] in a two-dimensional CdTe quantum well, followed by many other in different semiconductor materials [58, 59] (GaAs). Indeed, the binding energy tends to increase as the dimensionality of the system is lowered, in this case making the trion more stable in a QW as compared to bulk and hence easier to observe.

From a more theoretical viewpoint, the trion corresponds to the eigenstates of the following

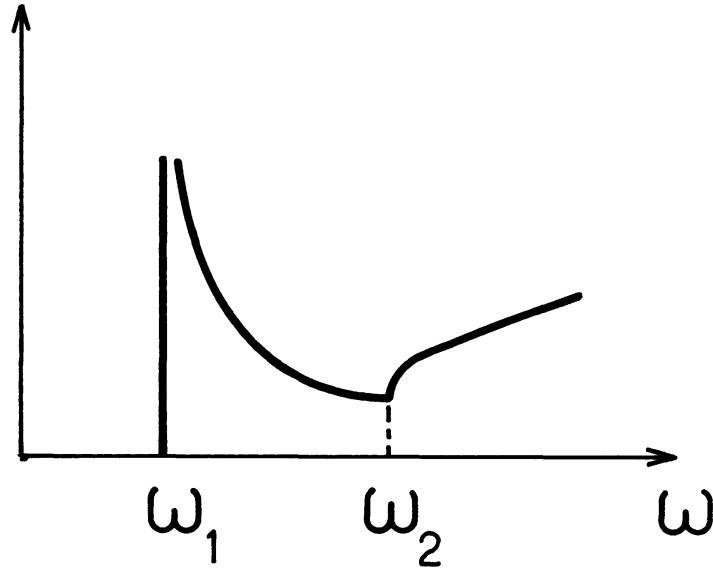


Figure 1.5: Qualitative absorption spectrum of a non-interacting quantum degenerate 2DEG. The lineshape is strongly asymmetric around the Fermi edge ω_1 and decays as a power law to higher frequencies. Original figure taken from Ref. [48].

three-particle Hamiltonian

$$\hat{H}_{\text{trion}} = -\frac{\hbar^2}{2m_e}(\Delta_{\mathbf{r}} + \Delta_{\mathbf{r}'}) - \frac{\hbar^2}{2m_h}\Delta_{\mathbf{x}} - \frac{e^2}{4\pi\epsilon} \left(\frac{1}{|\mathbf{r} - \mathbf{x}|} + \frac{1}{|\mathbf{r}' - \mathbf{x}|} - \frac{1}{|\mathbf{r} - \mathbf{r}'|} \right),$$

where the two electrons (hole) are denoted with position vectors $\mathbf{r}, \mathbf{r}' (\mathbf{x})$. The total energy is given by the kinetic energy of the three particles, the attractive Coulomb interaction between each electron and the hole and the repulsive interaction between the electrons. Because the trion is essentially a three-body problem, a closed solution for the eigenstates does not exist. Many (mostly variational) attempts have been made to describe the trion within a range of parameters (electron density, width of the quantum well, electron-to-hole mass ratio) [60, 61]. A simplified description can be obtained in terms of an electron bound to an exciton, making it a two-body problem for which analytical solutions do exist. Within the limit of low electron density (lower than the inverse exciton Bohr radius) the latter will in general give a good description [62, 63].

1.7 Research question

In complete analogy with the exciton-polariton formation in an empty quantum well, it is now possible to place a doped quantum well inside a microcavity and look at the eigenmodes resulting from the strong coupling between the cavity mode and the two-dimensional electron gas. In particular, it will be interesting to see how the intriguing many-body physics contained in the 2DEG is reflected onto the polariton properties. A pioneering experiment with high density modulation doping was performed by Gabbay *et al.* [17], where it is shown that strong light-matter coupling is possible, even though neither an excitonic nor a trionic state could be resolved. Recently, in the experiments by Smolka *et al.* [20] polariton formation was observed over a range of electron densities, both with and without a magnetic field. For what concerns the effect of the electron gas on the polaritons, various contributions both from the experimental [64, 65, 66] and theoretical [67] side have been made. Those works considered the

electron-polariton scattering physics, but it was assumed that the polariton quasiparticle itself was not affected by the electron gas. From the theoretical side, the mixed electronic-polaritonic system was proposed to reach superconductivity at higher temperatures, possibly even room temperature, thanks to a strongly attractive electron-electron interaction mediated by the polaritons [68]. It is still an open question whether the electron gas truly increases the polariton nonlinearity sufficiently, for example to realize interesting non-linear phenomena such as the polariton blockade.

To be concise, this work tries to answer the following question:

"How does the presence of electrons in the quantum well affect the linear properties of the polaritons?"

We will try to characterize the single particle properties of the polaritons in case the quantum well contains a quantum degenerate two-dimensional electron gas. In particular, we will answer the following questions:

- How does the polariton mass changes as a function of electron density?
- How does the Rabi splitting changes as a function of electron density?
- What do the lineshapes look like?
- What does the spatial part of the trion-polariton look like? Is it a localized particle?

In Chapter 2 we will give a description of the 2DEG optical susceptibility, for the electron density exceeding one electron per exciton Bohr radius squared, see figure 1.6. Using the 2DEG optical susceptibility we look for the polaritons via the dressed photon propagator. Chapter 3 contains a further simplification on the exact result of Chapter 2. The simplified model is used to take into account the finite mass of the valence band hole.

At last, Chapter 4 introduces the effective description for a trion already mentioned in the previous section. Within this effective model we again calculate the optical susceptibility and we study the trion-polariton. A useful quantity to investigate is the spatial structure of the trion-polariton, as this can give a first hint towards the way in which trion-polaritons interact in presence of a 2DEG. Finally, Chapter 5 gives a concise conclusion and outlook towards future research.

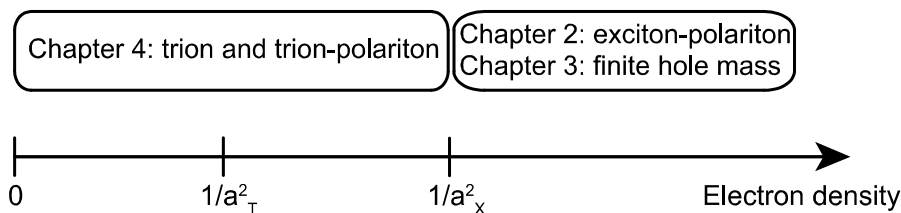


Figure 1.6: Schematic overview of the several chapters in this thesis. In Chapters 2, 3 we investigate the quantum well optical susceptibility for high electron densities: this means the electron can resolve the electron-hole structure of the exciton and we should use the electron-hole basis. In Chapter 4, an effective model for the trion-polariton is set up. There, the exciton is treated as a rigid object, as long as the electron density is lower than the inverse exciton Bohr radius.

Chapter 2

Exciton-polaritons in presence of a non-interacting 2DEG

In this chapter, we focus on a microcavity embedding a highly doped semiconductor quantum well. We stick to the situation in which the electron density n_e greatly exceeds the limit of one electron per squared exciton Bohr radius: $n_e a_X^2 \gg 1$. If an exciton is present in the system, the conduction electrons will be able to resolve the electron-hole structure of the exciton, hence it is suitable to describe the electron gas dynamics in terms of the electron-hole basis.

The content of this chapter is as follows: The general approach towards the calculation for the 2DEG optical response is introduced through Kubo's response theory. Using a simplified model in which the electrons are assumed to be non-interacting, we will pursue an exact calculation of the electron gas optical susceptibility. To obtain the polariton properties such as Rabi splitting, lineshapes, effective mass, ... this result is then inserted as a photon self energy into the photon propagator.

2.1 Kubo's linear response theory and general susceptibility

An interesting question one can ask for any system is the following:

How does a system, initially at rest, react if we give it a small kick?

It is exactly this question that has been answered by Kubo [69].

Suppose we have a system that is described by some Hamiltonian \hat{H}_0 (not necessarily the same as in Eq. (1.13) and we perturb the system with some time-dependent perturbation $\hat{V}(t)$. Then, any expectation value of some operator $\hat{A}(t)$ can be found to lowest order in \hat{V} as

$$\langle \hat{A}(t) \rangle - \langle \hat{A} \rangle_0 = \frac{i}{\hbar} \int_{-\infty}^t \langle \mathcal{T} \{ \hat{V}(s) \hat{A}(t) \} \rangle_0 ds,$$

with \mathcal{T} the time ordering operator putting the operator with the earliest time to the right. The name linear response comes from the fact that only the lowest order contribution in \hat{V} is taken into account. Higher order contributions contain higher order commutators. Note that the evaluation of $\langle \hat{A}(t) \rangle$ now only requires expectation values of operators in the state $| \rangle_0$ before the perturbation, i.e. the groundstate of \hat{H}_0 .

In particular, if one is interested in the observable $\hat{A}(t) = \hat{V}(t)$, one has

$$\langle \hat{V}(t) \rangle - \langle \hat{V} \rangle_0 = \frac{i}{\hbar} \int_{-\infty}^t \langle \mathcal{T} \{ \hat{V}(s) \hat{V}(t) \} \rangle_0 ds.$$

Mostly, if one can write the perturbation part as $\hat{V}(t) = \hat{V} h(t)$ with $h(t)$ a function, the result can further be rewritten as

$$\begin{aligned} \langle \hat{V}(t) \rangle - \langle \hat{V} \rangle_0 &= \int_{-\infty}^t \Pi(s-t) h(s) ds \\ &= (\Pi * h)(t), \end{aligned}$$

where $*$ means a convolution. The function

$$\Pi(s-t) = \frac{i}{\hbar} \langle \mathcal{T} \{ \hat{V}(s) \hat{V}(t) \} \rangle_0$$

is called the impulse response function or the susceptibility. The general time dependent expectation values are then found by a convolution of their impulse response with the time dependent perturbation. Note that the above structure for the time-dependent expectation value is a very general result. For example, when considering Ohm's law for the induced current $j(t)$ due to an external electrical field $E(t)$, one has

$$j(t) = \langle \hat{j}(t) \rangle = \int_{-\infty}^t \sigma(s-t) E(s) ds,$$

where the susceptibility is then the electrical conductivity σ . After Fourier transforming the above equation becomes a product in frequency space yielding the familiar form

$$j(\omega) = \sigma(\omega) E(\omega).$$

2.2 2DEG optical response: quench dynamics

Let us get back to our semiconductor microcavity containing a doped quantum well.

To find the eigenmodes of the coupled system, we first need to calculate the optical susceptibility of the QW, containing all information of this QW onto a perturbation by an external electromagnetic field. The optical field might induce a transition in which an interband electron-hole pair is created, in the very same way as we discussed the exciton formation in the introduction. The Hamiltonian for the quantum well perturbed by the electromagnetic field then reads

$$\hat{H} = \hat{H}_{QW} + \hat{V}(t),$$

with

$$\begin{aligned} \hat{H}_{QW} &= \sum_{\mathbf{k}} \varepsilon_{\mathbf{k}} \hat{c}_{\mathbf{k}}^{\dagger} \hat{c}_{\mathbf{k}} + \varepsilon^h \hat{b}^{\dagger} \hat{b} + \sum_{\mathbf{k}} V_{\mathbf{k}\mathbf{k}'}^{e-h} \hat{c}_{\mathbf{k}'}^{\dagger} \hat{c}_{\mathbf{k}} \hat{b}^{\dagger} \hat{b} \\ \hat{V}(t) &= \sum_{\mathbf{k}} g_{\mathbf{k}} \hat{c}_{\mathbf{k}}^{\dagger} \hat{b}^{\dagger} e^{-i\omega t} + \text{h.c.} \end{aligned} \quad (2.1)$$

where the operator \hat{b}^{\dagger} creates a valence band hole. The first two terms correspond to the kinetic energy of the electrons and holes. The third term in \hat{H}_{QW} describes the electron-hole interaction with some amplitude V^{e-h} . The perturbation to the light-field rotating at a frequency ω is given by $\hat{V}(t)$; with an amplitude $g_{\mathbf{k}}$, either a photon is annihilated and an interband electron-hole pair gets created or vice versa, where the latter is given by the hermitian conjugate term. Here, we have made one very important assumption:

- *The valence band hole is considered infinitely heavy.* This reduces the many-body electron problem to an effective one-body problem in which electrons are scattered onto an external potential, given by the hole. In the following we will thus interchangeably use the terms hole and scattering potential. As we know that an infinite heavy particle has a flat dispersion relation, this means that the hole can absorb any momentum of the electrons without changing its own energy. Also, because $m_h = \infty$ the hole cannot have kinetic energy: the hole does not have any recoil. It is completely localized and as such, we can take the hole to be in the origin of our frame of reference.

It needs no further arguing that this assumption is utterly important. Only under this assumption the optical response can be treated exactly, just because the problem is now essentially a one-body problem.

The optical response function of the electron gas, according to Kubo's linear response theory (see previous section) is now given by

$$\Pi(t) = \sum_{\mathbf{p}\mathbf{p}' > k_F} g_{\mathbf{p}} g_{\mathbf{p}'}^* \langle 0 | \otimes \langle \Psi_0 | \hat{c}_{\mathbf{p}}(t) \hat{b}(t) \hat{c}_{\mathbf{p}'}^\dagger \hat{b}^\dagger | \Psi_0 \rangle \otimes | 0 \rangle, \quad (2.2)$$

where the initial state is given as a product state of the Fermi sea $|\Psi_0\rangle$ with vacuum for the valence band holes $|0\rangle$. The absorption spectrum $\mathcal{A}(\omega)$ is obtained through the Laplace transform of $\Pi(t)$:

$$\mathcal{A}(\omega) = \frac{1}{\pi} \text{Re} \int_0^\infty e^{i\omega t} \Pi(t) dt. \quad (2.3)$$

From Eq. (2.2), we see that at time $t = 0$ a valence band hole and electron are created due to the absorption of a photon. The time evolution of the operators can be written out explicitly in the Heisenberg picture, yielding

$$\begin{aligned} \Pi(t) &= \sum_{\mathbf{p}\mathbf{p}' > k_F} g_{\mathbf{p}} g_{\mathbf{p}'}^* \langle 0 | \otimes \langle \Psi_0 | e^{i\hat{H}_{QW}t} \hat{c}_{\mathbf{p}} \hat{b} e^{-i\hat{H}_{QW}t} \hat{c}_{\mathbf{p}'}^\dagger \hat{b}^\dagger | \Psi_0 \rangle \otimes | 0 \rangle \\ &= e^{iE_0 t} \sum_{\mathbf{p}\mathbf{p}' > k_F} g_{\mathbf{p}} g_{\mathbf{p}'}^* \langle b | \otimes \langle \Psi_0 | \hat{c}_{\mathbf{p}} e^{-i\hat{H}_{QW}t} \hat{c}_{\mathbf{p}'}^\dagger | \Psi_0 \rangle \otimes | b \rangle \\ &= e^{iE_0 t} \sum_{\mathbf{p}\mathbf{p}' > k_F} g_{\mathbf{p}} g_{\mathbf{p}'}^* \langle \Psi_0 | \hat{c}_{\mathbf{p}} e^{-i\hat{H}_f t} \hat{c}_{\mathbf{p}'}^\dagger | \Psi_0 \rangle. \end{aligned}$$

Here, E_0 is the energy of the Fermi sea Eq. (1.14). We also used the fact that the state $\hat{b}^\dagger|0\rangle$ is an eigenstate of \hat{H}_{QW} . Because at time $t = 0$ a valence band hole has appeared in the system, we wrote in the last line $\hat{H}_f = \hat{H}_{QW} (\hat{b}^\dagger \hat{b} = 1)$. The problem is now described in the Hilbert space of the electrons only. Because the number ε^h in \hat{H}_f commutes with everything else we can pull the exponential of ε^h in front and we finally obtain

$$\Pi(t) = e^{iE_0 t} e^{-i\varepsilon^h t} \sum_{\mathbf{p}\mathbf{p}' > k_F} g_{\mathbf{p}} g_{\mathbf{p}'}^* \langle \Psi_0 | \hat{c}_{\mathbf{p}} e^{-i\tilde{H}t} \hat{c}_{\mathbf{p}'}^\dagger | \Psi_0 \rangle, \quad (2.4)$$

$$\tilde{H} = \sum_{\mathbf{k}} \varepsilon_{\mathbf{k}} \hat{c}_{\mathbf{k}}^\dagger \hat{c}_{\mathbf{k}} + \sum_{\mathbf{k}} V_{\mathbf{k}\mathbf{k}'}^{e-h} \hat{c}_{\mathbf{k}'}^\dagger \hat{c}_{\mathbf{k}}. \quad (2.5)$$

The calculation of the optical susceptibility of the 2DEG has now been reduced to the calculation of the expectation value in Eq. (2.4)

Initially at time $t = 0$, one starts with a many-body state $\hat{c}_{\mathbf{p}'}^\dagger |\Psi_0\rangle$, consisting of the Fermi sea $|\Psi_0\rangle$ (built with N electrons in plane wave states $|\mathbf{k}\rangle$, where in the following we will use \mathbf{k} for momenta below k_F) and an additional electron on top of the Fermi sea in a plane wave state

$|\mathbf{p}\rangle$, where we use \mathbf{p} for momenta larger than k_F . Then, the system is quenched: suddenly the time evolution is governed by another Hamiltonian \tilde{H} , for which this initial many-body state is no longer an eigenstate, because of the presence of the scattering potential V^{e-h} . Hence, the overlap with this time evolved state and the other plane wave Slater determinant therefore becomes a function of time.

Again, note that the problem is essentially a one-body problem for the electrons. All many-body eigenstates $|\tilde{\Psi}_N\rangle$ of \tilde{H} , satisfying $\tilde{H}|\tilde{\Psi}_N\rangle = \tilde{E}_N|\tilde{\Psi}_N\rangle$, can thus also be written as a Slater determinant Eq. (1.11), but with different single particle wave functions, satisfying $\hat{h}|\tilde{\phi}_j\rangle = \tilde{\varepsilon}_j|\tilde{\phi}_j\rangle$, where

$$\hat{h}(r_j) = \sum_{j=1}^N \hat{p}_j^2 + \sum_{j=1}^N V^{e-h}(\hat{r}_j) \quad (2.6)$$

is the corresponding single particle Hamiltonian of \tilde{H} in first quantization. The difference between the Hamiltonian \hat{h}_0 in Eq. (1.9) and \hat{h} is exactly the presence of the scattering potential V^{e-h} for the electrons, induced by the valence band hole. In a most naive way, one could insert a complete set of many-body eigenstates for \tilde{H} , this yields (we choose $\varepsilon^h = 0$ as the zero of energy)

$$\Pi(t) = e^{iE_0 t} \sum_{\mathbf{p}\mathbf{p}' > k_F} g_{\mathbf{p}} g_{\mathbf{p}'}^* \sum_N e^{-i\tilde{E}_N t} \langle \Psi_0 | \hat{c}_{\mathbf{p}} | \tilde{\Psi}_N \rangle \langle \tilde{\Psi}_N | \hat{c}_{\mathbf{p}'}^\dagger | \Psi_0 \rangle. \quad (2.7)$$

The last two numbers are overlaps between two Slater determinants, one built with plane waves, the other with eigenstates of the Hamiltonian \hat{h} . In a seminal paper, Anderson has shown that these matrix elements become exponentially small in the system size, which is the so-called *Anderson Orthogonality Catastrophe* [70]. In particular, he has proven for the ground state overlaps that

$$\langle \Psi_0 | \tilde{\Psi}_0 \rangle = N^{-\delta^2/2\pi^2}$$

for $N \rightarrow \infty$ and δ the phase shift at the Fermi level induced by the scattering potential. If one wants to calculate the optical susceptibility, the same analysis should be done for every other intermediate state $|\tilde{\Psi}_N\rangle$. However, there is an exponentially large number of many-body states, hence this becomes an impossible job...

2.2.1 Exact result for the optical response: Combescot and Nozières

Luckily, thanks to Slater we know that all information on the many-body state can be written in terms of single particle states, see section 1.6.1. We thus rewrite the expectation value in Eq. (2.4) in first quantization. For the $N + 1$ electron state we have

$$\hat{c}_{\mathbf{p}'}^\dagger |\Psi_0\rangle = \mathcal{A} [|\mathbf{k}_1\rangle \otimes |\mathbf{k}_2\rangle \dots |\mathbf{k}_F\rangle \otimes |\mathbf{p}'\rangle],$$

where the operator \mathcal{A} properly anti-symmetrizes the direct product of single particle states into a Slater determinant. The Hamiltonian of the $N + 1$ electron system in first quantization becomes

$$\tilde{H} \rightarrow \sum_{j=1}^N \hat{h}_j + \hat{h}_{N+1}.$$

Here, \hat{h}_j acts on the j -th particle in state $|\mathbf{k}_j\rangle$ with energy smaller than ε_F and \hat{h}_{N+1} acts on the additional electron in state $|\mathbf{p}'\rangle$ with $|\mathbf{p}'| > k_F$. Last, the ground state energy of the Fermi

sea can also be written as $E_0 = \sum_{j=1}^N \varepsilon_{\mathbf{k}_j}$. Combining the above expressions now yields

$$\begin{aligned}
& e^{iE_0 t} \langle \Psi_0 | \hat{c}_{\mathbf{p}} e^{-i\hat{H}t} \hat{c}_{\mathbf{p}'}^\dagger | \Psi_0 \rangle \\
&= e^{i \sum_{j=1}^N \varepsilon_{\mathbf{k}_j} t} \mathcal{A} \langle \mathbf{k}_1 | \otimes \langle \mathbf{k}_2 | \dots \langle \mathbf{k}_F | \otimes \langle \mathbf{p} | \left[e^{-i(\sum_{j=1}^N \hat{h}_j + \hat{h}_{N+1})t} \right] \mathcal{A} | \mathbf{k}_1 \rangle \otimes | \mathbf{k}_2 \rangle \dots | \mathbf{k}_F \rangle \otimes | \mathbf{p}' \rangle \\
&= \mathcal{A} \langle \mathbf{k}_1 | \otimes \langle \mathbf{k}_2 | \dots \langle \mathbf{k}_F | \otimes \langle \mathbf{p} | \left[e^{-i \sum_{j=1}^N (\hat{h}_j - \varepsilon_{\mathbf{k}_j})t} e^{-i\hat{h}_{N+1}t} \right] \mathcal{A} | \mathbf{k}_1 \rangle \otimes | \mathbf{k}_2 \rangle \dots | \mathbf{k}_F \rangle \otimes | \mathbf{p}' \rangle \\
&= e^{-i\varepsilon_{\mathbf{p}'}t} \mathcal{A} \langle \mathbf{k}_1 | \otimes \langle \mathbf{k}_2 | \dots \langle \mathbf{k}_F | \otimes \langle \mathbf{p} | \prod_{j=1}^N e^{-i(\hat{h}_j - \varepsilon_{\mathbf{k}_j})t} e^{-i(\hat{h}_{N+1} - \varepsilon_{\mathbf{p}'})t} \mathcal{A} | \mathbf{k}_1 \rangle \otimes | \mathbf{k}_2 \rangle \dots | \mathbf{k}_F \rangle \otimes | \mathbf{p}' \rangle \\
&= e^{-i\varepsilon_{\mathbf{p}'}t} \left[\mathcal{A} \langle \mathbf{k}_1 | \otimes \langle \mathbf{k}_2 | \dots \langle \mathbf{k}_F | \otimes \langle \mathbf{p} | \right] \mathcal{A} \left[e^{-i(\hat{h} - \varepsilon_{\mathbf{k}_j})t} | \mathbf{k}_1 \rangle \otimes \dots \otimes e^{-i(\hat{h} - \varepsilon_{\mathbf{k}_j})t} | \mathbf{k}_F \rangle \otimes e^{-i(\hat{h} - \varepsilon_{\mathbf{p}'})t} | \mathbf{p}' \rangle \right].
\end{aligned}$$

In the last line we dropped the index on the single particle Hamiltonians, because it is now clear upon which state they act. Finally, the overlap between the two Slater determinants in the last line can be written as a determinant again as to become

$$\begin{aligned}
& e^{iE_0 t} \langle \Psi_0 | \hat{c}_{\mathbf{p}} e^{-i\hat{H}t} \hat{c}_{\mathbf{p}'}^\dagger | \Psi_0 \rangle \\
&= e^{-i\varepsilon_{\mathbf{p}'}t} \det \begin{pmatrix} \langle \mathbf{k}_1 | e^{-i(\hat{h} - \varepsilon_{\mathbf{k}_j})t} | \mathbf{k}_1 \rangle & \dots & \langle \mathbf{k}_1 | e^{-i(\hat{h} - \varepsilon_{\mathbf{k}_j})t} | \mathbf{k}_F \rangle & \langle \mathbf{k}_1 | e^{-i(\hat{h} - \varepsilon_{\mathbf{p}'})t} | \mathbf{p}' \rangle \\ \vdots & \ddots & \vdots & \vdots \\ \langle \mathbf{k}_F | e^{-i(\hat{h} - \varepsilon_{\mathbf{k}_j})t} | \mathbf{k}_1 \rangle & & \langle \mathbf{k}_F | e^{-i(\hat{h} - \varepsilon_{\mathbf{k}_j})t} | \mathbf{k}_F \rangle & \langle \mathbf{k}_F | e^{-i(\hat{h} - \varepsilon_{\mathbf{p}'})t} | \mathbf{p}' \rangle \\ \langle \mathbf{p} | e^{-i(\hat{h} - \varepsilon_{\mathbf{k}_j})t} | \mathbf{k}_1 \rangle & & \langle \mathbf{p} | e^{-i(\hat{h} - \varepsilon_{\mathbf{k}_j})t} | \mathbf{k}_F \rangle & \langle \mathbf{p} | e^{-i(\hat{h} - \varepsilon_{\mathbf{p}'})t} | \mathbf{p}' \rangle \end{pmatrix} \\
&= e^{-i\varepsilon_{\mathbf{p}'}t} \det \rho_{\mathbf{p}\mathbf{p}'}(t).
\end{aligned}$$

This is in fact an expression that has been derived in a seminal paper by Combescot and Nozières (CN) [48]. The time-dependent matrix elements of $\rho(t)$ are given by

$$\begin{aligned}
\lambda_{\mathbf{k}\mathbf{q}}(t) &\equiv \langle \mathbf{k} | e^{-i(\hat{h} - \varepsilon_{\mathbf{q}})t} | \mathbf{q} \rangle \\
&= \sum_n \tilde{\phi}_n(\mathbf{k}) \tilde{\phi}_n^*(\mathbf{q}) e^{-i(\tilde{\varepsilon}_n - \varepsilon_{\mathbf{q}})t},
\end{aligned} \tag{2.8}$$

where we used the expansion of $\hat{h} = \sum_n \tilde{\varepsilon}_n |n\rangle \langle n|$ in its eigenbasis. We now see that the optical absorption, which can be written as

$$\Pi(t) = \sum_{\mathbf{p}\mathbf{p}' > k_F} g_{\mathbf{p}} g_{\mathbf{p}'}^* e^{-i\varepsilon_{\mathbf{p}'}t} \det \rho_{\mathbf{p}\mathbf{p}'}(t)$$

is fully determined by the transient behaviour of the unperturbed single particle states in presence of the scattering potential. At time $t = 0$, the matrix ρ becomes the unit matrix and we have a perfect overlap with the initial state.

Note that this is an exact result and it contains all the overlaps with the exponentially many intermediate many-body states as in Eq. (2.7) into a single determinant. Of course, the result can be obtained exactly only because the system is non-interacting. The price to pay is still the calculation of the above determinant, which will be done numerically. Therefore, despite the assumption of a simple non-interacting problem, the physics contained in this determinant can be far from trivial. This will become clear in the next sections. In the limit of long times $t \gg \varepsilon_F^{-1}$ analytical results have been obtained by CN, but we will come back to this later.

Finally, to gain some more intuition of the physics contained in the above determinant, we can expand the determinant along the last row and column, yielding

$$\Pi(t) = G(t) L(t). \tag{2.9}$$

The functions $G(t)$, $L(t)$ read

$$G(t) = \det [\lambda_{\mathbf{k} < \mathbf{k}_F, \mathbf{k}' < \mathbf{k}_F}(t)], \quad (2.10)$$

$$L(t) = \sum_{\mathbf{p}\mathbf{p}' > k_F} g_{\mathbf{p}} g_{\mathbf{p}'}^* e^{-i\varepsilon_{\mathbf{p}'t}} \left[\lambda_{\mathbf{p}\mathbf{p}'}(t) - \sum_{\mathbf{k}\mathbf{k}' < k_F} \lambda_{\mathbf{p}\mathbf{k}}(t) \lambda_{\mathbf{k}\mathbf{k}'}^{-1}(t) \lambda_{\mathbf{k}'\mathbf{p}'}(t) \right]. \quad (2.11)$$

The physical content is the following [71]:

- $G(t)$: this expression describes the dynamics of the valence band hole, i.e. $G(t) = \langle \Psi_0 | \hat{b}(t) \hat{b}^\dagger | \Psi_0 \rangle$.
- $L(t)$: This term has two different contributions. The first term between straight brackets in Eq. (2.11) describes the direct scattering of the conduction electrons from the valence band hole potential from a state $|\mathbf{p}'\rangle \rightarrow |\mathbf{p}\rangle$, both above the Fermi level. The second term between brackets also describes electron scattering $|\mathbf{p}'\rangle \rightarrow |\mathbf{p}\rangle$ but through an exchange process with electrons inside the Fermi sea. The latter exactly corresponds to the creation of intraband electron-hole pairs. It has been shown in Ref. [48] that the exchange contribution only becomes important in the long time limit $t\varepsilon_F \gg 1$.

2.2.2 Short time behaviour $t\varepsilon_F \ll 1$ and Elliot formula for absorption

Consider the short time behaviour $t\varepsilon_F \ll 1$ of the optical response. Then, we can approximate $G(t) \simeq 1$ and we only retain the first term in $L(t)$. We now have for the optical response Eq. (2.9)

$$\Pi(t \ll \varepsilon_F^{-1}) = \sum_{\mathbf{p}\mathbf{p}' > k_F} g_{\mathbf{p}} g_{\mathbf{p}'}^* e^{-i\varepsilon_{\mathbf{p}'t}} \lambda_{\mathbf{p}\mathbf{p}'}(t)$$

which, using the definition of $\lambda_{\mathbf{p}\mathbf{p}'}(t)$ and assuming $g_{\mathbf{p}} = g$ [72], yields

$$\begin{aligned} \Pi(t \ll \varepsilon_F^{-1}) &= \sum_{\mathbf{p}\mathbf{p}' > k_F} g_{\mathbf{p}} g_{\mathbf{p}'}^* e^{-i\varepsilon_{\mathbf{p}'t}} \sum_n \tilde{\phi}_n(\mathbf{p}) \tilde{\phi}_n^*(\mathbf{p}') e^{-i(\tilde{\varepsilon}_n - \varepsilon_{\mathbf{p}'})t} \\ &= |g|^2 \sum_n e^{-i\tilde{\varepsilon}_n t} \left| \sum_{\mathbf{p} > k_F} \tilde{\phi}_n(\mathbf{p}) \right|^2. \end{aligned} \quad (2.12)$$

The optical absorption now becomes, using Eq. (2.3)

$$\begin{aligned} \mathcal{A}(\omega) &= |g|^2 \frac{1}{\pi} \sum_n \left| \sum_{\mathbf{p} > k_F} \tilde{\phi}_n(\mathbf{p}) \right|^2 \lim_{\eta \rightarrow 0^+} \text{Re} \int_0^\infty e^{-\eta^+ t} e^{i\omega t} e^{-i\tilde{\varepsilon}_n t} dt \\ &= |g|^2 \sum_n \left| \sum_{\mathbf{p} > k_F} \tilde{\phi}_n(\mathbf{p}) \right|^2 \delta(\omega - \tilde{\varepsilon}_n), \end{aligned}$$

where we introduced the infinitesimal damping factor η for mathematical rigour.

In particular, for an empty quantum well, i.e. $\mathbf{k}_F = \mathbf{0}$, the above result becomes exact since then $\varepsilon_F^{-1} = \infty$, so the result is valid for all times. The above then further reduces to

$$\mathcal{A}_{k_F=0}(\omega) = |g|^2 \sum_n \left| \tilde{\phi}_n(\mathbf{r} = \mathbf{0}) \right|^2 \delta(\omega - \tilde{\varepsilon}_n), \quad (2.13)$$

where we used

$$\sum_{\mathbf{p}} \tilde{\phi}_n(\mathbf{p}) = \left(\sum_{\mathbf{p}} \tilde{\phi}_n(\mathbf{p}) e^{i\mathbf{p}\mathbf{r}} \right)_{\mathbf{r}=\mathbf{0}} = \tilde{\phi}_n(\mathbf{r} = \mathbf{0}).$$

For a $1/r$ potential, the wave functions $\tilde{\phi}_n(\mathbf{r})$ correspond to the relative exciton wave functions Eq. (1.3). The summation over n runs over all exciton states, both the bound part of the spectrum and the continuum part. The above is the well-known result of Elliot [73], saying that the optical absorption depends on the square of the relative exciton wave function evaluated in $\mathbf{r} = \mathbf{0}$. This is quite intuitive, as the absorption of a photon goes together with the creation of an electron-hole pair. We could say they are created ‘on top of each other’. The reverse process of emission turns an exciton into a photon: the photon can only be created after the exciton is annihilated, i.e. when ‘the electron falls into the hole’. This is exactly the same $\tilde{\phi}_n(\mathbf{r} = \mathbf{0})$ argument. Also note that the assumption of a constant light-matter coupling automatically leads to the conclusion that the photon only couples to zero angular momentum states. Only then the terms $\tilde{\phi}_n(\mathbf{r} = \mathbf{0}) \neq 0$ (see Eq. (1.3)) and there is a finite absorption. Finally, adding a finite lifetime to the energy levels (do not take the limit $\eta^+ \rightarrow 0$) would broaden the lineshape into a Lorentzian with a linewidth η .

2.3 2DEG optical response: model potential and results

We now make things more concrete and turn to a specific model for the electron-hole potential. First, note that under the assumption of a light-matter matrix element $g_{\mathbf{k}} = g$ being a constant in momentum space [72], we only need to investigate the zero angular momentum states for the electrons, see appendix A. This reduces the two-dimensional problem to an effective one-dimensional problem. Following the 1971 paper by CN, we have numerically implemented a separable scattering potential $V_{kk'} = Vu_ku_{k'}$, i.e. the Hamiltonian for the electronic degrees of freedom reads

$$\hat{H} = \sum_k \varepsilon_k \hat{c}_k^\dagger \hat{c}_k + V \sum_{kk'} u_k u_{k'} \hat{c}_{k'}^\dagger \hat{c}_k, \quad (2.14)$$

where all quantum numbers are now one-dimensional variables. The factors u_k can be shown to be $u_k = \sqrt{k/L}$ with L the length of the system. These factors are remnants of the true 2D nature of the system as they properly turn the 1D summations into integrals containing the correct metric elements for an integration in polar coordinates. Using a 1D density of states in k -space $\Delta k = 2\pi/L$, we have

$$\sum_k u_k^2 f(k) \rightarrow \frac{L}{2\pi} \int u_k^2 f(k) dk = \frac{1}{2\pi} \int k f(k) dk.$$

Any potential $V(\mathbf{r})$ with a negative spatial integral $\int V(\mathbf{r}) d^n \mathbf{r} < 0$ has at least one bound state in two dimensions [74, 75]. We therefore choose the amplitude V such that the spectrum of \hat{H} contains a single bound state.

- This *bound state will play the role of the exciton* in what follows, as it is an electron bound to the scattering potential, which was given by the valence band hole. Of course, it is not to be confused with ‘the exciton’ as the form of the potential is different. We choose not to consider a $1/r$ because of its long-range character and the corresponding numerical issues.
- The exciton has a *binding energy* $\varepsilon_B < 0$. This single particle binding energy ε_B will be *fixed for all electron densities*. The absolute number of ε_B does not matter as it merely sets the energy scales.

Using Eqs. (2.8), (2.10) and (2.11) we have numerically implemented the time dependent susceptibility from Eq. (2.9) using the separable potential. The result is shown on a double logarithmic scale in Fig. 2.1 a. for several Fermi energies $\varepsilon_F / |\varepsilon_B|$. For zero density the response

reaches a constant value, while for higher densities $\Pi(t)$ decays as a power law over several orders of magnitude. The powerlaw decay is a manifestation of the Anderson Orthogonality Catastrophe (AOC): as the unperturbed Fermi sea is suddenly quenched with an external potential (the appearance of the valence band hole due to photon absorption), the many-body state tries to adjust itself to the presence of this new potential. As mentioned in section 1.6.3, the Fermi sea will start to create multiple low-lying intraband electron-hole pairs near the Fermi level. As time increases more intraband pairs are created and the overlap with the original unperturbed many-body will decay as a function of time.

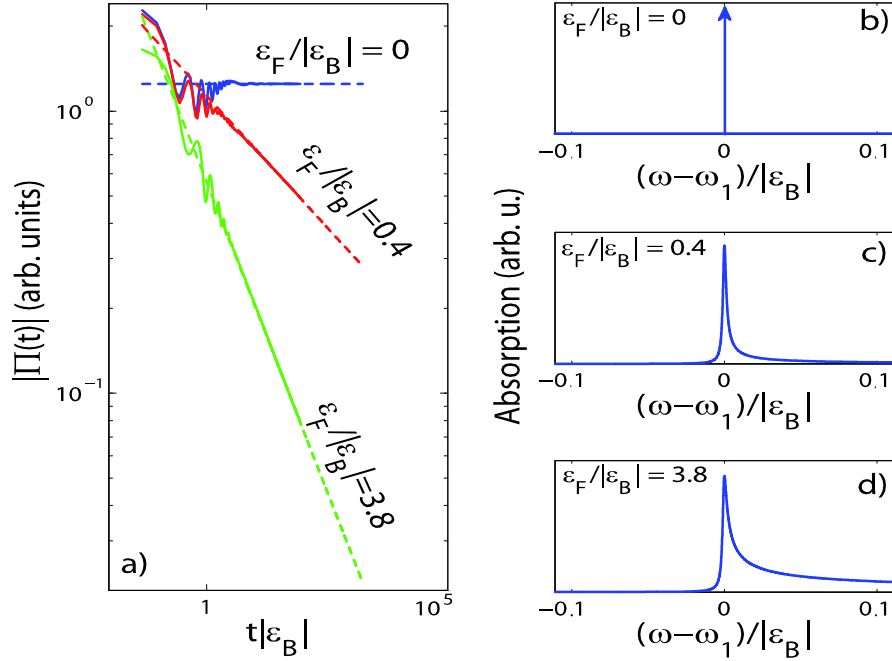


Figure 2.1: (a) Modulus of the numerically calculated response function $\Pi(t)$ (solid lines) and the fitted power law (dashed lines) for several Fermi energies as a function of time. (b)-(d) Optical absorption (arb. units) of the electron gas. For zero density, absorption is due to the bound state, yielding a δ -function. For higher densities, the absorption becomes broadened with a large right asymmetric tail. The nonsingular second threshold is not visible on the plotted energy interval.

In the limit of long times $t \gg \varepsilon_F^{-1}$, CN have analytically shown that the decay goes as a power law, which is due the AOC:

$$\Pi(t \gg \varepsilon_F^{-1}) = C_1 \frac{e^{-i\omega_1 t}}{t^{\alpha_1}} + C_2 \frac{e^{-i\omega_2 t}}{t^{\alpha_2}} \quad (2.15)$$

with $C_{1,2}$ some coefficients. The Laplace transform of a power law to frequency domain reads

$$\int_0^\infty e^{i\omega t} \left(C \frac{e^{-i\Omega t}}{t^\alpha} \right) dt = \frac{|C| \Gamma(1-\alpha) e^{-i\frac{\pi}{2}\alpha}}{(i(\omega - \Omega) + \eta^+)^{1-\alpha}} \quad (2.16)$$

with $\Gamma(x)$ the Gamma function.

The exponents are given in terms of the scattering phase shift at the Fermi energy δ_F as

$$\begin{aligned}\alpha_1 &= \left(\frac{\delta_F}{\pi} - 1 \right)^2, \\ \alpha_2 &= \left(\frac{\delta_F}{\pi} - 2 \right)^2\end{aligned}\tag{2.17}$$

where the phase shift at momentum k is given by [76]

$$\delta_k = (\varepsilon_k - \tilde{\varepsilon}_k) \pi \nu_k$$

with ν_k the density of states. The ‘thresholds’ $\omega_{1,2}$ in the spectrum read

$$\omega_1 = \varepsilon_B + \varepsilon_F + \Delta(\varepsilon_F),\tag{2.18}$$

$$\begin{aligned}\omega_2 &= \omega_1 + |\varepsilon_B| + \varepsilon_F \\ &= \Delta(\varepsilon_F) + 2\varepsilon_F.\end{aligned}\tag{2.19}$$

To explain this, let’s note that the optical response as expressed in Eq. (2.7) can be interpreted as a Fourier series with the Fourier components being given by the energies \tilde{E}_N of the many-body states. The summation in Eq. (2.7) over all many-body states, can be divided into the many-body states in which the single-particle bound state of the spectrum is occupied and in a part in which the bound state is not occupied:

$$\begin{aligned}\Pi(t) &\propto \sum_{\mathbf{p}\mathbf{p}' > k_F} g_{\mathbf{p}} g_{\mathbf{p}'}^* \sum_N e^{-i\tilde{E}_N t} \langle \Psi_0 \hat{c}_{\mathbf{p}} | \tilde{\Psi}_N \rangle \langle \tilde{\Psi}_N | \hat{c}_{\mathbf{p}'}^\dagger | \Psi_0 \rangle \\ &= \sum_{\mathbf{p}\mathbf{p}' > k_F} g_{\mathbf{p}} g_{\mathbf{p}'}^* \left[\begin{aligned} &\sum_{\text{bound state occupied}} e^{-i\tilde{E}_N t} \langle \Psi_0 \hat{c}_{\mathbf{p}} | \tilde{\Psi}_N \rangle \langle \tilde{\Psi}_N | \hat{c}_{\mathbf{p}'}^\dagger | \Psi_0 \rangle \\ &+ \sum_{\text{bound state NOT occupied}} e^{-i\tilde{E}_N t} \langle \Psi_0 \hat{c}_{\mathbf{p}} | \tilde{\Psi}_N \rangle \langle \tilde{\Psi}_N | \hat{c}_{\mathbf{p}'}^\dagger | \Psi_0 \rangle. \end{aligned} \right]\end{aligned}$$

Viewed as a Fourier series, each summation has a lowest energy Fourier component. These are called the thresholds and their corresponding many-body states are depicted in figure 2.2.

Regardless of the occupation of the bound state, the new single particle eigenstates will no longer correspond to plane waves. When building the Fermi sea with these new states (blue dots in Fig. 2.2), a ground state shift

$$\Delta(\varepsilon_F) = \sum_{k < k_F} (\tilde{\varepsilon}_k - \varepsilon_k)$$

with respect to the unperturbed Fermi sea will occur due to the filling of these new states, for which the dispersion does no longer have to be quadratic. Taking into account the original Fermi energy and the occupation of the bound state (left panel) this defines the lowest threshold ω_1 in Eq. (2.18), for which the many-body state is depicted in the left panel in figure 2.2. The second threshold corresponds to the lowest energy many-body state in which the bound state is not occupied: it can be obtained by emptying the bound state and put the electron on top of the Fermi sea. The energy cost is exactly the binding energy plus Fermi energy, defining ω_2 in Eq. (2.19).

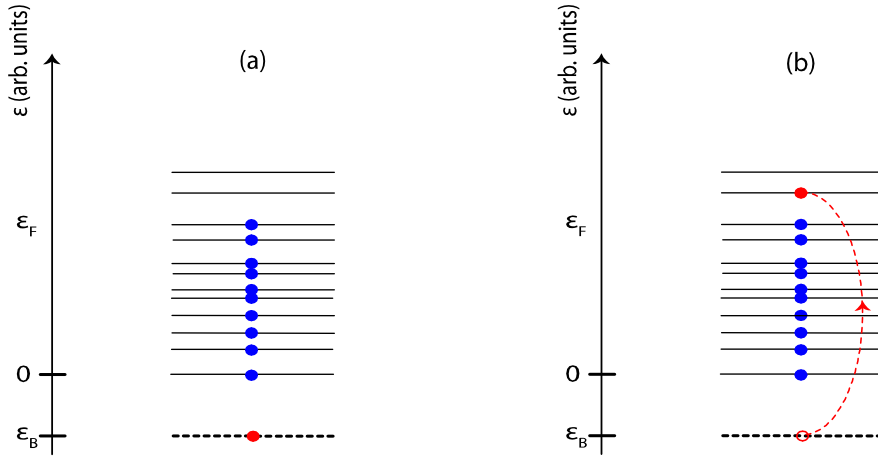


Figure 2.2: The absorption spectrum has two distinct thresholds, determined by the occupation number of the single particle states. (a) Occupying all single particle states, including the bound state, up to the Fermi level defines the lowest threshold ω_1 . (b) The second threshold corresponds to the case when the bound state remains empty. The energy cost relative to ω_1 is given by $|\epsilon_B| + \epsilon_F$.

For our model potential, the exponents and thresholds are shown in figure 2.3. The exponent of the first threshold ω_1 satisfies $\alpha_1 < 1$ for all densities, meaning that the first threshold exhibits the so-called Fermi edge singularity: the optical absorption exhibits singular behaviour at ω_1 , with a power-law tail going like $1/|\omega - \omega_1|^{1-\alpha_1}$. This can be easily seen from the Laplace transform in Eq. (2.16). For the second exponent $\alpha_2 > 1$ holds, corresponding to a non-singular onset of absorption. In the case of an undoped quantum well it holds that $\alpha_1 = 0$, and the first threshold corresponds to the excitation of the well-known exciton for which the absorption is most singular, i.e. a δ -function. The second threshold then corresponds to the onset of continuum absorption, above which free interband electron-hole pairs are excited. To appreciate the form of the lineshapes let's head back to expression (2.16). For zero density we had $\alpha_1 = 0$ and the absorption is given by

$$\text{Re} \left(\frac{|C| \Gamma(1 - \alpha) e^{-i\frac{\pi}{2}\alpha}}{(i(\omega - \Omega) + \eta^+)^{1-\alpha}} \right)_{\alpha=0} \propto \frac{\eta^+}{(\omega - \Omega)^2 + \eta^2}.$$

We find a Lorentzian lineshape for the exciton (in the limit of $\eta = 0$, a δ -function). However, for finite α_1 (at finite electron densities), we can immediately take $\eta = 0$. The lineshapes now also become manifest asymmetric because of the non integer power-law in the denominator. This is seen in Figs. 2.1 (b)-(d). For increasing electron density, the ‘‘excitonic’’ absorption evolves continuously towards a lineshape exhibiting the Fermi edge singularity: a sharp onset and a power-law tail on the right-hand side of the singularity. Note that in theory the onset should be a sudden step, but due to numerical damping with an exponential it is slightly rounded.

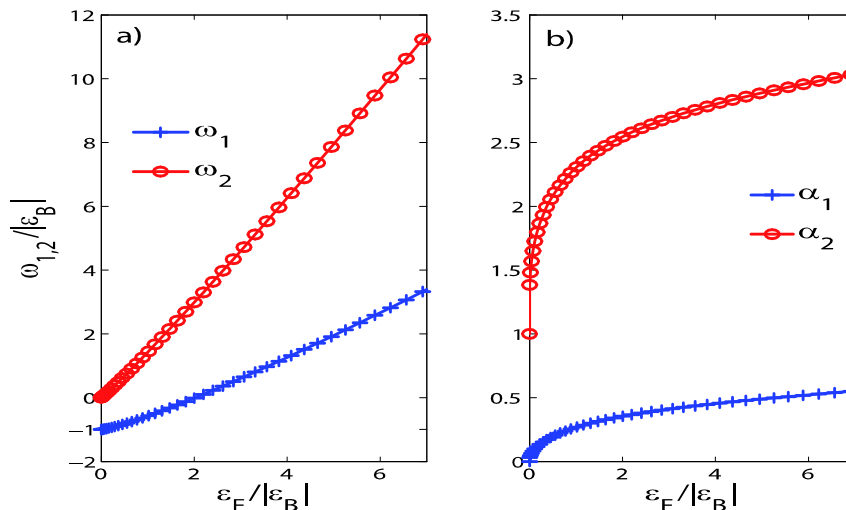


Figure 2.3: (a) Thresholds $\omega_{1,2}$ normalized to the binding energy of the bound state ϵ_B as a function of Fermi energy. (b) Corresponding power-law exponents $\alpha_{1,2}$ as a function of Fermi energy. The exponent α_1 is seen to be smaller than 1, corresponding to a singular behaviour in absorption. Restoring units, $V = -2.5 \hbar^2/m_e$ as used for the strength of the potential.

From the Fig. 2.1a it is seen that the singular threshold dominates the response function for long times. Eq. (2.15) can then be approximated by its first term only,

$$\Pi_{\text{asympt}}(t) = C_1 \frac{e^{-i\omega_1 t}}{t^{\alpha_1}} \quad (2.20)$$

defining what we will call the single-power-law approximation (SPA). Making a fit to the numerical curves with the SPA, we extract the values for C_1 . These are shown in figure 2.4 by the crosses. In a paper by Averkiev and Glazov, the 2DEG optical susceptibility has been computed, starting from a modification of the interband matrix element, mimicking the Fermi-edge singularity asymptotically close to the first threshold [77]. There, the constant in front of Eq. (2.20) is given by $A_1 = 1/2 \sin[\pi(1 - \alpha_1)]$. This is depicted by the open circles in figure 2.4. For low densities, the approximations made in Ref. [77] breaks down, where for higher densities it reproduces the correct orders of magnitude.

We have now fully characterized the absorption spectrum for a non-interacting 2DEG. In particular, we have discussed the form of the lineshapes and the corresponding (non)-singular thresholds and the underlying many-body physics. The next step is to implement the coupling of the doped quantum well with the optical mode inside the cavity.

2.4 Polariton as ‘dressed photon’

2.4.1 Dyson series

Let us put things in another perspective: from the point of view of the photon, the polariton can be looked at as being a photon dressed with matter excitations, due to the interaction with the quantum well. Therefore, consider the series of Feynman diagrams in figure 2.5, depicting the ‘story of a photon in the cavity’. The dressed photon propagator D , denoted by the bold wiggled line, is given as an infinite series of terms in which a photon D_0 turns into a matter

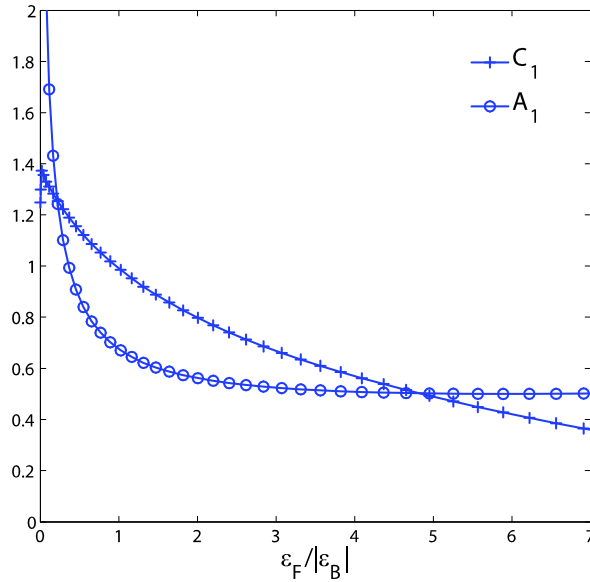


Figure 2.4: Numerically extracted values for C_1 in Eq. (2.20) (crosses) and A_1 as found in Ref. [77] as a function of Fermi energy.

excitation (denoted Π), turns into a photon again, ... and so forth and so on. This specific series of diagrams is called the Dyson series for D_0 . They exactly correspond to the Rabi oscillations of the coupled quantum well - photon system, which is indeed what the photon is experiencing. Note that these diagrams describe the linear properties of the polariton as there are no diagrams that contain photon-photon interactions.

Fig. 2.5b depicts the diagrammatic resummation of all the diagrams from Fig. a, resulting in the dressed photon propagator D . Because the photon propagates both in space and time, the propagator D depends on these values or its reciprocal counterparts, being momentum and frequency. Since at any vertex in the Feynman diagrams energy and momentum should be conserved, the dressed propagator D reads

$$\begin{aligned} D(\mathbf{k}, \omega) &= D_0(\mathbf{k}, \omega) + D_0(\mathbf{k}, \omega) \Pi(\mathbf{k}, \omega) D(\mathbf{k}, \omega) \\ \Rightarrow D(\mathbf{k}, \omega) &= \frac{1}{D_0^{-1}(\mathbf{k}, \omega) - \Pi(\mathbf{k}, \omega)}. \end{aligned}$$

The bare photon propagator [72] in Fourier space simply reads

$$D_0(\mathbf{k}, \omega) = \frac{1}{\omega - \omega_c(\mathbf{k}) + i\gamma_c},$$

where we have introduced a homogenous cavity linewidth γ_c and the photon dispersion $\omega_c(\mathbf{k})$ is given by Eq. (1.1). The poles of D_0 correspond to the possible excitation frequencies of the system: in the case of the bare photon, only the modes with a frequency equal to the cavity resonance are allowed. The linewidth corresponds to some broadening of this resonance because of the imperfection of the mirrors. For simplicity, and without changing the forthcoming analysis, we can again put $\gamma_c = 0$.

Using the above expression for D_0 into the expression for D we finally obtain

$$D(\mathbf{k}, \omega) = \frac{1}{\omega - \omega_c(\mathbf{k}) - \Pi(\mathbf{k}, \omega)}. \quad (2.21)$$

Because of the interaction with the quantum well, reflected by the presence of the term $\Pi(\mathbf{k}, \omega)$, the poles of the dressed propagator are shifted with respect to the bare photon propagator.

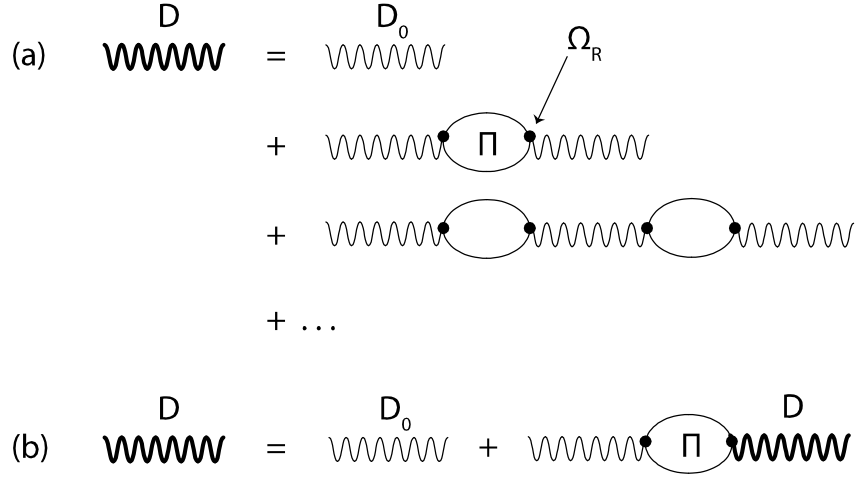


Figure 2.5: The photon propagator as given by a series of Feynman diagrams. a) The photon (wiggled line) propagates and turns into an exciton (circles Π) and reconverts into a photon etc. b) The infinite Dyson series from Fig. (a) can be resummed, defining a dressed photon propagator (bold wiggled line).

In particular, the term $\Pi(\mathbf{k}, \omega)$, which is of course the quantum well optical susceptibility we calculated in the previous section (hence the suggestive notation), serves as a self energy for the photon. If there is no quantum well embedded inside the microcavity, we have $\Pi(\mathbf{k}, \omega) = 0$ and the dressed propagator coincides with the bare propagator, as it should be. The calculation of the quantum well optical susceptibility is the most difficult part when looking for linear polariton properties. Once an expression for Π is found, it can be simply put into Eq. (2.21) and the poles immediately give the polariton energies.

2.4.2 Two-level system revisited

Assume for the optical susceptibility the following:

$$\Pi(\mathbf{k}, \omega) = \frac{\Omega_R^2}{\omega - \omega_X(\mathbf{k})},$$

where the quantum well has a transition at the exciton frequency $\omega_X(\mathbf{k})$ with zero linewidth. It seems we introduced an ad hoc energy scale Ω_R : the latter is necessary for dimensional reasons; remember Π is a self energy and thus should have dimensions of energy. On the other hand, at every vertex in the Feynman diagrams in figure 2.5 (every point in a diagram where a wiggled line turns into a bubble or vice versa) there is a corresponding amplitude. This amplitude, which we suggestively denote as Ω_R , is in fact the very same amplitude that showed up the first time in the Hamiltonian Eq. (1.5).

From Eq. (2.21) we now find

$$\begin{aligned} \frac{1}{\omega - \omega_c(\mathbf{k}) - \Pi(\mathbf{k}, \omega)} &= \frac{1}{\omega - \omega_c(\mathbf{k}) - \frac{\Omega_R^2}{\omega - \omega_X(\mathbf{k})}} \\ &= \frac{1}{(\omega - \omega_-(\mathbf{k}))(\omega - \omega_+(\mathbf{k}))}. \end{aligned}$$

Here, the energies $\omega_{\pm}(\mathbf{k})$ correspond to the upper and lower polariton energies as found in Eq. (1.8). Finally, let us focus on the lower polariton and assume it has a finite lifetime. This

can be due to radiative losses (the photon leaking out of the cavity) as well as the decay of the exciton. The absorption spectrum is per definition given by

$$\mathcal{A}(\omega) = -\frac{1}{\pi} \text{Im} D(\mathbf{k}, \omega)$$

and in the vicinity of the lower polariton resonance this becomes

$$\begin{aligned} \mathcal{A}(\omega) &= -\frac{1}{\pi} \text{Im} \frac{1}{\omega - \omega_-(\mathbf{k}) + i\gamma} \\ &= \frac{1}{\pi} \frac{\gamma}{(\omega - \omega_-(\mathbf{k}))^2 + \gamma^2}. \end{aligned}$$

The factor $1/\pi$ in front is conventional since then we have $\int_{-\infty}^{+\infty} \mathcal{A}(\omega) d\omega = 1$. This shape of $\mathcal{A}(\omega)$ corresponds to a Lorentzian with a resonance at the lower polariton energy and a linewidth γ . In the limit $\gamma \rightarrow 0$ the lineshape reduces to a delta function. Because of the very simplistic underlying model, with only a single exciton transition in the QW, the lineshape is perfectly symmetric around the polariton resonance. As will be shown in the following section, this will no longer be the case if we couple the photon to a charged quantum well.

2.5 Polariton properties in a highly degenerate 2DEG

We will investigate the polariton properties using the quantum well optical susceptibility calculated in the Combescot Nozières formalism in section 2.3. We restrict ourselves to normal incidence of the photon only, meaning we consider the photon propagator for fixed in-plane momentum $\mathbf{k} = \mathbf{0}$:

$$D(i\omega) = \frac{1}{\omega - \omega_c - \Pi(i\omega)}. \quad (2.22)$$

Cavity losses can be easily incorporated by giving ω_c an imaginary part. However, we prefer not to include them in order to highlight the polariton properties stemming from the electron gas dynamics.

2.5.1 Polariton energies and linewidth

Because the singular threshold ω_1 shifts with the electron density, see Fig. 2.3a, we can keep the cavity mode energy ω_c constant and use the 2DEG density as the tuning parameter. A typical anti-crossing spectrum for the choice $g = 0.1\sqrt{|\varepsilon_B|}$ in Eq. (2.11) is depicted in Fig. 2.6a where the cavity mode (red dashed) is fixed. The singular threshold is depicted as the black solid line. Open circles mark the polariton energies, the poles of $D(\omega)$, using the full numerical time series for the optical susceptibility $\Pi(\omega)$, computed in the previous section. Some representative line shapes are shown in Fig. 2.6c. Within our treatment, the lower polariton has zero linewidth. This is due to the fact that the lower polariton energy always lies below the threshold energy ω_1 . At the lower polariton energy, there are no decay channels into matter excitations. In practice, the lower polariton linewidth will thus be determined by the photon life time, at least for the case of the infinite hole mass. When the hole mass is finite, hole relaxation will reduce the life time of the lower polariton, a situation that will be dealt with in the next chapter. The upper polariton on the other hand does show an intrinsic broadening due to the electron gas dynamics. In particular, around resonance, the upper polariton inherits the strong asymmetric form from the electron gas optical absorption. Its full width at half maximum (FWHM) is plotted in Fig. 2.6b. The FWHM reaches its maximum at zero detuning between the photon

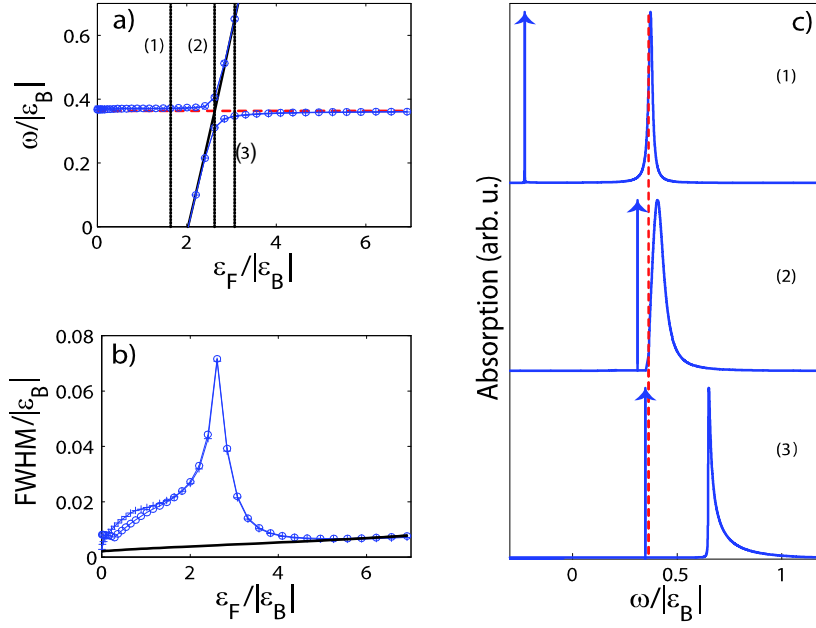


Figure 2.6: (a) Avoided crossing between the singular threshold (black solid line) and the cavity mode (red dashed line). The Fermi energy serves as the detuning parameter, while the photon energy is fixed. Black dotted lines indicate several cuts as fixed densities. (c) The corresponding lineshapes of these cuts depicted as a function of frequency. Again, the red dashed line is the photon energy. (b) Upper polariton full width at half maximum (crosses and circles) as a function of Fermi energy. Light-matter coupling $g = 0.1\sqrt{|\epsilon_B|}$ is used.

and the singular threshold. At high densities the upper polariton linewidth (open circles) is seen to approach the linewidth of the electron gas response function (black solid line). The latter increases itself as a function of density, because the exponent α_1 of the singular threshold increases as a function of density, see Fig. 2.3b.

The crosses in Figs. 2.6(a-b) are obtained by plugging Eq. (2.20) into Eq. (2.22). The agreement with the full numerics is very good, except for a small discrepancy in the upper polariton linewidth at small density. The reason is that at lower densities the power law approximation becomes less justified. The time scale for the asymptotic regime to set in, is determined by the inverse Fermi energy and thus becomes longer for lower densities. The condition for the SPA to work is that the time scales probed by the polariton are longer than the Fermi time. The accuracy of the SPA is therefore expected to become worse for larger light-matter couplings, so that the shorter time optical response of the quantum well is probed. This expectation is borne out in Fig. 2.7, where we plot the same quantities as in Fig. 2.6, but for a larger light-matter coupling strength $g = 1.5\sqrt{|\epsilon_B|}$ vs. $g = 0.1\sqrt{|\epsilon_B|}$. The discrepancy between the SPA (crosses) and the full numerical result (open circles) is indeed larger.

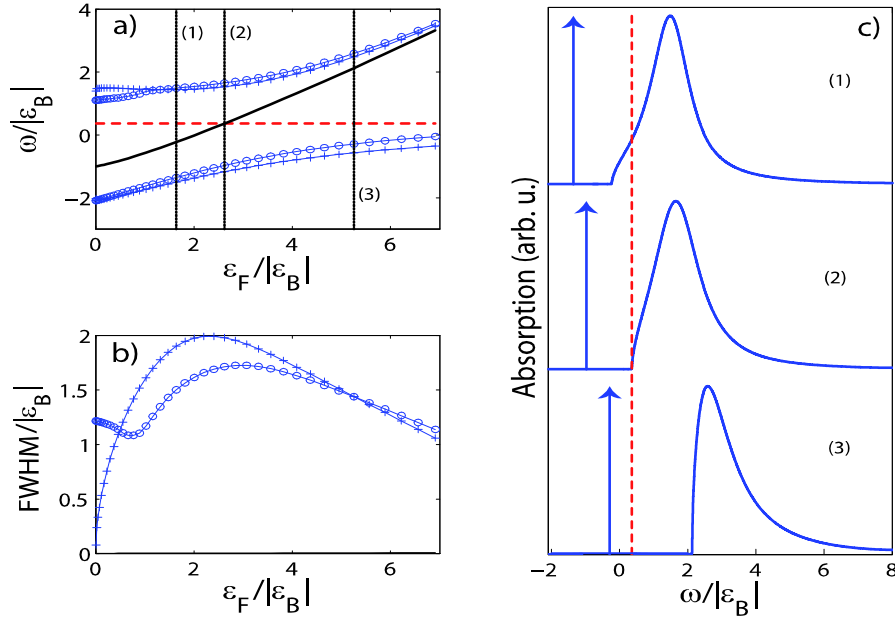


Figure 2.7: (a)-(c) The same quantities as in Fig. 2.6, but for a larger light-matter coupling strength, $g = 1.5\sqrt{|\epsilon_B|}$. The discrepancy between the full numerical result (circles) and the long-time response (crosses) appears in (a) and (b) because the Rabi oscillations are now faster than the Fermi time.

2.5.2 Rabi splitting vs density

Instead of fixing the cavity mode, we can tune the photon into resonance with the singular threshold for every density. We then obtain the Rabi splitting as a function of Fermi energy shown in Fig. 2.8 for two different values of the light-matter coupling $g = 1.5\sqrt{|\epsilon_B|}$ and $g = 0.1\sqrt{|\epsilon_B|}$. Note that, similar to Figs. (2.6-2.7), the difference between the full numerical result (circles) and the SPA (crosses) becomes larger for stronger light-matter coupling and that the discrepancy is largest at low densities. In general the Rabi splitting decreases as a function of the Fermi energy for high densities. We attribute this to the Anderson Orthogonality Catastrophe; the recombination of all the intraband electron-hole pairs excited due to the scattering potential into a single photon becomes less probable so that the overall light-matter overlap decreases. As more intraband pairs get created for increasing electron density, the overall Rabi splitting decreases as a function of density.

Furthermore, we observe a small increase of the Rabi splitting at small Fermi energy in Fig. 2.8b. We attribute it to the influence of the continuum (the second threshold ω_2) on the upper polariton energy. This is illustrated in Fig. 2.9, where we show the upper polariton energy (circles) as a function of Fermi energy. The second threshold ω_2 is depicted by the red solid line. The upper polariton energy is seen to follow ω_2 in the region where the Rabi splitting is increasing (note the different scales on the horizontal axes in Figs. 2.8b and 2.9). For larger Fermi energy ω_2 is pushed to higher energies, see Eq. (2.19). The influence of the continuum then becomes negligible and our numerical results are close to the SPA (crosses).

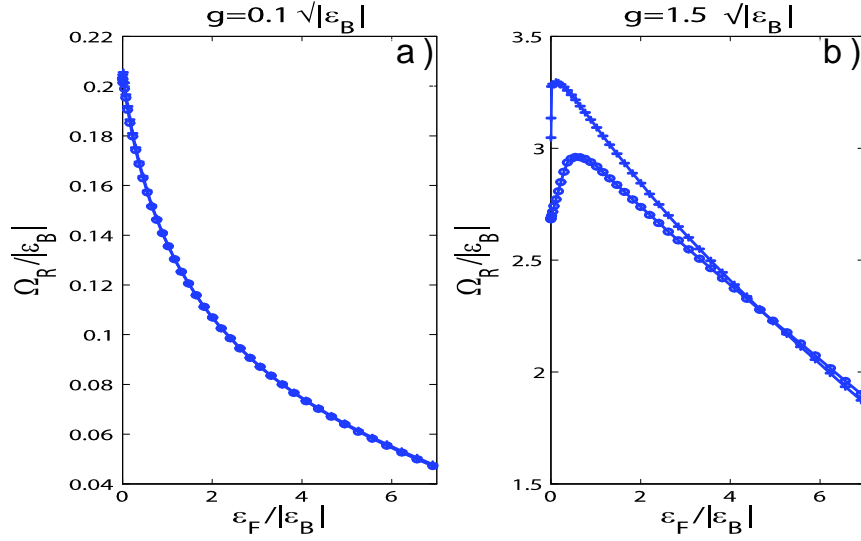


Figure 2.8: Rabi splitting as a function of Fermi energy for two different choices of the light-matter coupling g . For larger g a discrepancy between the exact numerical result (open circles) and the SPA (crosses) appears at low densities. Note the different scales on the vertical axes.

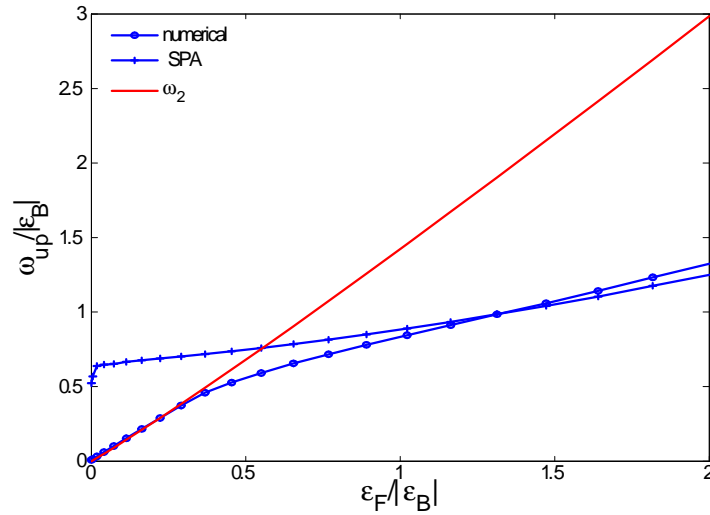


Figure 2.9: Upper polariton energy ω_{up} (circles = fully numerical; crosses = SPA) as a function of Fermi energy. Red solid line depicts ω_2 , the second threshold. $g = 1.5\sqrt{|\epsilon_B|}$ is used for the light-matter coupling strength.

2.5.3 Spectral weights

A further useful characterization of the polariton state is offered by the Hopfield coefficients, that express how much the character of the polariton is photon or matter like. The polariton wave function can be written as

$$|\Psi_{\text{LP,UP}}\rangle = C_{\text{LP,UP}}|\Psi_{\text{photon}}\rangle - \sqrt{1 - |C_{\text{LP,UP}}|^2}|\Psi_{\text{matter}}\rangle,$$

defining the photonic Hopfield coefficient $C_{\text{LP,UP}}$ of the lower and upper polaritons respectively. In terms of the photon spectral function $\mathcal{A}(\omega)$, the photonic Hopfield coefficient of the lower polariton is given by the integral of the spectral function around the lower polariton energy. We identify the upper polariton Hopfield coefficient with the integral over the other frequencies. According to the sum rule for the spectral function,

$$1 = \int_{-\infty}^{+\infty} \mathcal{A}(\omega) d\omega,$$

we then simply have $|C_{\text{UP}}|^2 = 1 - |C_{\text{LP}}|^2$.

Fig. 2.10(a-b) shows the photonic Hopfield coefficients for the lower (blue crosses) and upper (red circles) polariton as a function of Fermi energy. The fixed cavity mode energy was chosen the same as in Figs. 2.6 and 2.7. The Fermi energy serves again as the detuning parameter and the resonance is represented by the black dashed line. For large Fermi energy, the photon is strongly red-detuned with respect to the singular threshold and the lower polariton becomes almost purely photonic. As in the case of the simple exciton-polariton, the character of the lower polariton crosses over from matter like at positive photon detuning to photon like at negative photon detuning for small light-matter coupling. The detuning window in which the crossover takes place, is determined by the Rabi frequency. Remarkably, for larger light-matter coupling the Hopfield coefficients at resonance are different from the value 1/2, that is obtained for a simple two-level system. The reason is that, beside the bound state (singular threshold) contributing to the optical response, also the continuum (non-singular threshold and beyond) forms an important part of the description if the Rabi splitting becomes of the order of the distance between the two thresholds, as showed by Khurgin [78].

The photonic content of the lower polariton is plotted as a function of Fermi energy in Fig. 2.10c, where the photon was taken into resonance with the singular threshold for all Fermi energies. Only at zero density and small light-matter coupling, the polariton consists of equal amounts of photon and matter. For larger light-matter coupling, $g = 1.5\sqrt{|\varepsilon_B|}$ vs $g = 0.1\sqrt{|\varepsilon_B|}$, the ‘Khurgin effect’ results in $|C_{\text{LP}}|^2 > 1/2$ at zero density [78].

2.5.4 Lower polariton effective mass

Within our approximations (in particular the infinite hole mass) the lower polariton is still a quasi particle with infinite intrinsic life time, even in the case of a highly doped quantum well. Its lineshape remains a delta function, despite the electron gas dynamics. The latter only affects the upper polariton lineshape as discussed in previous section. It is therefore interesting to consider the lower polariton effective mass m_{LP} . Let us assume a quadratic in-plane dispersion relation for both the cavity photon and lower polariton. Furthermore, we assume that the electron dynamics happens on a length scale much shorter than the polariton wave length (this amounts to assuming a flat dispersion relation for the electron degrees of freedom as compared to the photon dispersion relation, remember the values $m_X/m_c \sim 10^5$ in table 1.1). Choosing

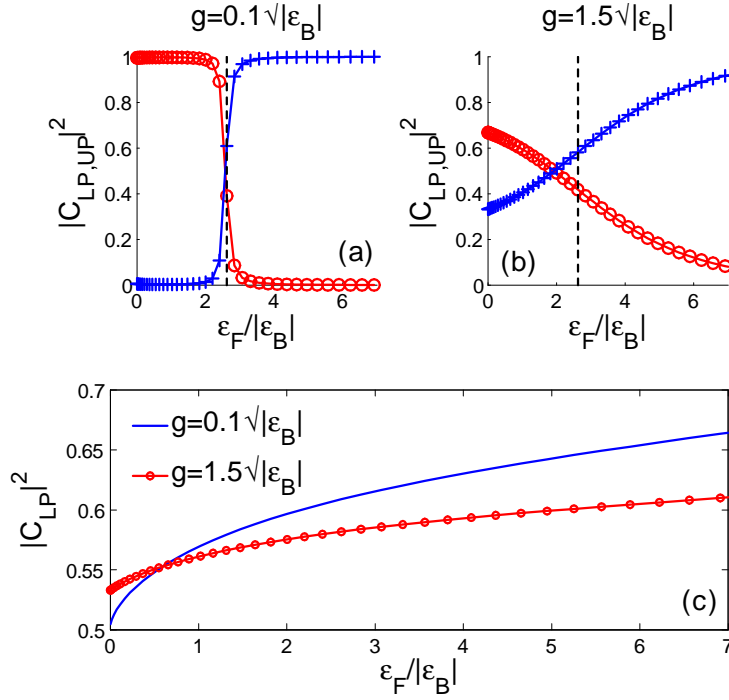


Figure 2.10: (a-b) Photonic Hopfield coefficients for two different strengths of light-matter coupling as a function of Fermi energy. Crosses (circles) represent the photonic Hopfield coefficient for the lower (upper) polariton. The cavity mode was taken the same as in Figs. 2.6 and 2.7. c) Lower polariton photonic Hopfield coefficient when the photon is taken into resonance with the singular threshold for all densities.

the zero of energy at the excitonic threshold ω_1 we have

$$\begin{aligned}\varepsilon_{\text{LP}} &= \alpha + \frac{k^2}{2m_{\text{LP}}}, \\ \varepsilon_c &= \Delta_0 + \frac{k^2}{2m_c}\end{aligned}\quad (2.23)$$

with α some constant. The lower polariton effective mass in terms of the photon mass m_c is

$$\left(\frac{d\varepsilon_{\text{LP}}}{d\Delta_0}\right)^{-1} = \left(\frac{d\varepsilon_{\text{LP}}}{dk^2} \frac{dk^2}{d\varepsilon_c} \frac{d\varepsilon_c}{d\Delta_0}\right)^{-1} = \frac{m_{\text{LP}}}{m_c}, \quad (2.24)$$

where ε_{LP} is the lower polariton energy and $\Delta_0 = \omega_c(\mathbf{k}=\mathbf{0}) - \omega_1(\mathbf{k}=\mathbf{0})$ is the detuning at normal incidence between the cavity mode and the singular threshold. In Fig. 2.11 the lower polariton effective mass as a function of Δ_0 is depicted for several 2DEG densities. For a fixed large $\Delta_0 \gg 0$, the higher electron densities yield a larger lower polariton mass. On the other hand, it turns out that in the regime $\Delta_0 \lesssim 0$ the behaviour is opposite, as can be seen from the inset in Fig. 2.11, showing a more detailed zoom of the left side of the larger figure. There it is seen that the lower polariton mass converges faster towards the bare photon mass for a higher density 2DEG. Both are consequences of the decreased Rabi splitting for a higher density electron gas.

It is instructive to compare our numerical results with the simple two-level model for exciton-polariton formation in an empty quantum well. Then, the lower polariton energy is given by (see Eq. (1.8))

$$\varepsilon_{\text{LP}} = \frac{\omega_c + \omega_1}{2} - \frac{\sqrt{\Delta_0^2 + \Omega_R^2}}{2}.$$

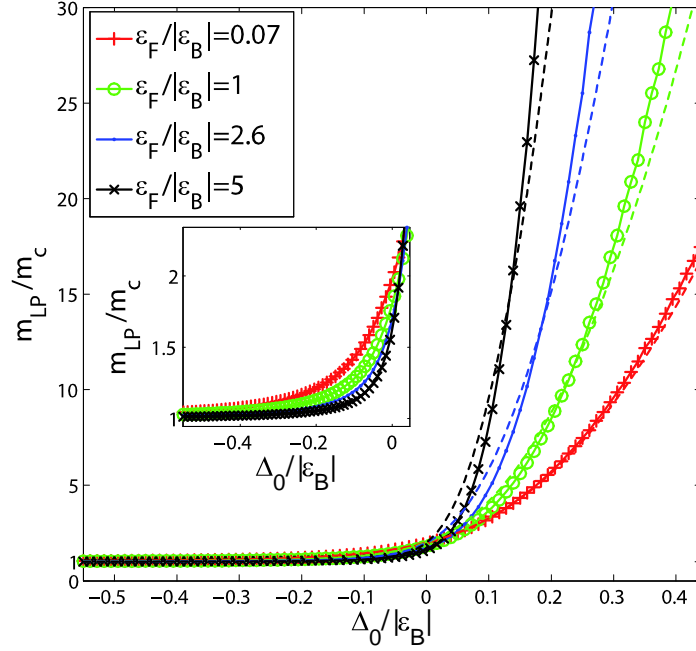


Figure 2.11: Effective mass of the lower polariton (in units of effective photon mass) as a function of Δ_0 . Different lines correspond to different electron densities. The inset is a detailed zoom of the left part of the main figure. $g = 0.1\sqrt{|\epsilon_B|}$ is used for the light-matter coupling strength. The effective mass obtained by using a simple two-level model is depicted by the dashed lines.

Combining the above with Eqs. (2.23-2.24) we find

$$\left(\frac{m_{\text{LP}}}{m_c}\right)_{\text{two level}} = \frac{2}{1 - \frac{\Delta_0}{\sqrt{\Delta_0^2 + \Omega_R^2}}}.$$

In Fig. 2.11 the dashed lines represent the lower polariton effective mass obtained by using the above two-level model. The Rabi frequency used in the above expression is taken from Fig. 2.8a. In the limit of zero electron density the two-level model coincides with the full numerical result. This is expected since for $\Omega_R \ll |\epsilon_B|$ we are only probing the long time response of the electron gas. For nonzero electron densities, a difference between the SPA and the two-level system becomes apparent at positive Δ_0 : due to the presence of the electron gas, the lower polariton appears to be heavier than expected on the basis of the two-level model. Note that in practice the effective polariton mass is obtained by fitting a quadratic curve to the experimentally obtained lower polariton dispersion. For a very large polariton mass, with a very flat dispersion, this fit might become inaccurate.

Chapter 3

Finite hole mass: recoil effects

The previous chapter presented an exact calculation of the optical susceptibility of the 2DEG assuming an infinitely heavy valence band hole. This is not exactly true as can be seen from table 1.1. Roughly, we have the following ratio $m_e^*/m_h^* \in [0.1, 0.4]$, i.e. the hole is only ten to forty times heavier than the electron. Up till now, there are only some qualitative arguments [79, 80] and several attempts that take (approximately) into account the recoil of an impurity immersed in a bath of fermions [71, 81, 82]. We follow another different approach to include the finite valence band hole mass in the exciton formation. In this chapter, we start from the previous results and make a well-controlled approximation in which we come to an effective description for the exciton. It should be stressed that we have to give up on the Anderson Orthogonality and Fermi edge physics in order to estimate the role of the hole recoil. The many-body response of the Fermi sea by intraband pair creation and the corresponding asymmetric lineshapes are thus out of the scope of this chapter.

3.1 Determinants by means of Feynman diagrams

The expression for the optical susceptibility from the previous chapter reads

$$\Pi(t) = G(t) L(t).$$

Here, the functions $G(t)$ and $L(t)$ are defined in Eqs. (2.10-2.11). The function $G(t)$ describes the dynamics of the valence band hole, while $L(t)$ contains the conduction band electron dynamics. These can also be represented by means of Feynman diagrams, as shown in Fig. 3.1a. Assume a photon with energy ω and momentum $\mathbf{k} = \mathbf{0}$ creates the interband electron-hole pair. Due to conservation of the in-plane momentum and energy in the light-matter interaction, the electron-hole pair should have total energy ω and zero momentum as shown in the figure.

Roughly, these diagrams can be divided into three parts. The first row in Fig. 3.1a corresponds to the so-called ‘ladder diagrams’ in which the optically excited electron and valence band hole interact multiple times with each other through the Coulomb interaction $V_{\mathbf{k}\mathbf{k}'}$ (dashed lines). As we will see, the resummation of these kind of diagrams will yield the Wannier equation for the exciton. The second row describes exchange processes in which an electron scatters indirectly from the hole by an exchange process (‘crossed ladders’) with an electron in the Fermi sea, which is also included in the second term of $L(t)$, see Eq. (2.11) These processes are responsible for the Fermi edge singularity and asymmetric lineshapes. Last, the third row gives some diagrams not belonging to any of the two previous ones.

From this viewpoint, the exact formalism using the determinants does an extraordinary task at it sums ALL possible Feynman diagrams. This is remarkable!

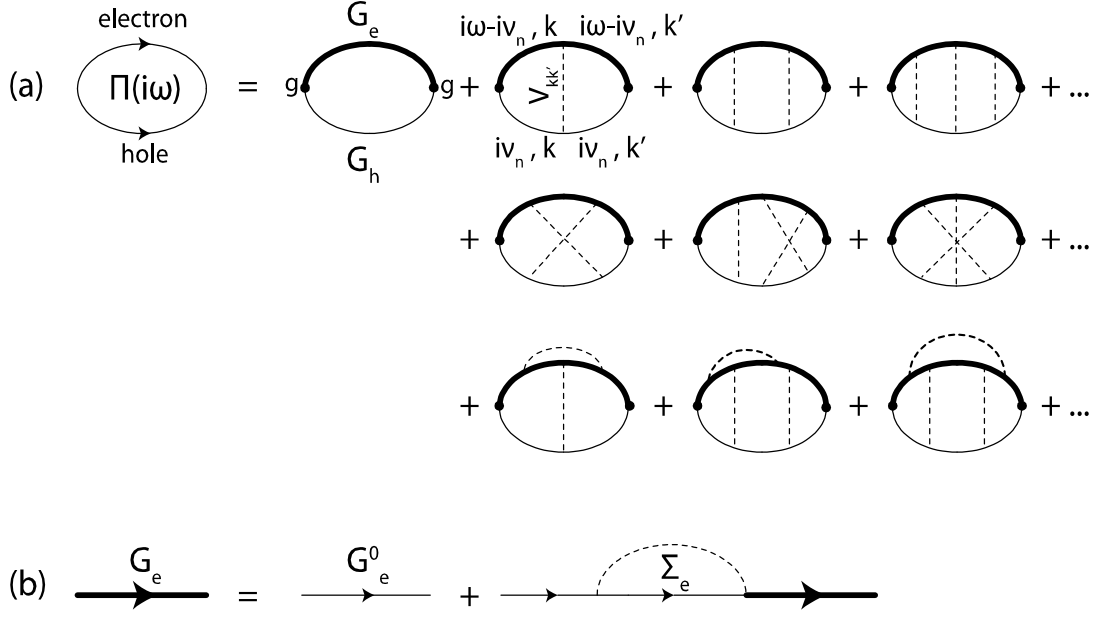


Figure 3.1: (a) 2DEG optical susceptibility $\Pi(i\omega)$ as a series of Feynman diagrams. Top solid line is the dressed electron propagator G_e , while under solid line depicts the valence band hole G_h^0 . Dashed lines depict the screened Coulomb interaction. (b) Dressed propagator for the conduction band electron taking into account exchange interaction Σ_e .

3.2 Wannier equation

3.2.1 Ladder diagrams

We restrict ourselves to a subset of diagrams corresponding to the first row in Fig. 3.1. For the electron and hole Green's function we have

$$G_{e/h}(\mathbf{k}, i\nu_n) = \frac{1}{i\nu_n - \xi_{\mathbf{k}}^{e/h} - \mu_{e/h}}, \quad (3.1)$$

where ($\hbar = 1$)

$$\begin{aligned} \xi_{\mathbf{k}}^e &= \varepsilon_{\mathbf{k}}^e + \Sigma_e(\mathbf{k}), \\ \xi_{\mathbf{k}}^h &= \varepsilon_{\mathbf{k}}^h. \end{aligned}$$

Here we assume a quadratic dispersion for both the electrons and hole, $\varepsilon_{\mathbf{k}}^{e/h} = k^2/2m_{e/h}$. Further, $\Sigma(\mathbf{k})$ is the exchange energy of the electron with the electrons in the Fermi sea:

$$\Sigma(\mathbf{k}) = -\frac{1}{S} \sum_{\mathbf{q}} V_{\mathbf{k}-\mathbf{q}} \Theta(|\mathbf{q}| < k_F).$$

The chemical potentials are given by

$$\begin{aligned} \mu_e &= \xi_{\mathbf{k}_F}^e, \\ \mu_h &= 0 \end{aligned}$$

where the chemical potential for the hole is taken zero because we only consider a single valence band hole.

The sum over Fermionic Matsubara frequencies $i\nu_n$ in the very first diagram (without Coulomb

interaction $V_{\mathbf{k}\mathbf{k}'}$) can be simply calculated [72]. We obtain (the superscript (0) means the diagram has zero ‘ladders’)

$$\begin{aligned}
\pi^{(0)}(i\omega) &= -\frac{|g|^2}{\beta} \frac{1}{S} \sum_{\mathbf{k}} \sum_n G_e(\mathbf{k}, i\omega - i\nu_n) G_h(-\mathbf{k}, i\nu_n) \\
&= \frac{|g|^2}{S} \sum_{\mathbf{k}} \frac{1 - n_F(\varepsilon_{\mathbf{k}}^e) - n_F(\varepsilon_{\mathbf{k}}^h)}{i\omega - \varepsilon_{\mathbf{k}}^e - \Sigma(\mathbf{k}) - \varepsilon_{\mathbf{k}}^h} \\
&= \frac{|g|^2}{S} \sum_{\mathbf{k}} \frac{\Theta(k > k_F)}{i\omega - \frac{k^2}{2\mu} - \Sigma(\mathbf{k})} \\
&= \frac{|g|^2}{S} \sum_{\mathbf{k}} F(\mathbf{k}, i\omega).
\end{aligned}$$

We have defined

$$F(\mathbf{k}, i\omega) = \frac{\Theta(k > k_F)}{i\omega - \frac{k^2}{2\mu} - \Sigma(\mathbf{k})}. \quad (3.2)$$

The reduced mass of the electron-hole pair is given by

$$\frac{1}{\mu} = \frac{1}{m_e} + \frac{1}{m_h}.$$

Because $V_{\mathbf{k}\mathbf{k}'}$ does not depend on frequency, we have for the ladder diagram containing one electron-hole interaction

$$\begin{aligned}
\pi^{(1)}(i\omega) &= \frac{|g|^2}{S^2 \beta^2} \sum_{\mathbf{k}, \mathbf{k}'} \sum_{n, n'} V_{\mathbf{k}-\mathbf{k}'} G_e(\mathbf{k}, i\omega - i\nu_n) G_h(-\mathbf{k}, i\nu_n) G_e(\mathbf{k}', i\omega - i\nu_{n'}) G_h(-\mathbf{k}', i\nu_{n'}) \\
&= \frac{|g|^2}{S^2} \sum_{\mathbf{k}, \mathbf{k}'} V_{\mathbf{k}-\mathbf{k}'} \left[\frac{1}{\beta} \sum_n G_e(\mathbf{k}, i\omega - i\nu_n) G_h(-\mathbf{k}, i\nu_n) \right] \left[\frac{1}{\beta} \sum_{n'} G_e(\mathbf{k}', i\omega - i\nu_{n'}) G_h(-\mathbf{k}', i\nu_{n'}) \right] \\
&= \frac{|g|^2}{S^2} \sum_{\mathbf{k}, \mathbf{k}'} V_{\mathbf{k}-\mathbf{k}'} F(\mathbf{k}, i\omega) F(\mathbf{k}', i\omega).
\end{aligned}$$

This can be easily generalized to the diagrams containing n interactions, only when the Coulomb interaction is assumed to act instantaneously. In a further attempt to include electron interactions, we therefore use the statically screened Coulomb interaction in the RPA approximation

$$V(\mathbf{q}) = \frac{e^2}{2\varepsilon_{\text{RPA}}^{(2D)}(\mathbf{q})} \frac{1}{|\mathbf{q}|},$$

where the Lindhard dielectric function $\varepsilon_{\text{RPA}}^{(2D)}(\mathbf{q})$ has been calculated in Ref. [83]. In all of the following numerical results, this screened Coulomb interaction has been used.

Summing all ladder diagrams one has for the 2DEG optical susceptibility $\Pi(i\omega)$

$$\begin{aligned}
\Pi(i\omega) &= \sum_{n=0}^{\infty} \pi^{(n)}(i\omega) \\
&= |g|^2 \sum_{\mathbf{k}} F(\mathbf{k}, i\omega) + |g|^2 \sum_{\mathbf{k}, \mathbf{k}'} V_{\mathbf{k}-\mathbf{k}'} F(\mathbf{k}, i\omega) F(\mathbf{k}', i\omega) + \dots \\
&= g \sum_{\mathbf{k}} F(\mathbf{k}, i\omega) \Gamma(\mathbf{k}, i\omega) \\
&= g \sum_{\mathbf{k}} P(\mathbf{k}, i\omega).
\end{aligned} \quad (3.3)$$

The function $\Gamma(\mathbf{k}, i\omega)$ satisfies

$$\Gamma(\mathbf{k}, i\omega) = g + \sum_{\mathbf{k}_1} V_{\mathbf{k}-\mathbf{k}_1} F(\mathbf{k}_1, i\omega) \Gamma(\mathbf{k}_1, i\omega),$$

which can easily be checked by inserting this expression into the second last line of Eq. (3.3). Further, we defined

$$P(\mathbf{k}, i\omega) = F(\mathbf{k}, i\omega) \Gamma(\mathbf{k}, i\omega).$$

The optical susceptibility $\Pi(i\omega)$ can be calculated if we know $P(\mathbf{k}, i\omega)$. Using the inverse of the above expression,

$$\Gamma(\mathbf{k}, i\omega) = F^{-1}(\mathbf{k}, i\omega) P(\mathbf{k}, i\omega)$$

and using this into the equation for $\Gamma(\mathbf{k}, i\omega)$, we finally obtain

$$F^{-1}(\mathbf{k}, i\omega) P(\mathbf{k}, i\omega) = g + \frac{1}{S} \sum_{\mathbf{k}_1} V_{\mathbf{k}-\mathbf{k}_1} P(\mathbf{k}_1, i\omega).$$

Rewriting things and using Eq. (3.2) for the expression of $F(\mathbf{k}, i\omega)$ we obtain

$$\frac{1}{S} \sum_{|\mathbf{k}'| > k_F} [i\omega - H_X(\mathbf{k}, \mathbf{k}')] P(\mathbf{k}') = g(\mathbf{k}), \quad (3.4)$$

with

$$H_X(\mathbf{k}, \mathbf{k}') = \left[\left(\frac{k'^2}{2\mu} + \Sigma(\mathbf{k}') \right) \delta_{\mathbf{k}, \mathbf{k}'} + V_{\mathbf{k}-\mathbf{k}'} \right] \Theta(|\mathbf{k}|, |\mathbf{k}'| > k_F) \quad (3.5)$$

the Hamiltonian for the relative motion of the electron and hole, completely analogous to the reduced motion for the hydrogen atom. The major difference however is the presence of the exchange term $\Sigma(\mathbf{k})$ and the Pauli blocking term (the heaviside function, whose origin is Eq. (3.2)) which restricts the momenta of the electron-hole pair to be larger than the Fermi wave vector. Of course, this comes from the fact that an electron can only be optically excited into an unoccupied state, i.e. above the Fermi level.

Equation (3.4) can be inverted to obtain the 2DEG response function:

$$P(\mathbf{k}, i\omega) = g \sum_n \frac{1}{S} \sum_{|\mathbf{k}'| > k_F} \frac{\phi_n(\mathbf{k}) \phi_n(\mathbf{k}')}{i\omega - \varepsilon_n^X},$$

where we used a complete orthonormal set satisfying $H_X|n\rangle = \varepsilon_n^X|n\rangle$ and we assumed $g(\mathbf{k}) = g$. The wave functions $\phi_n(\mathbf{k})$ correspond to the relative exciton wave functions in momentum space, but including Pauli blocking. Plugging the above expression into Eq. (3.3) we finally obtain

$$\Pi(i\omega) = |g|^2 \sum_n \frac{\left| \frac{1}{S} \sum_{|\mathbf{k}| > k_F} \phi_n(\mathbf{k}) \right|^2}{i\omega - \varepsilon_n^X}. \quad (3.6)$$

In conclusion, the ladder diagrams can be resummed to infinite order, yielding the so-called Wannier equation for the exciton relative motion, with the inclusion of Pauli blocking. In the context of nuclear physics, this equation is better known as the Bethe-Salpeter equation. The optical susceptibility is thus straightforwardly found by diagonalizing the Wannier Hamiltonian Eq. (3.5) and using the result in the above expression (3.6). Finally, the spectral density $\mathcal{A}(\omega)$ is given by the imaginary part of the retarded optical susceptibility:

$$\mathcal{A}(\omega) = -\frac{1}{\pi} \lim_{\eta \rightarrow 0^+} \text{Im} \Pi(i\omega \rightarrow \omega + i\eta).$$

In case we turn off the Coulomb interaction, the eigenstates of the Hamiltonian in Eq. (3.5) correspond to plane waves and the spectrum is given by the kinetic energy of the electron-hole pair,

$$\begin{aligned}\phi_n(\mathbf{k}) &\rightarrow \delta_{n,\mathbf{k}} \\ \varepsilon_n^X &\rightarrow \frac{k^2}{2\mu}.\end{aligned}$$

One finds for the free-carrier absorption

$$\begin{aligned}\mathcal{A}_{\text{free carrier}}(\omega) &= \frac{|g|^2}{S} \sum_{|\mathbf{k}| > k_F} \delta\left(\omega - \frac{k^2}{2\mu}\right) \\ &= \frac{|g|^2}{4\pi} \Theta\left(\omega > \frac{k_F^2}{2\mu}\right)\end{aligned}$$

with Θ the Heaviside function. Neglecting the electron-hole pair Coulomb interaction results in a constant absorption above the so-called ‘Fermi edge’, defined by the energy $\frac{k_F^2}{2\mu}$. Below the Fermi edge there is no absorption, while above the Fermi edge the constant absorption is due to the creation of free interband electron-hole pairs. Because the Fermi edge energy increases for higher electron densities, the onset of optical absorption also tend to increase towards larger energies. This is the so-called Burnstein-Moss shift [84, 85], and it is a direct consequence of a degenerate semiconductor and the fact that free electron-hole pairs can only be created on top of the Fermi sea.

3.2.2 Variational ansatz

The Wannier exciton, i.e. the ground state of the Hamiltonian in Eq. (3.5), can also be obtained from a variational principle.

The Hamiltonian for the quantum well reads

$$\begin{aligned}H_{\text{QW}} &= \sum_{\mathbf{k}} (\varepsilon_{\mathbf{k}}^e - \mu_e) \hat{c}_{\mathbf{k}}^\dagger \hat{c}_{\mathbf{k}} + \sum_{\mathbf{k}} (\varepsilon_{\mathbf{k}}^h - \mu_h) \hat{b}_{\mathbf{k}}^\dagger \hat{b}_{\mathbf{k}} \\ &+ \frac{1}{2} \sum_{\mathbf{Q}} \sum_{\mathbf{k}_1, \mathbf{k}_2} V_{\mathbf{Q}} \hat{c}_{\mathbf{k}_1 - \mathbf{Q}}^\dagger \hat{c}_{\mathbf{k}_2 + \mathbf{Q}}^\dagger \hat{c}_{\mathbf{k}_2} \hat{c}_{\mathbf{k}_1} - \sum_{\mathbf{Q}} V_{\mathbf{Q}} \sum_{\mathbf{k}_1, \mathbf{k}_2} \hat{c}_{\mathbf{k}_1 - \mathbf{Q}}^\dagger \hat{b}_{\mathbf{k}_2 + \mathbf{Q}}^\dagger \hat{b}_{\mathbf{k}_2} \hat{c}_{\mathbf{k}_1},\end{aligned}$$

where the first two terms correspond to the kinetic energy for conduction band electrons and valence band holes, created with resp. \hat{c}^\dagger and \hat{b}^\dagger . The third term gives the electron-electron interaction while the last term is the electron-hole Coulomb interaction. Denoting $|\Psi_0\rangle$ as the Fermi sea of electrons, we can start from the following ansatz for the exciton with zero center-of-mass momentum:

$$|X\rangle = \sum_{\mathbf{k}} \phi(\mathbf{k}) \hat{c}_{\mathbf{k}}^\dagger \hat{b}_{-\mathbf{k}}^\dagger |\Psi_0\rangle,$$

with $\phi(\mathbf{k})$ the relative exciton wave function that we are looking for. The expectation value of the energy in the state $|X\rangle$ reads

$$\begin{aligned}
\langle X|H_{\text{QW}}|X\rangle &= \sum_{\mathbf{k}} \frac{k^2}{2\mu} |\phi(\mathbf{k})|^2 \Theta(|\mathbf{k}| > k_F) \\
&+ \sum_{\mathbf{k}_1} \Theta(|\mathbf{k}_1| < k_F) \sum_{\mathbf{k}_2} V_{\mathbf{k}_1, \mathbf{k}_2} |\phi(\mathbf{k}_2)|^2 \Theta(|\mathbf{k}_2| > k_F) \\
&+ \sum_{\mathbf{k}_1, \mathbf{k}_2} V_{\mathbf{k}_1, \mathbf{k}_2} \phi(\mathbf{k}_2) \phi(\mathbf{k}_1) \Theta(|\mathbf{k}_2| > k_F) \Theta(|\mathbf{k}_1| > k_F).
\end{aligned}$$

The variational principle states that the best solution is given by minimizing the expectation value of the energy with respect to the variational parameters $\phi(\mathbf{k})$. Under the normalization condition $\langle X|X\rangle = 1$, one finds that $\phi(\mathbf{k})$ satisfies

$$\frac{k^2}{2\mu} \phi(\mathbf{k}) - \sum_{\mathbf{k}_1} V_{\mathbf{k}_1, \mathbf{k}} \Theta(|\mathbf{k}_1| < k_F) \phi(\mathbf{k}) + \sum_{\mathbf{k}_1} V_{\mathbf{k}_1, \mathbf{k}} \phi(\mathbf{k}_1) \Theta(|\mathbf{k}_1| > k_F) = \varepsilon \phi(\mathbf{k}),$$

where only components larger than k_F are allowed for. This is the very same eigenvalue equation as found from the diagrammatic resummation, for which the Wannier Hamiltonian is given in Eq. (3.5).

At this point, it is instructive to stress the difference between the two approaches used for the calculation of the optical absorption in the previous and current chapter. The current result is obtained by means of a variational calculation, i.e. one only uses the ground state properties of the system before the optical excitation (the Fermi sea). In the previous chapter, however, another physical quantity has been calculated: since we are looking for the optical absorption of the 2DEG, we need to know the response of the 2DEG on the appearance of the valence band hole for all frequencies. In the reciprocal domain we thus need to know the full time-dependent dynamics of the 2DEG after the quench. The determinant method from the previous chapter thus explicitly investigates the non-equilibrium behaviour of the Fermi sea after a quench.

3.2.3 Validity of the result

It is worth noting that the result in Eq. (3.6) is exactly the same as Eq. (2.12) from the previous chapter (if we forget about the exchange energy $\Sigma(\mathbf{k})$ for the electrons). The above choice of ladder diagrams thus correspond to the complete neglect of the second term in Eq. (2.11) as discussed in the same section. We thus do not allow for electron scattering through an exchange process with electrons inside the Fermi sea. This is often called the ‘static Fermi sea approximation’, because the Fermi sea merely acts as a static background for the optically excited electron-hole pair. In the same section, we also argued that this result is only valid for short times $t\varepsilon_F \ll 1$. This means that the above result is a good approximation for low electron densities only. Indeed, the indirect scattering (the ‘crossed ladder diagrams’) between the electrons become important for times $t \gtrsim \varepsilon_F^{-1}$ which correspond to much shorter times for higher Fermi energies.

From the viewpoint of the strong light-matter coupling, which will be of interest to us, the above choice of diagrams can still be justified if we consider a Rabi frequency that is large enough. Typically, since the relevant states in the Fermi sea are the states near the Fermi level, the reaction time of the Fermi sea goes as the inverse Fermi energy. If the Rabi frequency exceeds the Fermi energy $\Omega_R \gg \varepsilon_F$, we could say the static Fermi sea approximation will be quite good because there is no time for the Fermi sea to react. On the other hand, for a given fixed Rabi frequency, the short time response is only accurate in the low-density limit.

3.3 Mahan exciton

Before studying the coupled exciton-photon system, we discuss the exciton itself as a function of density. Again, we restrict ourselves to zero angular momentum states and units of energy and length are taken to be the exciton Rydberg $R_X = \frac{1}{2\mu a_X^2}$, resp. exciton Bohr radius a_X . Neglecting the constant energy of the bandgap, the zero of energy ω_{th} is chosen as the energy of a free electron-hole pair with both particles at the Fermi wave vector, such that the total in-plane momentum of the pair is zero:

$$\omega_{\text{th}} = \frac{k_F^2}{2m_e} + \Sigma(k_F) + \frac{k_F^2}{2m_h} = \frac{k_F^2}{2\mu} + \Sigma(k_F).$$

This energy corresponds to the free particle absorption threshold or ‘Fermi edge’ as seen in Fig. 3.2b. It is the analogon of the second threshold ω_2 in Eq. (2.19), but here the many-body ground state shift is not taken into account. Photons with an energy larger than this Fermi edge energy create free interband electron-hole pairs, i.e. the so-called ‘electron-hole continuum’. We also have another energy scale, given by the lowest energy of a free electron-hole pair. Then, the hole sits at $\mathbf{k} = \mathbf{0}$, while the electron has a momentum \mathbf{k}_F . The energy reads

$$\omega_{\text{eh}} = \frac{k_F^2}{2m_e} + \Sigma(\mathbf{k}_F)$$

and is also depicted in Fig. 3.2b.

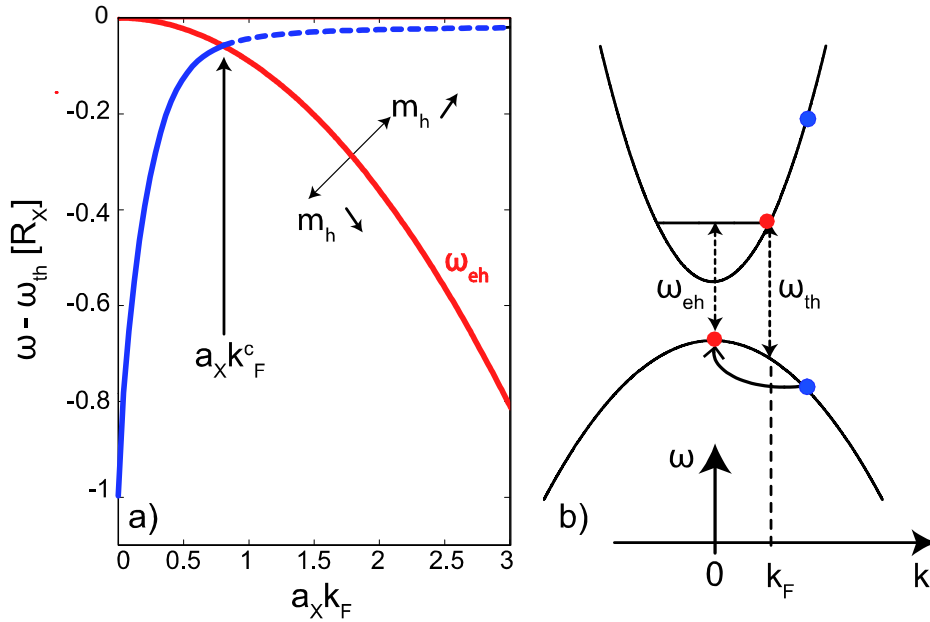


Figure 3.2: Left panel: below $a_X k_F^c$ the exciton forms the groundstate of the optically excited quantum well. Above the critical wave vector (determined by m_e/m_h) the exciton becomes metastable and obtains a finite lifetime due to relaxation of the hole (black arrow) via emission of an intraband electron-hole pair (right panel). We used $m_e/m_h = 0.15$ in the figure.

On the left panel in the same figure, we show the lowest lying exciton level in blue, obtained by diagonalizing the Hamiltonian in Eq. (3.5), as a function of Fermi wave vector (this energy corresponds with the two-particle state depicted by the blue circles in the right panel). Below a critical density, the electron and the hole form a stable bound state below the free electron-hole

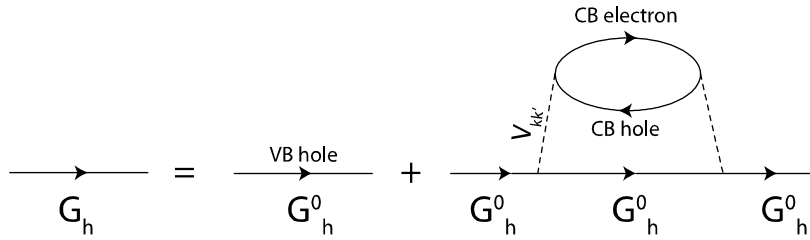


Figure 3.3: Propagator for the valence band hole to lowest order in the Lindhard polarization (the CB electron-hole bubble).

energy ω_{eh} . This is the well-known exciton. Beyond the critical value $a_X k_F^c$, which depends on m_e/m_h and follows a trend as given by the arrows, the exciton crosses ω_{eh} and is no longer the lowest energy state, but becomes a metastable bound state with respect to the Fermi edge (blue dashed line). This metastable state will be referred to as the ‘Mahan exciton’ [46, 86]. It is the hole kinetic energy that is responsible for the fact that the Mahan exciton is not the ground state. When the hole is bound to the electron in a zero momentum exciton, the momentum of the electron has to be compensated by an opposite momentum of the hole. Because the low momentum electron states are Pauli blocked, there is a minimal kinetic energy cost $k_F^2/2m_h$ for the hole to form a bound state with the electron. Obviously, this cost vanishes in the limit where the hole becomes infinitely heavy. We then find that the exciton is stable for arbitrary density and corresponds to the bound state that always exists for an attractive potential in 2D.

3.4 Valence band hole recoil and the lifetime of ‘Mahan polaritons’

Beyond the critical density, the exciton becomes a metastable state because a lower energy state (the free electron-hole pair) is available. As the total exciton momentum is zero, both electron and hole have a momentum \mathbf{k} larger than k_F (the blue dots in Fig. 3.2b). The lowering of the energy of the exciton state towards the free electron-hole pair does require scattering from both the electron and hole. We shall neglect electron scattering for two reasons. First, we believe it is not important because of Pauli blocking and secondly, in this way we can highlight the influence of the hole recoil only, on the polariton formation in a further stage. We will take into account the hole scattering in an approximate way to estimate its consequences on the polariton properties.

To include the recoil of the hole, we consider a modified propagator for the valence band hole, as shown in Fig. 3.3. Note that, opposite to the electron propagator in Fig. 3.1b for which a Dyson series is used, for the valence band hole we only use the bare propagator G_h^0 and the self energy is also expanded to lowest order in the Lindhard polarization. This keeps the calculations manageable.

The Wannier Hamiltonian including the hole dynamical self energy can be found along similar lines as in section 3.2. All we have to do is replace the propagator G_h in the calculation of the ladder diagrams with the propagator in Fig. 3.3. The corresponding Hamiltonian reads (see appendix B)

$$H = \left[\left(\frac{k'^2}{2\mu} + \Sigma(\mathbf{k}') \right) \delta_{\mathbf{k},\mathbf{k}'} + V_{\mathbf{k}-\mathbf{k}'} \right] \Theta(|\mathbf{k}|, |\mathbf{k}'| > k_F) + i \Sigma_h(\mathbf{k}, \omega), \quad (3.7)$$

where

$$\begin{aligned} \Sigma_h(\mathbf{k}, \omega) &\propto \sum_{\mathbf{q}, \mathbf{K}} V_{\mathbf{q}}^2 n_F(\varepsilon_{\mathbf{K}+\mathbf{q}}^e) [1 - n_F(\varepsilon_{\mathbf{K}}^e)] \frac{n_F(-\varepsilon_{-\mathbf{k}+\mathbf{q}}^h + \varepsilon_{\mathbf{K}+\mathbf{q}}^e - \varepsilon_{\mathbf{K}}^e)}{(\varepsilon_{-\mathbf{k}+\mathbf{q}}^h - \varepsilon_{\mathbf{K}+\mathbf{q}}^e + \varepsilon_{\mathbf{K}}^e - \varepsilon_{-\mathbf{k}}^h)^2} \\ &\times \delta[\omega - \varepsilon_{-\mathbf{k}+\mathbf{q}}^h + \varepsilon_{\mathbf{K}+\mathbf{q}}^e - \varepsilon_{\mathbf{K}}^e - \varepsilon_{\mathbf{k}}^e - \Sigma_e(\mathbf{k})] \end{aligned} \quad (3.8)$$

is the contribution of the lifetime of the hole due to recoil effects. It is equivalent to the use of Fermi’s golden rule to calculate the linewidth due to the relaxation of the hole through the emission of a single low energetic intraband electron-hole pair with center-of-mass momentum \mathbf{q} . The δ -function conserves energy and momentum in the scattering process. Note that only the lifetime contribution of this process is taken into account and we neglect the associated energy shift. It can be further expressed in terms of a numerically tractable integral and a Pauli blocking function $\Xi(\mathbf{k}, \omega)$, see appendix B. The latter is given by

$$\Xi(\mathbf{k}, \omega) = \Theta(k > k_F) \Theta\left(\omega > \frac{k^2}{1 + m_e/m_h} + \Sigma_e(\mathbf{k})\right), \quad (3.9)$$

where energies are measured in exciton Rydbergs. The Pauli blocking term $\Xi(\mathbf{k}, \omega)$ tells that if the exciton is stable, i.e. below $a_X k_F^c$, the hole self energy vanishes. Whenever the exciton is metastable, the hole self energy $\Sigma_h(\mathbf{k}, \omega)$ is nonzero at the exciton energy. This can be seen from the photon spectral function (PSF)

$$\begin{aligned} \mathcal{A}(\omega) &= -\frac{1}{\pi} \text{Im} \frac{1}{\omega - \omega_c - \Pi(i\omega)} \\ &= -\frac{1}{\pi} \text{Im} \frac{1}{\omega - \Delta_{c,\text{th}} - \omega_{\text{th}} - \Pi(i\omega)}, \end{aligned} \quad (3.10)$$

where we introduced the cavity mode - Fermi edge detuning $\Delta_{c,\text{th}} = \omega_c - \omega_{\text{th}}$. The optical response itself is again obtained by combining Eqs. (3.6) and (3.7).

In Fig. 3.4a the PSF is depicted as a function of Fermi wave vector and energy for a very large positive cavity detuning $\Delta_{c,\text{th}} \gg 0$. In this way we recover the exciton from Fig. 3.2a. The free electron hole energy ω_{eh} is indicated by the white solid lines in the left lower corner of Figs. 3.4a and b. As mentioned earlier, beyond the critical wave vector the exciton becomes metastable and acquires a finite lifetime due to the relaxation of the hole. As the density increases, the linewidth broadens as it becomes more advantageous for the hole to undergo relaxation towards $\mathbf{k} = \mathbf{0}$, yielding a shorter lifetime. In the limit where the hole relaxation energy becomes comparable to the exciton binding energy, the peaked structure of the exciton resonance gets smeared and the underlying structure can no longer be resolved [86].

Above the Fermi edge ω_{th} , the expression (3.8) for the hole self energy diverges. Actually, above ω_{th} , the photon self energy acquires an imaginary part even when the Hamiltonian is real. Physically, this finite lifetime comes from the conversion of photons into free electrons and holes. Therefore, as a lowest order approximation to the spectral function in the regime above ω_{th} , we do exactly the same as before (diagonalize the Hamiltonian in Eq. (3.7) and plug the obtained wave functions into Eq. (3.6)), but the hole self energy is discarded. In this way we recover an increase in absorption near the Fermi edge, the so-called Sommerfeld or Coulomb enhancement [78, 86]. This is a many-body effect, due to the electron-hole Coulomb interaction between the optically excited electron and hole. Indeed, for large photon frequencies the electron-hole Coulomb interaction is dominated by the kinetic energy of the optically excited carriers and the absorption spectrum asymptotically approaches the free carrier absorption result. The Sommerfeld enhancement is not very clear on the figure 3.4a but is shown in more detail in the insets in Figs. 3.4(c)-(e), where the spectral functions are taken along several cuts

at fixed Fermi wave vectors (indicated by the white dashed lines in Fig. 3.4b). The convergence towards the free carrier result is on an energy scale much larger than shown on the figure. In fact, it has been shown that the absorption due to the Sommerfeld enhancement only decays as $1/\sqrt{\omega}$ [87].

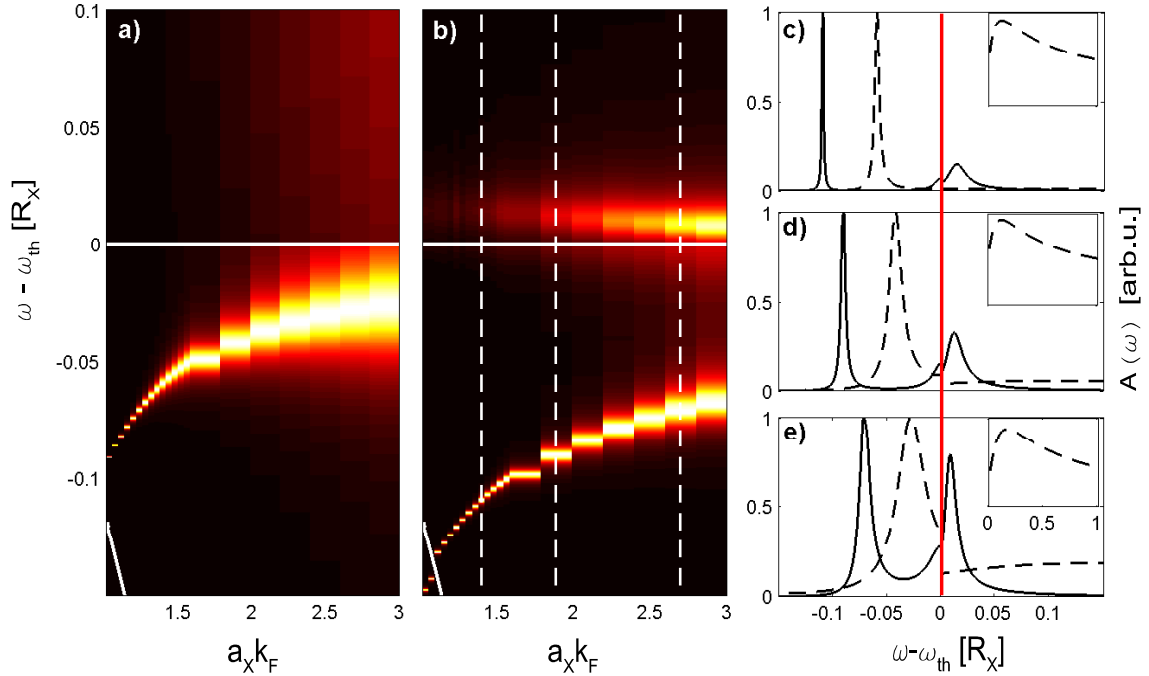


Figure 3.4: a) Photon spectral function (arb. units) as a function of electron Fermi wave vector and energy. The free electron-hole energy ω_{eh} is indicated with the solid white line in the left lower corner. The light-matter coupling strength was chosen $|g|^2 = 0.05 R_X$. b) shows the PSF at $\Delta_{\text{c,th}} = 0$. The lower and upper Mahan polaritons are clearly visible. Different cuts along $a_X k_F$ (white dashed lines) show the narrowing of the PSF (black solid) under the continuum (red line) with respect to the exciton spectral function (black dashed) in panels c-e. The Sommerfeld enhancement is shown in more detail in the insets. Note the different scales between insets and main figures, showing that the upper polariton has a much narrower lineshape as compared to the Sommerfeld enhancement.

To answer the question whether this Coulomb enhancement could lead to the formation of polaritons, we have put the photon into resonance with the Fermi edge ($\Delta_{\text{c,th}} = 0$ in Eq. (3.10)) in Fig. 3.4b for all electron densities. There, we see an upper and lower ‘Fermi edge polariton’, experimentally claimed in Ref. [17]. It is clear, however, that the photon strongly couples with the metastable Mahan exciton, rather than the Fermi edge itself. Henceforth we will call these new eigenstates the Mahan polaritons. The lower Mahan polariton is qualitatively not different from an exciton-polariton in an empty quantum well, as it still is a coherent superposition between the cavity mode and a discrete (metastable) bound state, the Mahan exciton. As expected, the lower Mahan polariton is pushed below the excitonic resonance. Moreover, the shift of the polariton with respect to the exciton is reduced due to the presence of the 2DEG. This is expected since the light-matter coupling is proportional to the electron-hole overlap, which is reduced due to Pauli blocking and screening, as can be seen in Fig. 3.5. Most importantly, the linewidth of the lower Mahan polariton is strongly reduced with respect to the linewidth of the Mahan exciton. This narrowing can be attributed to the reduced final state phase space, which slows the hole relaxation. For low electron densities, it is even possible

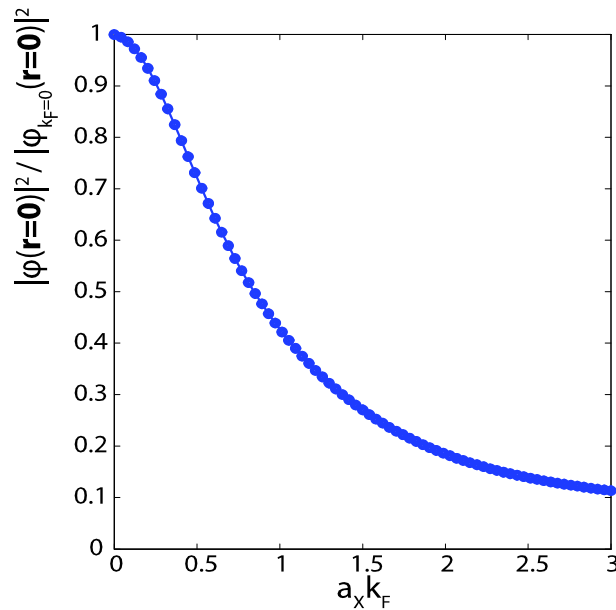


Figure 3.5: Electron-hole overlap (normalized with respect to the electron-hole overlap at zero density) as a function of Fermi wave vector. Due to Pauli blocking and screening, the electron-hole overlap is seen to decrease for increasing Fermi wave vector, reducing the light-matter coupling.

for the polaritons to decrease their energy below the free electron-hole energy ω_{eh} , making their linewidth vanish (on the figure a very small non-zero value is added to make the resonance visible). If one is able to increase the Rabi splitting such that the lower polariton energy lies below the free electron-hole energy, the recoil of the hole can thus be completely discarded as a mechanism responsible for the finite lifetime of the polaritons. Put in another way, there are three different regimes as a function of Rabi frequency (for a fixed electron density): First, if the Rabi frequency is smaller than the linewidth of the hole, we are in the weak coupling regime. Secondly, increasing the Rabi frequency to values larger than the hole linewidth, we reach the strong coupling regime, and the quasiparticles are polaritons with a finite lifetime. Third, if the Rabi frequency even exceeds the hole recoil energy, the polariton lifetime is only determined by the properties of the cavity as the hole recoil is eliminated as a loss channel.

The upper polariton, that can be clearly identified above the absorption threshold in Fig. 3.4b, is qualitatively quite different as compared to the standard exciton-polariton because it lies in the electron-hole continuum. The continuum exciton states now form an essential part of the description of the optical absorption [78]. In fact, the Sommerfeld enhancement above the Fermi edge in the 2DEG absorption is an immediate consequence of the continuum states [87]. Despite the absence of bound electron-hole pairs, the Sommerfeld enhancement still allows for a finite oscillator strength and the formation of the upper polariton. To appreciate this, we have turned off the Coulomb interaction and compared the photon spectral function with and without Coulomb interaction in Fig. 3.6, given respectively by the red and blue lines. There, we observe that the Coulomb interaction is responsible for the narrowing of the polariton linewidth. We also see that the strong coupling between the cavity mode and the electron-hole continuum is a consequence of the Coulomb interaction, as the polariton is pushed into the electron-hole continuum when Coulomb interaction is taken into account. As mentioned before, the upper polariton has an intrinsic lifetime because of the finite absorption above the Fermi edge due to the creation of free interband electron-hole pairs. Finally, it is worth mentioning that when the light-matter coupling is increased, the upper polariton

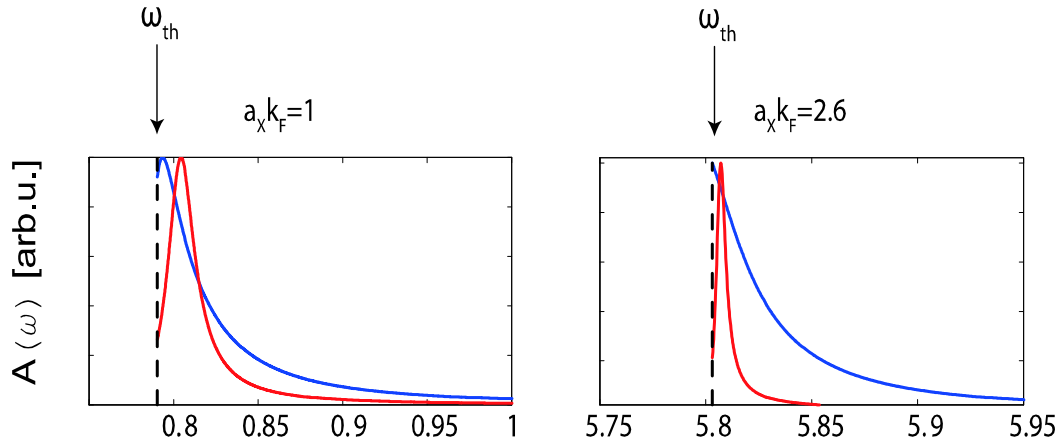


Figure 3.6: Comparison of photon spectral function with (red) and without (blue) electron-hole Coulomb interaction for two different electron densities. The cavity mode is put into resonance with the Fermi edge. A significant narrowing of the linewidth and a larger shift from the cavity mode can be observed when the Coulomb interaction is taken into account.

is further blue shifted and its linewidth increases. For a good visibility of the upper Fermi edge polariton, it is actually advantageous if the Rabi splitting is not too large. This trend is opposite to the one of the lower polariton, where a larger Rabi splitting leads to a lower energy and therefore a longer lifetime. Also note that the upper polariton energy decreases in Fig. 3.4b for increasing electron density, even though the photon energy is constant and the exciton energy increases. In an undoped quantum well, the opposite dependence is observed for increasing exciton energy. We attribute the decrease of the upper polariton energy to the reduction of the electron-hole overlap when the density is increased.

Chapter 4

The trion-polariton

So far, we have been discussing the polariton formation in a highly doped quantum well microcavity. Here, high electron density means that the average distance between the electrons is of the order or less than the exciton Bohr radius. The electrons can then resolve the structure of the exciton, being built from different constituents, i.e. the electron and hole. In this chapter we will discuss the other limit, in which the average electron distance is larger than the exciton Bohr radius. For the electrons, the exciton then looks like an elementary bosonic particle. Within this framework, we will introduce another quasiparticle: the trion. The formation and single particle properties of the trion-polariton, the quasi particle resulting from the coherent superposition of the cavity mode and the trion, are investigated.

4.1 Optical response using an effective trion model

Assume an exciton is created inside the quantum well due to the absorption of a photon. In the presence of a 2DEG, the exciton will interact with the electrons, with the possibility of forming a trionic bound state, where the valence band hole is bound to two electrons. Typically, the trion binding energy is much weaker than the exciton binding energy. For example, in GaAs one has $\varepsilon_X/\varepsilon_T \simeq 10$. Therefore, the trion can be approximated as an electron that is bound to an exciton through an effective electron-exciton potential V^{X-e} , reducing the trion physics from a three-body to a two-body problem. Provided that the electron-electron interactions can be neglected and the exciton mass tends to infinity, the optical response properties of the 2DEG can be found. We will assume a spin polarized 2DEG and the electron spin from the exciton is assumed to be opposite to the 2DEG spin. In this way we discuss the singlet state of the trion only.

4.1.1 Hamiltonian

We start from the following Hamiltonian:

$$\hat{H} = \hat{H}_M + \hat{V}_{LM},$$

with

$$\hat{H}_M = \sum_{\mathbf{k}} \varepsilon_{\mathbf{k}} \hat{c}_{\mathbf{k}}^\dagger \hat{c}_{\mathbf{k}} + \sum_{\mathbf{k}, \mathbf{k}'} V_{\mathbf{k}\mathbf{k}'}^{X-e} \hat{c}_{\mathbf{k}'}^\dagger \hat{c}_{\mathbf{k}} \hat{\psi}_X^\dagger \hat{\psi}_X.$$

Here, \hat{H}_M describes the matter degrees of freedom of the quantum well. Because the exciton (created with $\hat{\psi}_X^\dagger$) is assumed to have infinite mass, it is sufficient to consider a single mode that is localized in real space with energy ε_X . We have implicitly chosen $\varepsilon_X = 0$ as the zero of energy. The kinetic energy for the electrons, created with $\hat{c}_{\mathbf{k}}^\dagger$, is given by $\varepsilon_{\mathbf{k}} = k^2$ (units are

$\hbar = 1, m_e = 1/2$). The last term in \hat{H}_M describes the electron scattering by the exciton. In particular we will use an exciton-electron potential V^{X-e} , satisfying $\int V^{X-e}(\mathbf{r}) d^2r < 0$, for which it is known that in two dimensions this always results in the presence of a bound state with energy $\varepsilon_T < 0$.

The coupling of the QW to the photon field is again treated semiclassically as

$$\hat{V}_{LM} = gA_L e^{-i\omega_L t} \hat{\psi}_X^\dagger + \text{h.c.} \quad (4.1)$$

where g is the coupling constant between the optical mode in the cavity and the exciton center-of-mass at zero in-plane momentum. The amplitude A_L represents a coherent drive by an external laser field at frequency ω . The optical response $G(t)$ of the QW is given by linear response theory as (see Sec. 2.1)

$$G(t) = \langle 0 | \otimes \langle \Psi_0 | \hat{\psi}_X(t) \hat{\psi}_X^\dagger | \Psi_0 \rangle \otimes | 0 \rangle, \quad (4.2)$$

where $|\Psi_0\rangle$ and $|0\rangle$ denote the Fermi sea of electrons, resp. vacuum for the excitons. The above expression can be further elaborated along the lines from Sec. 2.2, yielding

$$\begin{aligned} G(t) &= e^{iE_0 t} \langle X | \otimes \langle \Psi_0 | e^{-i\hat{H}_M t} | \Psi_0 \rangle \otimes | X \rangle \\ &= e^{iE_0 t} \langle \Psi_0 | e^{-i\bar{H}t} | \Psi_0 \rangle. \end{aligned} \quad (4.3)$$

Here, $\bar{H} = \hat{H}_M (\hat{\psi}_X^\dagger \hat{\psi}_X = 1)$ and E_0 again represents the ground state energy of the Fermi sea built with plane waves. The problem is now fully described within the Hilbert space of the electrons. At time $t = 0$, the Fermi sea of electrons is quenched with an external potential, given by the exciton. The optical response is given by the overlap of the time-evolved Fermi sea under the new Hamiltonian and the original Fermi sea.

4.1.2 Optical absorption in the zero angular momentum channel

Baring in mind that our initial state is a Slater determinant built with plane waves, the expectation value (4.3) can be straightforwardly computed along the same lines as in section 2.2.1. Restricting ourselves to zero angular momentum states for the electrons only, and at zero temperature, we have

$$G(t) = \det [\lambda_{kk'}(t)]_{\varepsilon_k, \varepsilon_{k'} < \varepsilon_F}. \quad (4.4)$$

The matrix $\lambda(t)$ reads

$$\lambda_{kk'}(t) = e^{-i\varepsilon_k t} \langle k | e^{-i\hat{H}t} | k' \rangle \quad (4.5a)$$

$$= \sum_p \langle k | p \rangle \langle p | k' \rangle e^{-i(\bar{\varepsilon}_p - \varepsilon_k)t}, \quad (4.5b)$$

where $\bar{H}|p\rangle = \bar{\varepsilon}_p|p\rangle$. Finally the 2DEG spectral function can be obtained by the Laplace transform of $G(t)$.

$$\mathcal{A}(\omega) = \frac{1}{\pi} \text{Re} \int_0^\infty e^{-i\omega t} G(t) dt. \quad (4.6)$$

In the long time limit $t \gg \varepsilon_F^{-1}$ the function $G(t)$ is given as a sum of two power laws [48],

$$\mathcal{G}(t \gg \varepsilon_F^{-1}) = C_1 \frac{e^{i\omega_1 t}}{t^{\alpha_1}} + C_2 \frac{e^{i\omega_2 t}}{t^{\alpha_2}}, \quad (4.7)$$

with $C_{1,2}$ some constants. Again, the power law decay is a consequence of the Anderson Orthogonality Catastrophe. However, the powers $\alpha_{1,2}$ are different from those of the response function as discussed in chapter 2:

$$\alpha_1 = \left(\frac{\delta_F}{\pi} \right)^2 \quad (4.8a)$$

$$\alpha_2 = \left(\frac{\delta_F}{\pi} - 1 \right)^2. \quad (4.8b)$$

It is the phase shifts at the Fermi surface from the electrons scattering of the exciton that determine the exponents. The phase shifts have been proven to satisfy $\delta_F \in [0, \pi]$, making $\alpha_{1,2} \in [0, 1]$. Remember, the Laplace transform of the separate terms in Eq. (4.7) reads

$$\int_0^\infty e^{-i\omega t} \left[C \frac{e^{i\Omega t}}{t^\alpha} \right] dt = \frac{|C| \Gamma(1 - \alpha) e^{-i\frac{\pi\alpha}{2}}}{(\omega - \Omega + i\eta^+)^{1-\alpha}}, \quad (4.9)$$

with $\Gamma(x)$ the gamma function. From this and the value of the exponents, it follows that the absorption spectrum now contains two singularities, the so-called Fermi edge singularities. The positions of the singularities in frequency domain ('thresholds') is given by [48]

$$\omega_1 = \varepsilon_T + \Delta(\varepsilon_F) \quad (4.10a)$$

$$\omega_2 = \Delta(\varepsilon_F) + \varepsilon_F, \quad (4.10b)$$

where $\Delta(\varepsilon_F) = \sum_{p < k_F} (\bar{\varepsilon}_p - \varepsilon_p)$ is the energy difference between the system's many-body ground state before and after the quench. These threshold positions can be found analogously as in section 2.3.

Let us now be more specific about the choice for the exciton-electron potential. For electrons a few Bohr radii away from the exciton, it looks like the exciton is an object without electrical charge. As a function of radial distance, the exciton-electron potential should thus decay rapidly. We therefore chose to work with an attractive Yukawa potential $V^{X-e}(r) = ae^{-r/b}/r$ with $a < 0, b > 0$ numerical constants. The potential needs to be attractive to ensure the presence of a bound state in the spectrum, corresponding to the trion. All of the following results have been verified to give qualitatively the same results for some other short-range potentials as well.

The thresholds (4.10) and the corresponding power law exponents in real time domain (4.8) for the above choice of V are depicted in Fig. 4.1 as a function of Fermi energy.

Because the scattering potential is attractive, the single particle spectrum $\bar{\varepsilon}_n$ contains a bound state with energy $\varepsilon_T < 0$, corresponding to the state in which an electron is bound to the exciton, i.e. a trion. The trion binding energy is thus given by the amount of energy needed to dissociate the trion into an exciton and an electron. In the following, the binding energy is fixed for all electron densities and it will be used as an energy scale. Again, note that upon including electron-electron interactions, the single particle binding energy becomes a (decreasing) function of electron density. This will be dealt with in future research.

At zero density, the lowest threshold ω_1 corresponds to the trion and the upper threshold ω_2 is given by the exciton energy (which we chose as the zero of energy). For sake of simplicity, in the following we will call the lowest threshold the trion, and the highest threshold the exciton for all densities (this should not be confused with the thresholds in chapter 1, in which the lowest threshold ω_1 corresponded to the exciton and the upper threshold ω_2 denoted the electron-hole continuum!). Still at zero density, we find that the power law exponent in time domain corresponding to the trion (α_1) is exactly one, while the exciton exponent α_2 is zero. From Eq. (4.9) we then immediately see that the exciton corresponds to a delta function in

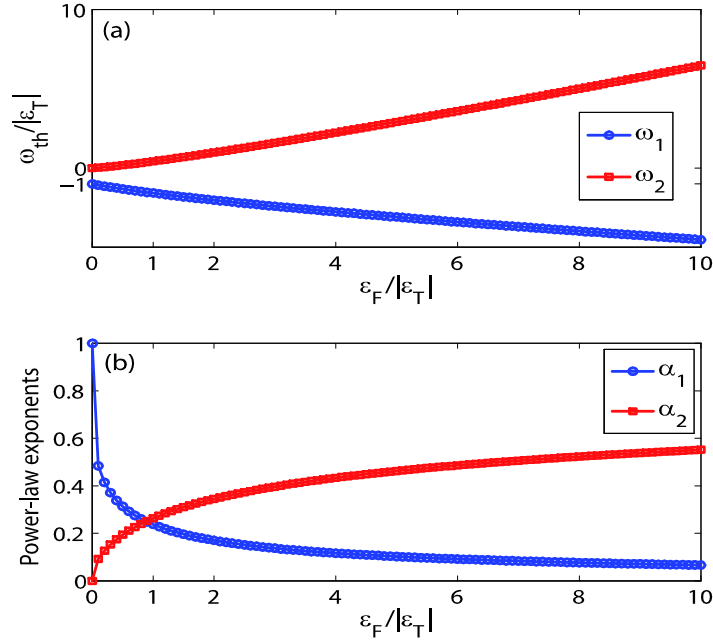


Figure 4.1: (a) Thresholds $\omega_{1,2}$ as a function of Fermi energy. (b) Power-law exponents $\alpha_{1,2}$ as a function of Fermi energy. Both exponents are seen to be smaller than 1, corresponding to two singularities in the absorption spectrum. For Fermi energies larger or comparable to the trion binding energy, the trion exponent (blue open circles) starts getting smaller than the exciton exponents (red squares).

absorption while the trion is completely flat in frequency domain. For increasing electron density, the trion exponent gets larger than the excitonic exponent, the crossover being for the Fermi energy comparable to the trion binding energy. The latter means that the trion tends to get more delta-function like in absorption for increasing 2DEG density, while the exciton gets flattened out. The two thresholds are getting more separated for increasing Fermi energy. This would correspond to an increase of the trion binding energy for higher electron densities. This seems unphysical and should be attributed to the neglect of electron-electron interactions.

Note that, in order for our model (the exciton as elementary boson) to be valid we must avoid very high electron densities. Specifically, we are restricted to densities satisfying $\epsilon_F \ll |\epsilon_X|$. This means that the electron interparticle distance should on average always be larger than the exciton Bohr radius. Only in this situation it is not possible for the electrons to see the internal structure of the exciton. Typically, in GaAs QW's it holds that $\epsilon_T \simeq 0.1\epsilon_X$, so in order for our model to stay valid we must have approximately $\epsilon_F \leq 10|\epsilon_T|$. This explains the horizontal range on the figure 4.1.

For the Yukawa potential mentioned earlier, we have numerically computed the response function $G(t)$ in the time domain up to times for which the asymptotic regime, Eq. (4.7), sets in. In Figs. 4.2(a-c) the modulus of the response function is plotted for increasing 2DEG density from top to bottom. Note the double logarithmic scale to evidence the power law nature of the decay. The oscillatory behaviour originates from the beating between the trionic and excitonic frequency in Eq. (4.7). Solid lines correspond to the numerical simulation while the dashed (dotted) line corresponds to the power law decay using the trion (exciton) exponent from Fig. 4.1(b). To obtain the absorption, we numerically performed the Laplace transform of the time series using an appropriate damping term to avoid manifestations of the Gibbs

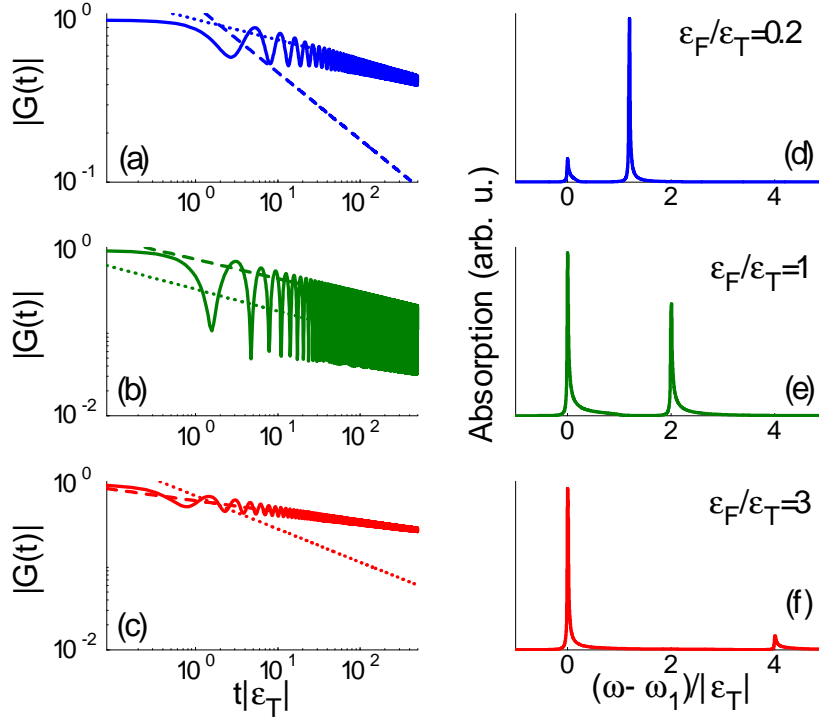


Figure 4.2: (a)-(c) Solid lines: Modulus of the response function $|G(t)|$ on a double-logarithmic scale for increasing Fermi energy. The dashed (dotted) lines depict the power law decay using the exponents α_1 (α_2) from Eqs. 4.8 (d)-(f) Absorption spectra obtained after performing the Laplace transform of the time series. Spectral weight is shifted from the exciton singularity at low densities towards the trion threshold at higher densities.

phenomenon. The corresponding absorption spectra are seen in Figs. 4.2(d-f). All spectra are shifted with respect to the trion threshold ω_1 . The spectral lines are seen to have an asymmetric lineshape with a power law tail at the high frequency side of the threshold. This is due to the power-law exponent in Eq. (4.9). Only for the real time exponent being exactly zero, the lineshape becomes a symmetric Lorentzian. In theory, the absorption on the left hand side of the trion singularity should be identically zero. Due to the numerical damping, this sudden step is slightly rounded. Furthermore, for increasing Fermi energy we see that the distance between the two thresholds indeed increases, as mentioned before. The trion is seen to get narrower again for higher densities (the corresponding real time exponent goes to zero for high densities, see Fig. 4.1b). Experimentally many effects such as electron-electron interactions, finite temperature, will nevertheless broaden the spectral line.

4.1.3 Oscillator strength

To quantify which of both singularities is most dominant in the spectrum, we define the oscillator strength as the integral of the absorption spectrum around each singularity. The boundary between the two thresholds is taken as the frequency where the absorption has its minimal value in between. Fig. 4.3 shows the oscillator strength as a function of Fermi energy. From the definition (4.6) we see that the spectral function obeys a sum rule: $\int_{-\infty}^{\infty} \mathcal{A}(\omega) d\omega = 1$. At zero density all spectral weight is in the exciton (red squares), that is a delta function. This is indeed the only transition that is possible in our model, since at least one electron is needed to form a trion. For increasing Fermi energy, oscillator strength is transferred from the exciton

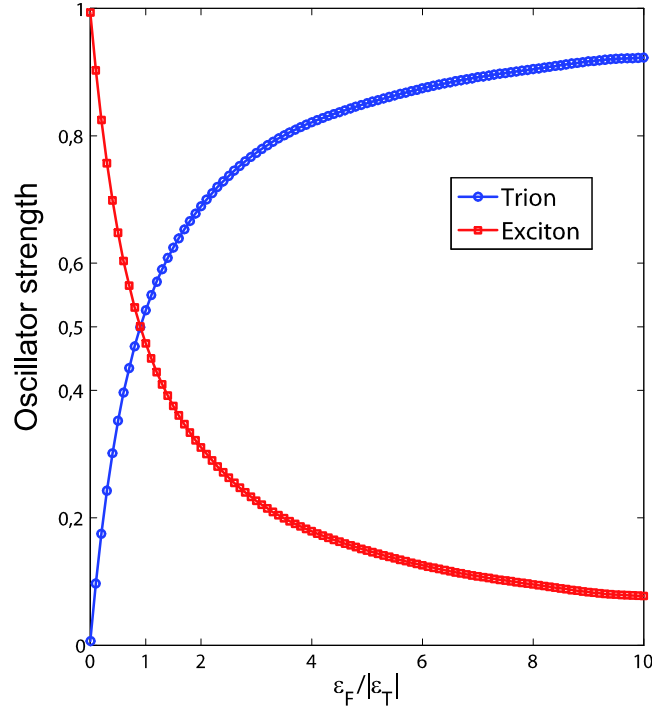


Figure 4.3: Oscillator strength of the trion and exciton as a function of Fermi energy. At zero density the exciton contains all oscillator strength. The trion starts dominating for Fermi energies larger than the trion binding energy.

towards the trion (blue circles). Both singularities have equal oscillator strength when the Fermi energy is comparable to the trion binding energy. For very high 2DEG densities most oscillator is gathered in the trion. This is also seen in the spectral lineshapes in Figs. 4.2(d-f) where the exciton is seen to be dominant at low densities, while the trion starts dominating for high electron densities [65].

4.1.4 Higher angular momentum channels

Throughout this work, the electron gas is treated as a purely two-dimensional system, i.e. the electrons have two degrees of freedom and the single particle states are labelled with two quantum numbers. We have chosen to label the states in the angular momentum basis. In particular, we have only treated the zero angular momentum $l = 0$ states up till now. However, also the $l \neq 0$ states are scattered by the exciton and the full optical response of the 2DEG is given by the response of all the angular momentum channels. If we write the ground state before the quench as a direct product of Fermi seas with different angular momentum,

$$|\Phi_0\rangle = |\Psi_0\rangle_{l=0} \otimes |\Psi_0\rangle_{l=1} \otimes \dots \otimes |\Psi_0\rangle_{l=N} \dots$$

where $l \in \mathbb{N}$ denotes the angular momentum, the optical response is given by

$$\begin{aligned} G(t) &= \langle \Phi_0 | e^{-i \sum_{l=0}^N \mathcal{H}_l t} | \Phi_0 \rangle \\ &= \prod_{l=0}^N \langle \Psi_0 | e^{-i \mathcal{H}_l t} | \Psi_0 \rangle_l. \end{aligned}$$

The full optical response in real time domain is obtained by a product of the susceptibilities in the different angular momentum channels. This is only true if, during the dynamics, different angular momenta do not couple with each other. The latter is indeed true if electron-electron interactions are neglected.

For the first-quantized Hamiltonian in angular momentum basis and in real space we have

$$\hat{h}_l(r) = - \left[\frac{\partial^2}{\partial r^2} + \frac{1}{r} \frac{\partial}{\partial r} \right] + \frac{l^2}{r^2} + V^{X-e}(r),$$

where the subscript $l \in \mathbb{N}$ denotes the angular momentum index and r is the radial distance. Because of the kinetic energy (Laplacian) in polar coordinates an additional centrifugal term appears in the Hamiltonian. In Fig. 4.4 the optical response in real time domain and the corresponding absorption spectra are depicted for several Fermi energies. Different colours correspond to more and more different angular momentum channels being taken into account. In the numerics, we only have a bound state in the $l = 0$ channel. For higher angular momenta the exciton-electron potential $V^{X-e}(r)$ is too weak to overcome the extra centrifugal term. Overall, the effect of the p , d , f channels is negligible (assuming an angular momentum independent light-matter coupling) and we also visually verify that the result has more or less converged when we take into account angular momenta up to $l = 3$.

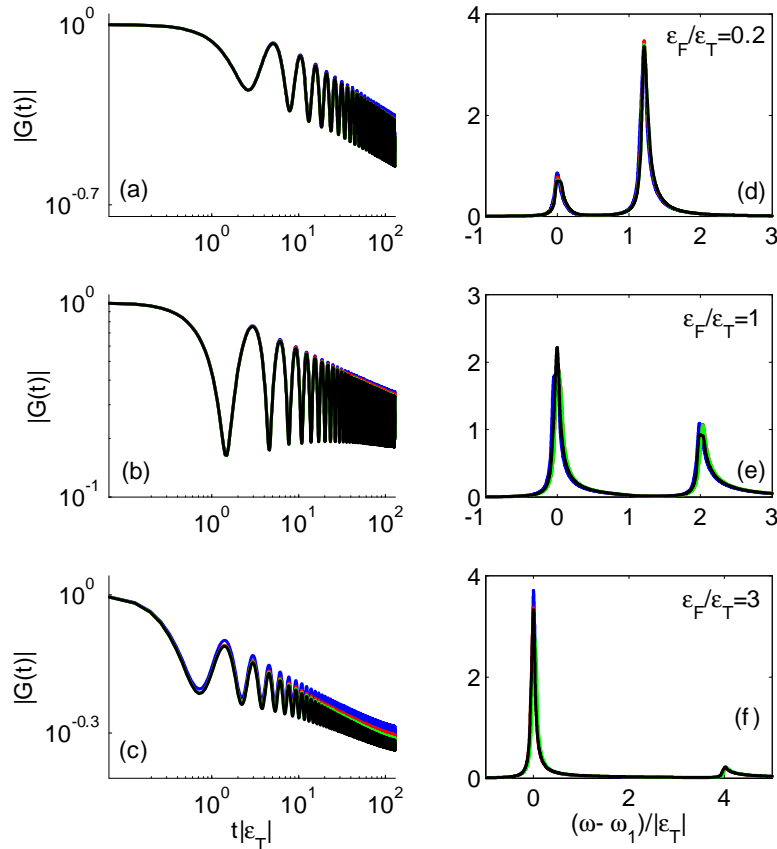


Figure 4.4: (a-c) Modulus of the optical response function in real time for increasing Fermi energy. Different colours denote higher angular momenta (blue: $l = 0$, red: $l + p$, green: $l + p + d$, black: $l + p + d + f$). (d-f) Corresponding absorption spectra obtained by means of the Laplace transform.

We indeed do not expect the $l \neq 0$ channels to contribute significantly. The non-trivial

many-body physics in the optical response arises from the scattering of the plane waves onto the exciton potential. Because our potential was assumed to be short-ranged, the scattering of the $l \neq 0$ channels is expected to get less important. In particular, if we assume a contact potential for the electron-exciton scattering,

$$V^{X-e}(r) = V_0 \frac{\delta(r)}{2\pi r},$$

the relevant matrix elements needed in Eq. (4.5) are

$$\begin{aligned} \langle k | \hat{V} | q \rangle &= 2\pi \int dr r V^{X-e}(r) J_l(kr) J_l(qr) \\ &= V_0 \int dr \delta(r) J_l(kr) J_l(qr) \\ &= V_0 [J_l(kr)]_{r=0} [J_l(qr)]_{r=0}. \end{aligned}$$

Only the Bessel functions of zeroth order are different from zero in the origin and yield a finite non-zero matrix element for the scattering of the $l = 0$ states of the exciton potential. As long as the potential is short-ranged and tends to contact interaction, we thus indeed see that the $l \neq 0$ channels are not that important.

4.1.5 Finite temperature

The generalization of the optical response $G(t)$ in Eq. (4.4) towards finite temperatures has been theoretically established by Muzykantskii *et al.* [88]. It is given by

$$G(t) = \det \left[\hat{1} - \hat{n}_F + \hat{n}_F \hat{\lambda}(t) \right].$$

Here, \hat{n}_F is the Fermi-Dirac distribution at temperature T and $\hat{\lambda}$ has been defined in Eq. (4.5). In Fig. 4.5a we show the time evolution of $G(t)$ for a fixed Fermi energy $\varepsilon_F/\varepsilon_T = 1$, and for several temperatures T/ε_T .

For finite temperature, the time series are always seen to coincide with the zero temperature result (blue solid lines) for short times. However, deviations from the $T = 0$ start showing up at the time proportional to the inverse temperature, i.e. $t \sim T^{-1}$. For long times the finite temperature series decay exponentially to zero. Figure 4.5b depicts the corresponding absorption spectra. For $T = 0$ we have the same lineshape as in Fig. 4.2e. For increasing temperature, the spectral line shapes become broadened and tend to get more Lorentzian. As expected, increasing the temperature too much, causes the trion to disappear (for the highest temperature under consideration, a small shoulder around ω_1 under the exciton is still visible). In other words, the many-body phenomena of the Anderson orthogonality catastrophe and Fermi-edge singularity only exist thanks to the well-defined Fermi energy and the corresponding steep behaviour of the Fermi-Dirac distribution at the Fermi energy at zero-temperature.

4.2 Trion-polariton

We can now turn on the light-matter interaction between the cavity photon and the charged quantum well. The main quantity of interest is the photon spectral function, given by

$$D(\omega) = -\text{Im} \frac{1}{\omega - \omega_c + i|g_{LM}|^2 G(i\omega)}.$$

Here ω_c is the cavity mode energy and $G(i\omega)$ the Laplace transform of $G(t)$. The microcavity is assumed to be lossless and we only consider a single photon mode at normal incidence.

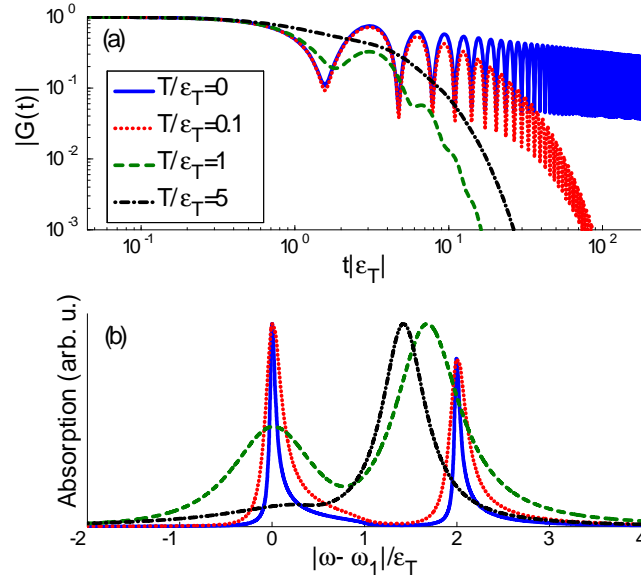


Figure 4.5: a) Time dependence of $|G(t)|$ for a fixed density $\varepsilon_F/\varepsilon_T = 1$ and for several temperatures $T/\varepsilon_T = 0, 0.1, 1, 5$. For finite T , the response function exponentially decays, with a decay time set by the inverse temperature. b) Absorption spectra obtained by Laplace transformation of the time series. Finite temperature causes a broadening of the absorption peaks and makes them more symmetric, i.e. Lorentzian.

From now on, we restrict our attention to the trion in the 2DEG absorption spectra at zero temperature. In particular, as the trion energy shifts with increasing electron density (see Fig. 4.1a), we can tune the photon into resonance with the trion for every density. The resulting lower polariton energy ε_{LP} is seen in Fig. 4.6 for two different values of the light-matter coupling, i.e. $g_{LM} = 0.5|\varepsilon_T|$ vs $g_{LM} = 3|\varepsilon_T|$. In both cases, we see a monotonic increase in the trion-polariton ‘Rabi splitting’ as a function of Fermi energy. This can be attributed to the gain of trion oscillator strength as the Fermi energy increases. For low electron density, the increase of the trion oscillator strength can be simply understood in terms of an increased trion-photon overlap [89]. However, there, a linear dependence of the oscillator as function of electron density has been observed, using a simplified three-level system to describe the exciton-trion-photon system. In recent experiments [20], a *decrease* of the Rabi splitting was however observed for higher electron density. Including hole recoil and electron-electron interactions could resolve these issues. In the subfigures (1-3) the polariton lineshapes (red solid) are depicted for some fixed Fermi energies, the values being indicated by the black dashed lines in the large figures. For comparison, the 2DEG absorption has also been depicted in blue dashed lines. For small light-matter coupling, the exciton does not influence the cavity mode. The lower polariton now truly corresponds to the trion-polariton as being a superposition of trion and photon. Note that in principle the lower polariton should have zero linewidth, but for visibility we gave it some small value. The other polariton modes intrinsically possess a finite linewidth due to the finite absorption of the 2DEG at the corresponding polariton energies. For larger light-matter coupling, the photon starts admixing with the exciton resulting in a non-zero quasiparticle shift at the lowest electron density under consideration. We also see a clearly visible polariton mode above the exciton threshold. Furthermore, in the right panel of Fig. 4.6(2) the middle polariton is seen to have an asymmetric lineshape with a large tail towards the low frequencies. This feature stems from the interplay between the two skewed lineshapes from both the trion and exciton and the fact that they both contribute equally to the polariton formation because of

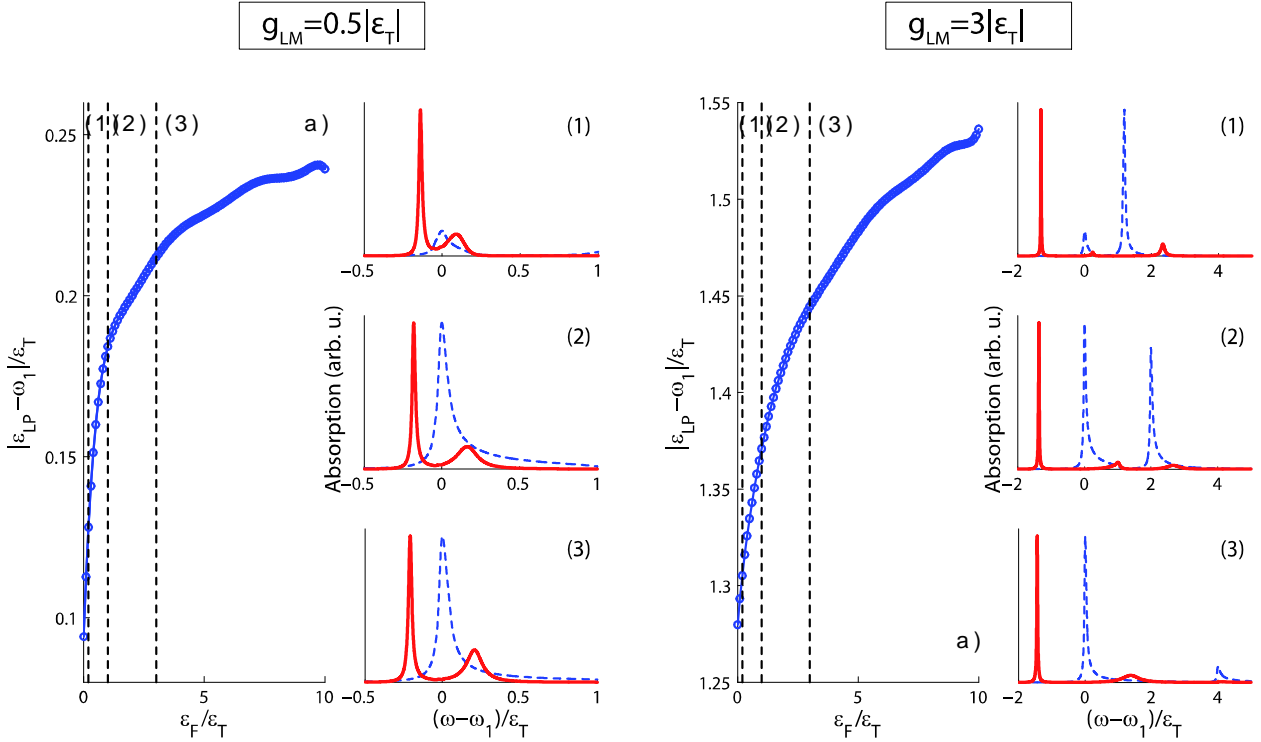


Figure 4.6: Left figure - a) Lower polariton energy as a function of Fermi energy, obtained by putting the cavity mode into resonance with the trion for all Fermi energies. The light-matter coupling was taken $g_{LM} = 0.5 |\epsilon_T|$. (1-3) depict the polariton lineshapes (red solid) for some fixed Fermi energies (black dashed lines in Fig. a). For reference, the 2DEG absorption is also shown in blue dashed lines. The exciton threshold is not visible because it lies at higher energies. Right figure: Same quantities as in left panel, but now for a light-matter coupling $g_{LM} = 3 |\epsilon_T|$. The larger light-matter coupling now admixes the photon with both the trion and the exciton, resulting in an upper polariton with an energy higher than the exciton energy. In (2) the middle polariton is seen to have an asymmetric lineshape, inherited from the 2DEG absorption.

their oscillator strengths being the same at the corresponding Fermi energy.

4.3 Spatial structure of the lower trion-polariton: towards the polariton blockade

A very appealing feature of microcavity polaritons is their strong optical nonlinearity, allowing the creation of an interacting polariton quantum ‘fluid’ [31]. In principle, the polariton interactions could lead to the so-called polariton blockade inside the microcavity if the nonlinearity is strong enough [32]. The latter is the phenomenon in which the energy of a polariton entering the cavity is shifted with an amount larger than the polariton linewidth, due to interaction with a polariton that was previously created inside the cavity. In this way, the incoming polariton is blocked from the cavity. In other words, only a single polariton is allowed at a time in the cavity, analogous to the photon blockade [90]. Unfortunately, in the current state of the art microcavities, the single photon nonlinearities are too weak in order to enter the polariton blockade regime.

It has been recently suggested that the electrons in the QW could enhance interactions between

the polaritons [20]. In the previous section, we have shown the lower trion-polariton to be the good quasi particle for a highly doped QW embedded in a planar microcavity. Because in the coherent light-matter superposition, the matter component of the polaritons is responsible for the interactions, it is instructive to investigate the spatial structure of the trion-polariton. In particular, here we will calculate the electron density in the lower polariton state through the electron-exciton density correlation function:

$$n_e(r) = \frac{\langle \text{LP} | \hat{n}_e(r) \hat{n}_X(0) | \text{LP} \rangle}{\langle \text{LP} | \hat{n}_X(0) | \text{LP} \rangle}, \quad (4.11)$$

with $\hat{n}(x) = \hat{\psi}^\dagger(x) \hat{\psi}(x)$ the density operator of the field ψ at position x . Because the exciton is assumed to be infinitely heavy, we can place it in the origin without loss of generality. Since we only consider s-wave scattering, the meaning of the spatial coordinate r is the relative radial distance from the electrons to the exciton center-of-mass. We start again from the unperturbed Fermi sea $|\Psi_0\rangle$ and consider the Hamiltonian \hat{V}_{LM} given by Eq. (4.1) as a small perturbation to the 2DEG. Using Kubo's response theory, we find that the lowest order contribution to the above correlation function is of second order in the perturbation, i.e. proportional to $|gA_L|^2$. It is given by

$$\langle \text{LP} | \hat{n}_e(r) \hat{n}_X(0) | \text{LP} \rangle \quad (4.12a)$$

$$= |gA_L|^2 \lim_{\eta \rightarrow 0^+} \lim_{t_0 \rightarrow -\infty} \int_{t_0}^t e^{\eta s} \int_{t_0}^s e^{\eta \tau} e^{i\omega_L(s-\tau)} \langle \Psi_0 | \hat{\psi}_X(0, s) \hat{n}_e(r, t) \hat{n}_X(0, t) \hat{\psi}_X^\dagger(0, \tau) | \Psi_0 \rangle ds d\tau + \text{h.c.}$$

$$= |gA_L|^2 \sum_{n,m} \phi_n(r) \phi_m^*(r) \int_{-\infty}^{\infty} g_{nm}(\omega) \frac{1}{\omega - (\omega_L - \bar{\varepsilon}_m)} \frac{1}{\omega - (\omega_L - \bar{\varepsilon}_n)} d\omega. \quad (4.12b)$$

Here, we adiabatically turned on the laser in order to find the stationary state of the electron density under the continuous wave excitation (see details in appendix C). The wave functions $\phi_n(r)$ are the single particle eigenstates of the Hamiltonian \bar{H} in position space, satisfying $\bar{H}\phi_n(r) = \bar{\varepsilon}_n\phi_n(r)$. The latter is defined in section 4.1.1. The matrix $g_{nm}(\omega)$ is given as

$$g_{nm}(\omega) = \frac{1}{\pi} \text{Re} \int_0^\infty e^{-i\omega t} g_{nm}(t) dt,$$

$$g_{nm}(t) = \sum_{k,q} \phi_n^*(k) \phi_m(q) \langle \Psi_0 | \hat{c}_q^\dagger e^{-i(\bar{H}-E_0)t} \hat{c}_k | \Psi_0 \rangle. \quad (4.13)$$

The expectation value in the above equation looks similar to an expression obtained in section 2.2.1 in chapter 1. This means we can again numerically compute the above expectation value taking determinants of the appropriate matrix, analogous to the same section 2.2.1 and moreover, our results on the electron density properly take into account the Anderson orthogonality catastrophe and the Fermi edge singularity physics.

The expectation value (4.11) should be calculated in the lower polariton state. In the resulting expression the polariton shows up through the laser frequency ω_L . In particular, we consider resonant continuous wave excitation, thus with the frequency of the laser resonant with the lower polariton energy ε_{LP} . Note that ε_{LP} is a free parameter in this calculation, but its actual value has been calculated in the previous section, see Fig. 4.6.

The exciton density in the lower polariton state, needed in Eq. (4.11), can be calculated analogously. It is found to be

$$\langle \hat{n}_X(0) \rangle = |gA_L|^2 \int_{-\infty}^{\infty} \frac{\mathcal{A}(\omega)}{(\omega - \omega_L)^2} d\omega,$$

where the absorption $\mathcal{A}(\omega)$ is given in Eq. (4.6).

The electron density along the radial direction and in the lower polariton state is shown in Fig. 4.7 for several Fermi energies and polariton energies. The trion Bohr radius a_T is taken as the lengthscale corresponding to the bound state $\psi(r) \sim \exp(-r/a_T)$ with energy ε_T . For the lowest Fermi energy, a small Rabi frequency (blue solid lines), defined as the energy difference between the lower polariton and the trion threshold ω_1 , is seen to increase the electron density at short distances from the exciton. This can be understood as follows: when the photon is annihilated and an exciton is created, the Fermi sea is shaken up due to the appearance of the exciton. For small Rabi frequency, it takes longer time for the exciton to be reconverted into a photon. This means that there is a longer time for the electrons in the Fermi sea to adjust themselves to the presence of the exciton: a screening cloud of electrons is able to build up near the exciton. The reason for the increase of electron density is the attractive exciton-electron potential. At distances much larger than the trion Bohr radius, the exciton does not affect the electron density as the ratio $n_e(r)/n_0 \xrightarrow{r \rightarrow \infty} 1$. Here, $n_0 = k_F^2/4\pi$ is the homogenous electron density for a spin polarized 2DEG. For larger Rabi frequency, there will be much less time for the electrons to reorganize; as soon as they start readjusting, the exciton has already disappeared and turned into a photon. This is seen by the green dashed-dotted line where the density tends to flatten. For large Fermi energies (comparable to or larger than the trion binding energy), the electron density does not depend too much on the Rabi frequency. We argue that the time it takes for the individual electrons to adjust to the presence of the scattering potential, is proportional to the inverse Fermi energy. The larger the Fermi energy, the less time it takes to reorganize the electrons at the Fermi level and the system will always be able to build up a screening cloud. Nevertheless, the absolute value of $n_e(r)/n_0$ decreases for increasing Fermi energy, because there is less time to screen the exciton. In all cases, the electron density oscillates and the envelope decays as $1/r^2$ at large distances, corresponding to the Friedel oscillations.

From the above, we see that there should be a frequency window in which the trion gets screened on a length scale comparable to the bare trion Bohr radius, making it a truly localized, electrically charged particle. The Rabi frequency should be small enough such that there is time for the electrons to form the trion, by binding to the exciton. Since the formation time typically goes as $1/\varepsilon_T$, one should maintain $\Omega_R < \varepsilon_T$. On the other hand, one should avoid running into the weak coupling regime by taking the Rabi frequency too small.

This analysis could give a first clue towards the nature of interactions amongst trion-polaritons. In the case of exciton-polaritons, the exciton can be viewed as a charged dipole and one expects the interaction between exciton-polaritons being mediated through some dipole-dipole interaction (only scaling with r^{-6} , thus a very weak interaction). However, Ciuti *et al.* have shown that the exchange interactions between the electrons and hole for different excitons is the dominant mechanism for exciton-exciton interactions [23]. Other mechanisms for exciton-polariton interactions have been investigated in Ref. [25]. Our results indicate that the trionic component of the trion-polariton could behave as a point charge, with the size of the charge comparable to the bare trion Bohr radius. This implies the interaction between trion-polaritons to be mediated through the Coulomb interaction between two point charges, scaling like r^{-1} , which is a much stronger interaction as compared to e.g. dipole-dipole interaction. The 2DEG could thus indeed serve as a way to increase the optical nonlinearity.

Here, we have presented the trion-polariton quasi particle, as the result from the coherent coupling between the cavity mode and the trion excitation in the quantum well. We addressed a few properties for this quasiparticle, e.g. lineshapes, Rabi splitting and electron density profile of the matter component. Of course, we have made some major simplifications (under which we could do the exact treatment of the optical response). However, the most prominent one is the neglect of electron interactions. We believe the inclusion of this physics could solve some issues,

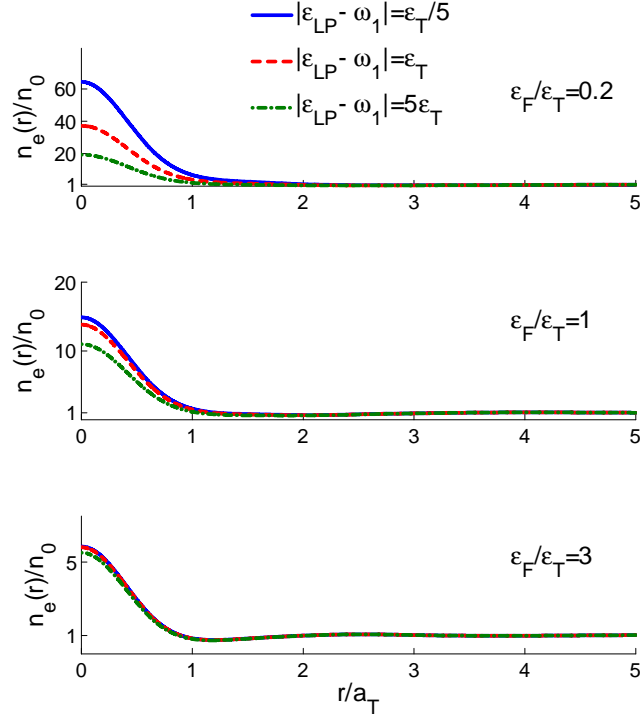


Figure 4.7: Electron density in the lower polariton state (normalized with respect to the unperturbed density $n_0 = k_F^2/4\pi$) as a function of radial distance to the exciton center-of-mass. At large distances, the density stays unperturbed as the correlation function always asymptotically goes to 1. For a high density 2DEG, the electron density does not depend too much on the Rabi frequency because the electrons screen the exciton on a time scale of the inverse Fermi energy. For smaller Fermi energy, a low Rabi frequency still allows the electrons to screen the exciton. For higher Rabi frequency, the electrons do not have enough time to react onto the presence of the exciton so that the electron density is unperturbed.

as for example the decrease of the trion linewidth for increasing electron density. Also, the single particle trion binding energy would then become a function of electron density. But most importantly, in the build-up of the screening cloud surrounding the exciton, a self-consistent treatment taking into account the electron-electron interactions should be implemented. One can easily imagine the electrons repelling each other as the density becomes to high, which in turn would decrease the overall electron density around the exciton. In that case, it might turn out that there is no net charge build-up near the exciton.

Chapter 5

Closing

5.1 Conclusion and outlook

In this work we have studied a system composed of a planar microcavity embedding a quantum well, where the latter contains a quantum degenerate *non-interacting* electron gas. The strong coupling between the optical mode inside the cavity and the quantum well results in the formation of the polariton quasi particles and we investigated the properties of these polaritons in a wide range of electron densities. While the coupling with the electromagnetic field mode is rather straightforward (if polariton-polariton interactions are neglected), the calculation of the optical properties of the electron gas turns out to be the difficult part of the problem.

In chapter 2 we considered the limit of a high density electron gas, i.e. where the average inter-electron distance is less than the exciton Bohr radius. We showed that the optical response of the electron gas can be described by the dynamics of the 2DEG after a sudden quench with an impurity, where the role of the impurity is played by the valence band hole that appears due to interband absorption of a photon. Absorption spectra exhibiting the Fermi edge singularity and Anderson Orthogonality Catastrophe, resulting in asymmetric lineshapes, were obtained in agreement with analytical predictions. For what concerns the effect on the polaritons, we found that the lower polariton lineshape remains a delta function, while the upper polariton inherits the asymmetry from the 2DEG absorption. Tuning the cavity mode in resonance with the excitonic threshold, we obtained a monotonic decrease of the Rabi splitting as a function of electron density, due to the decrease of oscillator strength. Furthermore, in the resonant case, but changing the light-matter coupling strength, we found that a small coupling only probes the long time response of the 2DEG after the quench. Then, the system can be described *as if* the exciton-polariton is a two-level system, but with a renormalized Rabi frequency due to the presence of the charge carriers. For Rabi frequencies of the order of the distance between the singular and non-singular threshold, the short time behaviour is probed and both thresholds determine the polariton properties. This effect is seen in the photonic/excitonic spectral weights. Finally, the lower polariton mass increases for increasing electron density, because of the reduced Rabi frequency. For a blue detuned photon with respect to the excitonic threshold, the polariton mass turns out to be (slightly) heavier than expected on the basis of a simple two-level system.

Chapter 3 elucidated the role of the finite mass of the valence band hole on the polariton. By neglecting the many-body Fermi edge physics, a single particle description of the 2DEG absorption is obtained. The results in this chapter are valid only if we consider timescales shorter than the Fermi time. We recover the Mahan exciton: a stable exciton state for low densities, turning into a metastable state if the electron density is increased. The coupling with the optical mode results in the Mahan polaritons. To estimate their lifetime, we derived a generalized Wannier equation including a lowest order relaxation mechanism for the valence

band hole due to intraband pair creation. The linewidth of the polaritons was found to increase for increasing electron density. On the other hand, if the Rabi splitting could be enhanced such that it becomes larger than the hole recoil energy, the lower polariton mode becomes stable again. Its lifetime is then only determined by the cavity properties.

Chapter 4 is concerned with the low-density 2DEG (average inter-electron distance larger than exciton Bohr radius). We introduced the trion as an electron bound to an exciton and we computed the optical response in the same formalism as the first chapter. Again, we found asymmetric lineshapes, but now we have two singular thresholds, resp. the trionic and excitonic threshold. For increasing electron density, oscillator strength is transferred from the exciton at zero density towards the trion at higher densities. For the cavity mode resonant with the trion, we found an increasing Rabi splitting as a function of electron density, the consequence of the increased oscillator strength of the trion. We also briefly discussed the effects of different angular momentum channels in the 2DEG and finite temperature on the optical absorption. Finally, we investigated the stationary electron density profile around the exciton in the lower polariton state. An increase in the electron density near the exciton is always found and the length scale at which the exciton gets screened is comparable to the unperturbed trion Bohr radius. For large electron densities, the density profile did not depend too much on the Rabi frequency. For low electron densities, the largest build-up near the exciton was seen for the lowest Rabi frequencies.

A major simplification in this work is the neglect of electron-electron interactions in the 2DEG. Although some analytical results have been obtained on the Anderson Orthogonality Catastrophe in an interacting electron gas [91], computationally little has been done. The remaining challenge is to treat both the many-body physics of the Fermi edge singularity and Anderson Orthogonality Catastrophe and the electron-electron interactions at the same footing. Currently, we are working to include electron interactions in the dynamical Hartree-Fock approximation. We expect a faster decrease of the many-body overlap in time. Whether this decay is power law like or exponential is still an open question. Most importantly, to better estimate the role of the 2DEG in enhancing polariton interactions, we should again calculate the exciton-electron density correlation. For example, it might happen that the repulsive electron interaction tends to decrease the overall charge build-up near the exciton, making the trion a less localized particle than one expects on the basis of a non-interacting calculations. This could dramatically affect the nature of the polariton interactions.

5.2 Scientific contributions

Peer-reviewed articles

- M. Baeten and M. Wouters, Phys. Rev. B **91**, 115313 (2015).
- M. Baeten and M. Wouters, Phys. Rev. B **89**, 245301 (2014).

Conference contributions

- M. Baeten and M. Wouters, *Polaritons at the Fermi edge: strong light-matter coupling between a cavity photon and a highly degenerate 2D electron gas*, The 7-th International Conference on Spontaneous Coherence in Excitonic Systems, 21-25 April 2014, Hakone, Japan. *Oral contribution*.
- M. Baeten and M. Wouters, *Fermi edge polaritons in a highly degenerate 2D electron gas*, 14-th Conference on Physics of Light-Matter Coupling in Nanostructures, 27-31 May

2013, Hersonissos, Crete. *Oral contribution.*

- M. Baeten and M. Wouters, *Fermi edge polaritons in a highly degenerate 2D electron gas: a diagrammatic theory*, Belgian Physical Society General Scientific Meeting, 22 May 2013, Louvain-La-Neuve, Belgium. *Poster presentation.*
- M. Baeten and M. Wouters, *Theory of Polaritons in a highly degenerate 2DEG*, Tweedaagse van de Theoretische en Mathematische Fysica, 8-9 April 2013, Nieuwpoort, Belgium. *Poster presentation.*

Appendix A

Angular-momentum basis for the optical susceptibility

A.1 Matrix $\lambda_{\mathbf{k}\mathbf{q}}(t)$ in angular momentum basis

Given is the expression for the matrix elements $\lambda_{\mathbf{k}\mathbf{q}}(t)$, needed to calculate the 2DEG optical response:

$$\lambda_{\mathbf{k}\mathbf{q}}(t) = \sum_{\mathbf{n}} \phi_{\mathbf{n}}(\mathbf{k}) \phi_{\mathbf{n}}^*(\mathbf{q}) e^{i(\bar{\varepsilon}_{\mathbf{n}} - \varepsilon_{\mathbf{k}})t}.$$

We want to rewrite it into the basis of angular momentum eigenstates,

$$\begin{aligned} \lambda_{km,k'm'} &= \langle km | \lambda | k'm' \rangle \\ &= \int d\mathbf{K} \int d\mathbf{K}' \langle km | \mathbf{K} \rangle \langle \mathbf{K} | \lambda | \mathbf{K}' \rangle \langle \mathbf{K}' | k'm' \rangle, \end{aligned} \quad (\text{A.1})$$

where k is the modulus of the plane wave state $|\mathbf{k}\rangle$ and $m \in \mathbb{N}$ the corresponding angular momentum. We can also write the wave functions $\phi_{\mathbf{n}}(\mathbf{k})$ in terms of a radial part, depending on the modulus of $|\mathbf{k}|$ only and an angular part, i.e.

$$\phi_{\mathbf{n}}(\mathbf{k}) = \phi_{n,l}(k) \frac{e^{il\theta_k}}{\sqrt{2\pi}}.$$

The matrix λ in the plane wave representation now becomes a sum over all angular momentum states:

$$\lambda_{\mathbf{k}\mathbf{q}}(t) = \sum_{n,l} \phi_{n,l}(k) \phi_{n,l}^*(q) \frac{e^{il(\theta_{\mathbf{k}} - \theta_{\mathbf{q}})}}{2\pi} e^{i(\bar{\varepsilon}_n - \varepsilon_k)t}.$$

We still need the overlaps $\langle km | \mathbf{K} \rangle$ in Eq. (A.1). Using

$$\begin{aligned} \langle \mathbf{r} | \mathbf{K} \rangle &= \frac{e^{i\mathbf{K}\mathbf{r}}}{2\pi} \\ \langle \mathbf{r} | km \rangle &= J_m(kr) \frac{e^{im\theta_{\mathbf{r}}}}{\sqrt{2\pi}}, \end{aligned}$$

with $J_m(kr)$ the Bessel function of order m , one has

$$\begin{aligned}
\langle \mathbf{K} | km \rangle &= \int d\mathbf{r} \langle \mathbf{K} | \mathbf{r} \rangle \langle \mathbf{r} | km \rangle \\
&= \frac{1}{2\pi} \int_0^\infty dr r \int_0^{2\pi} d\theta_{\mathbf{r}} e^{-iKr \cos(\theta_{\mathbf{K}} - \theta_{\mathbf{r}})} J_m(kr) \frac{e^{im\theta_{\mathbf{r}}}}{\sqrt{2\pi}} \\
&\stackrel{\phi = \theta_{\mathbf{r}} - \theta_{\mathbf{K}}}{=} \frac{1}{2\pi} \int_0^\infty dr r \int_0^{2\pi} d\phi e^{-iKr \cos \phi} J_m(kr) \frac{e^{im(\phi + \theta_{\mathbf{K}})}}{\sqrt{2\pi}} \\
&= \frac{1}{2\pi} \frac{e^{im\theta_{\mathbf{K}}}}{\sqrt{2\pi}} \int_0^\infty dr r \int_0^{2\pi} d\phi e^{i(m\phi - Kr \cos \phi)} J_m(kr) \\
&= \frac{1}{2\pi} \frac{e^{im\theta_{\mathbf{K}}}}{\sqrt{2\pi}} \int_0^\infty dr r 2\pi (-i)^m J_m(Kr) J_m(kr) \\
&= \frac{e^{im\theta_{\mathbf{K}}}}{\sqrt{2\pi}} (-i)^m \int_0^\infty dr r J_m(Kr) J_m(kr) \\
&= \frac{e^{im\theta_{\mathbf{K}}}}{\sqrt{2\pi}} (-i)^m \frac{\delta(K - k)}{k}
\end{aligned}$$

We thus obtain

$$\begin{aligned}
&\lambda_{km, k'm'} \\
&= \int d\mathbf{K} \int d\mathbf{K}' \langle km | \mathbf{K} \rangle \langle \mathbf{K} | \lambda | \mathbf{K}' \rangle \langle \mathbf{K}' | k'm' \rangle \\
&= \int_0^\infty dK K \int_0^{2\pi} d\theta_{\mathbf{K}} \int_0^\infty dK' K' \int_0^{2\pi} d\theta_{\mathbf{K}'} \\
&\quad \times \frac{1}{\sqrt{2\pi}} i^m e^{-im\theta_{\mathbf{K}}} \frac{\delta(K - k)}{k} \lambda_{\mathbf{K}\mathbf{K}'}(t) \frac{1}{\sqrt{2\pi}} (-i)^{m'} e^{im'\theta_{\mathbf{K}'}} \frac{\delta(K' - k')}{k'} \\
&= \int_0^\infty dK K \int_0^{2\pi} d\theta_{\mathbf{K}} \int_0^\infty dK' K' \int_0^{2\pi} d\theta_{\mathbf{K}'} \\
&\quad \times \frac{1}{\sqrt{2\pi}} i^m e^{-im\theta_{\mathbf{K}}} \frac{\delta(K - k)}{k} \sum_{n,l} \phi_{n,l}(K) \phi_{n,l}^*(K') \frac{e^{il(\theta_{\mathbf{K}} - \theta_{\mathbf{K}'})}}{2\pi} e^{i(\bar{\varepsilon}_n - \varepsilon_K)t} \frac{1}{\sqrt{2\pi}} (-i)^{m'} e^{im'\theta_{\mathbf{K}'}} \frac{\delta(K' - k')}{k'} \\
&= \sum_{n,l} \phi_{n,l}(k) \phi_{n,l}^*(k') e^{i(\bar{\varepsilon}_n - \varepsilon_k)t} \frac{i^m (-i)^{m'}}{(2\pi)^2} \int_0^{2\pi} d\theta_{\mathbf{k}} e^{-i(m-l)\theta_{\mathbf{k}}} \int_0^{2\pi} d\theta_{\mathbf{k}'} e^{i(m'-l)\theta_{\mathbf{k}'}} \\
&= \delta_{m,m'} \sum_n \phi_{n,m}(k) \phi_{n,m}^*(k') e^{i(\bar{\varepsilon}_n - \varepsilon_k)t} \\
&= \delta_{m,m'} \lambda_{kk'}^{(m)}(t),
\end{aligned}$$

where we introduced

$$\lambda_{kk'}^{(m)}(t) = \sum_n \phi_{n,m}(k) \phi_{n,m}^*(k') e^{i(\bar{\varepsilon}_n - \varepsilon_k)t}.$$

In angular momentum basis, the matrix λ is decoupled into different angular momentum states and thus becomes block diagonal in this representation.

A.2 Light-matter coupling in the electron-hole basis

Here, we show that the optical response function in Chapter 2 only couples to the zero-angular momentum states of the electron gas. Using the so-called Jacobi-Anger expansion for writing

a plane wave into angular momentum states, we have

$$\begin{aligned}\hat{c}_{\mathbf{K}}^\dagger|0\rangle &= |\mathbf{K}\rangle = \sum_m i^m e^{-im\theta_{\mathbf{K}}} |Km\rangle = \sum_m i^m e^{-im\theta_{\mathbf{K}}} \hat{c}_{Km}^\dagger|0\rangle \\ \Rightarrow \hat{c}_{\mathbf{K}}^\dagger &= \sum_m i^m e^{-im\theta_{\mathbf{K}}} \hat{c}_{Km}^\dagger\end{aligned}$$

This can be used into the second quantized formulation for the electron-hole optical susceptibility Eq. (2.4):

$$\begin{aligned}\Pi(t) &= e^{iE_0t} e^{-i\varepsilon^h t} \sum_{\mathbf{p}\mathbf{p}'>k_F} g_{\mathbf{p}} g_{\mathbf{p}'}^* \langle \Psi_0 \hat{c}_{\mathbf{p}} | e^{-i\tilde{H}t} | \hat{c}_{\mathbf{p}'}^\dagger \Psi_0 \rangle \\ &= e^{iE_0t} e^{-i\varepsilon^h t} \sum_{m,l} i^m (-i)^l \sum_{\mathbf{p}\mathbf{p}'>k_F} e^{-im\theta_{\mathbf{p}'}} e^{il\theta_{\mathbf{p}}} g_{\mathbf{p}} g_{\mathbf{p}'}^* \langle \Psi_0 \hat{c}_{p'l} | e^{-i\tilde{H}t} | \hat{c}_{p'm}^\dagger \Psi_0 \rangle \\ &\propto \sum_{m,l} i^m (-i)^l \int_{k_F}^\infty dp p \int_0^{2\pi} d\theta_p \int_{k_F}^\infty dp' p' \int_0^{2\pi} d\theta_{p'} e^{-im\theta_{p'}} e^{il\theta_p} g_{\mathbf{p}} g_{\mathbf{p}'}^* \langle \Psi_0 \hat{c}_{p'l} | e^{-i\tilde{H}t} | \hat{c}_{p'm}^\dagger \Psi_0 \rangle\end{aligned}$$

Assuming a constant light-matter coupling in momentum space, i.e. $g_{\mathbf{p}} = g$, we can do the angular integrals, yielding

$$\begin{aligned}\Pi(t) &\propto |g|^2 \sum_{m,l} i^m (-i)^l \int_{k_F}^\infty dp p \int_{k_F}^\infty dp' p' \delta_{m,0} \delta_{l,0} \langle \Psi_0 \hat{c}_{p'l} | e^{-i\tilde{H}t} | \hat{c}_{p'm}^\dagger \Psi_0 \rangle \\ &= |g|^2 \int_{k_F}^\infty dp p \int_{k_F}^\infty dp' p' \langle \Psi_0 \hat{c}_{p0} | e^{-i\tilde{H}t} | \hat{c}_{p'0}^\dagger \Psi_0 \rangle\end{aligned}$$

It is thus sufficient to restrict ourselves to the $l = 0$ channel only. The other angular momentum channels do not contribute in the optical response of the electron gas.

Appendix B

Dynamical self energy for the valence band hole

In this section we derive the expression for the Hamiltonian in Eq. (3.7).

With the assumption of a frequency-independent screened electron-hole Coulomb interaction, from the ladder diagrams, a Wannier equation for the vertex factor $P(\mathbf{k}, i\omega)$ can be found along the lines of Ref. [72]. This integral equation for the vertex factor $P(\mathbf{k}, i\omega)$ is given by

$$F^{-1}(\mathbf{k}, i\omega) P(\mathbf{k}, i\omega) - \frac{1}{S} \sum_{\mathbf{k}_1} V_{\mathbf{k}-\mathbf{k}_1} P(\mathbf{k}_1, i\omega) = g. \quad (\text{B.1})$$

The solution of this equation yields the photon self energy by the following relation

$$\Pi(i\omega) = \frac{g}{S} \sum_{\mathbf{k}} P(\mathbf{k}, i\omega),$$

where for simplicity we have set the photon momentum equal to zero. The function $F(\mathbf{k}, i\omega)$ is given by the Matsubara summation over the internal fermionic frequency $i\nu_n$ of the electron and hole propagators, defined in Fig. 3.1 Because we consider a zero photon momentum, only electrons and holes with opposite momentum contribute. Hence we have

$$F(\mathbf{k}, i\omega) = -\frac{1}{\beta} \sum_{i\nu_n} G_e(\mathbf{k}, i\omega - i\nu_n) G_h(-\mathbf{k}, i\nu_n). \quad (\text{B.2})$$

For the electron we use the free Green's function

$$G_e(\mathbf{k}, i\nu_n) = \frac{1}{i\nu_n - \xi_{\mathbf{k}}^e},$$

with $\xi_{\mathbf{k}}^e = \varepsilon_{\mathbf{k}}^e + \Sigma_e(\mathbf{k}) - \mu_e$. Here, $\varepsilon_{\mathbf{k}}^e = \hbar^2 k^2 / 2m_e$ is the single particle dispersion in the parabolic mass approximation and $\Sigma_e(\mathbf{k})$ stands for the screened exchange interaction of the optically excited electron with the Fermi sea. Also the electron chemical potential μ_e is renormalized due to exchange interaction.

For the hole Green's function, we include the interactions with the electron Fermi sea perturbatively as follows, see Fig. 3.3:

$$G_h(\mathbf{k}, i\nu_n) = G_h^0(\mathbf{k}, i\nu_n) + G_h^0(\mathbf{k}, i\nu_n) \Sigma^{RPA}(\mathbf{k}, i\nu_n) G_h^0(\mathbf{k}, i\nu_n).$$

Here, for the dynamical self energy Σ^{RPA} , describing hole relaxation that is responsible for a finite polariton lifetime, we use the 2D RPA result. The free hole Green's function is given by

$$G_h^0(\mathbf{k}, i\nu_n) = \frac{1}{i\nu_n - \xi_{\mathbf{k}}^h}.$$

The hole dispersion is also assumed to be quadratic, so $\xi_{\mathbf{k}}^h = \hbar^2 k^2 / 2m_h - \mu_h$. No exchange contribution shows up because we consider a single hole ($\mu_h = 0$).

In order to be able to perform the Matsubara summation in Eq. (B.2) exactly, we further approximate the RPA result to lowest order in the Lindhard polarization ('1 intraband electron-hole bubble'), so only emission of a single intraband electron-hole pair is taken into account:

$$\Sigma^{RPA}(\mathbf{k}, i\nu_n) = \Sigma_{1 \text{ bubble}}(\mathbf{k}, i\nu_n) + \mathcal{O}(2 \text{ bubbles}).$$

Using the 2D expression of the Lindhard polarization function, the dynamical self energy is given by

$$\Sigma_{1 \text{ bubble}}^h(\mathbf{k}, i\nu_n) = -\frac{2}{S^2} \sum_{\mathbf{q}, \mathbf{K}} (V_{\mathbf{q}}^s)^2 [n_F(\varepsilon_{\mathbf{K}}^e) - n_F(\varepsilon_{\mathbf{K}+\mathbf{q}}^e)] \frac{1 - n_F[\xi_{\mathbf{k}-\mathbf{q}}^h] + n_B(\varepsilon_{\mathbf{K}+\mathbf{q}}^e - \varepsilon_{\mathbf{K}}^e)}{i\nu_n - \xi_{\mathbf{k}-\mathbf{q}}^h - \varepsilon_{\mathbf{K}+\mathbf{q}}^e + \varepsilon_{\mathbf{K}}^e}.$$

Here, the exchange correction to the electron energy was neglected to simplify the subsequent calculations. Furthermore, the double summation runs over the center-off-mass momentum and relative wavevector of the intraband electron-hole pair, resp. \mathbf{q}, \mathbf{K} .

Combining the expressions we can do the Matsubara sum over $i\nu_n$. The result is given by

$$F(\mathbf{k}, i\omega) = S_0 \left(1 + \frac{S_1}{S_0} \right), \quad (\text{B.3})$$

where we have

$$S_0(\mathbf{k}, i\omega) = \frac{1 - n_F(\xi_{\mathbf{k}}^e) - n_F(\xi_{-\mathbf{k}}^h)}{i\omega - \xi_{-\mathbf{k}}^h - \xi_{\mathbf{k}}^e}. \quad (\text{B.4})$$

This is the same expression as in Eq. (3.2) in Chapter 3. Furthermore, we have

$$\frac{S_1(\mathbf{k}, i\omega)}{S_0(\mathbf{k}, i\omega)} = \frac{2}{S^2} \sum_{\mathbf{q}, \mathbf{K}} (V_{\mathbf{q}}^s)^2 n_F(\varepsilon_{\mathbf{K}+\mathbf{q}}^e) [1 - n_F(\varepsilon_{\mathbf{K}}^e)] \times \left\{ \begin{aligned} & \frac{1}{1 - n_F(\xi_{\mathbf{k}}^e)} \frac{1}{-\xi_{-\mathbf{k}}^h - (-i\omega + \xi_{\mathbf{k}}^e)} \frac{1}{-\xi_{-\mathbf{k}}^h - (-\xi_{-\mathbf{k}+\mathbf{q}}^h + \varepsilon_{\mathbf{K}+\mathbf{q}}^e - \varepsilon_{\mathbf{K}}^e)} \\ & + \frac{1}{1 - n_F(\xi_{\mathbf{k}}^e)} \frac{1}{[-\xi_{-\mathbf{k}}^h - (-\xi_{-\mathbf{k}+\mathbf{q}}^h + \varepsilon_{\mathbf{K}+\mathbf{q}}^e - \varepsilon_{\mathbf{K}}^e)]^2} \\ & - \frac{i\omega - \xi_{-\mathbf{k}}^h - \xi_{\mathbf{k}}^e}{1 - n_F(\xi_{\mathbf{k}}^e)} \frac{n_F(-\xi_{-\mathbf{k}+\mathbf{q}}^h + \varepsilon_{\mathbf{K}+\mathbf{q}}^e - \varepsilon_{\mathbf{K}}^e)}{-\xi_{-\mathbf{k}+\mathbf{q}}^h + \varepsilon_{\mathbf{K}+\mathbf{q}}^e - \varepsilon_{\mathbf{K}}^e + i\omega - \xi_{\mathbf{k}}^e} \frac{1}{(-\xi_{-\mathbf{k}+\mathbf{q}}^h + \varepsilon_{\mathbf{K}+\mathbf{q}}^e - \varepsilon_{\mathbf{K}}^e + \xi_{-\mathbf{k}}^h)^2} \end{aligned} \right\}$$

Upon analytical continuation $i\omega \rightarrow \omega - \mu_e - \mu_h + i\eta^+$ only the last line yields an imaginary part and thus the lifetime of the hole. The other terms correspond to the energy shift, but these are currently not of interest. One has

$$\text{Im} \frac{S_1}{S_0} = \frac{2\pi}{S^2} \frac{\omega - \varepsilon_{-\mathbf{k}}^h - \varepsilon_{\mathbf{k}}^e - \Sigma_e(\mathbf{k})}{1 - n_F(\xi_{\mathbf{k}}^e)} \sum_{\mathbf{q}, \mathbf{K}} \frac{(V_{\mathbf{q}}^s)^2}{(\varepsilon_{-\mathbf{k}+\mathbf{q}}^h - \varepsilon_{\mathbf{K}+\mathbf{q}}^e + \varepsilon_{\mathbf{K}}^e - \varepsilon_{-\mathbf{k}}^h)^2} \times n_F(\varepsilon_{\mathbf{K}+\mathbf{q}}^e) [1 - n_F(\varepsilon_{\mathbf{K}}^e)] n_F(-\varepsilon_{-\mathbf{k}+\mathbf{q}}^h + \varepsilon_{\mathbf{K}+\mathbf{q}}^e - \varepsilon_{\mathbf{K}}^e) \delta[\omega - \varepsilon_{-\mathbf{k}+\mathbf{q}}^h + \varepsilon_{\mathbf{K}+\mathbf{q}}^e - \varepsilon_{\mathbf{K}}^e - \varepsilon_{-\mathbf{k}}^h - \Sigma_e(\mathbf{k})].$$

where the delta-function expresses conservation of energy and momentum. The 4-fold summation (modulus and angular part for each two-dimensional wave vector) can be elaborated further to a two-dimensional integral which we then compute numerically. This leads to the following result (all energies expressed in exciton Rydbergs $R_X = \hbar^2 / 2\mu a_X^2$, with μ the reduced mass of the electron-hole pair):

$$\text{Im} \frac{S_1}{S_0} = \Xi(\mathbf{k}, \omega) \frac{\Sigma_{hole}(\mathbf{k})}{\omega - k^2 - \Sigma_e(\mathbf{k})} \quad (\text{B.5})$$

where the Pauli blocking factor $\Xi(\mathbf{k}, \omega)$ reads

$$\Xi(\mathbf{k}, \omega) = \Theta(k > k_F) \Theta\left(\omega > \frac{k^2}{1 + m_e/m_h} + \Sigma_e(\mathbf{k})\right). \quad (\text{B.6})$$

Here the hole self energy is

$$\begin{aligned} & \Sigma_{hole}(\mathbf{k}, \omega) \quad (\text{B.7}) \\ = & \frac{1}{\pi} \frac{m_e}{\mu} \int_0^\infty dq \int_0^\pi d\theta \frac{\sqrt{k_F^2 - a - K_{\min}^2} - \sqrt{\max(K_{\min}, k_F)^2 - K_{\min}^2}}{[q + s(q)]^2} \Theta(a < 0) \Theta(k_F^2 - a > K_{\min}^2) \end{aligned}$$

with $s(q)$ the inverse screening length as defined in Ref. [83]. The functions $a(\mathbf{k}, q, \theta)$ and $K_{\min}(\mathbf{k}, q, \theta)$ are given by

$$\begin{aligned} a(\mathbf{k}, q, \theta) &= \frac{m_e}{m_h} q^2 - 2 \frac{m_e}{m_h} k q \cos \theta + \frac{m_e}{\mu} (k^2 - \omega + \Sigma_e(\mathbf{k})) \\ K_{\min}(\mathbf{k}, q, \theta) &= \frac{1}{2q} |a(\mathbf{k}, q, \theta) - q^2| \end{aligned}$$

In order to obtain the Wannier equation, the inverse of the function $F(\mathbf{k}, i\omega)$ in Eq. (B.3) was needed. Combining Eqs. (B.3) and (B.5) we find

$$F^{-1}(\mathbf{k}, \omega) = S_0^{-1} \left(1 + i \text{Im} \frac{S_1}{S_0}\right)^{-1} = (\omega - k^2 - \Sigma_e(\mathbf{k})) \left(1 + i \Xi(\mathbf{k}) \frac{\Sigma_{hole}(\mathbf{k})}{\omega - k^2 - \Sigma_e(\mathbf{k})}\right)^{-1}.$$

For a small hole self energy, we can use the following Taylor expansion: $1/(1+x) \approx 1-x$ for $x \ll 1$. Identifying $x = i \Xi(\mathbf{k}) \Sigma_{hole}(\mathbf{k}) / (\omega - k^2 - \Sigma_e(\mathbf{k}))$ we obtain

$$\begin{aligned} F^{-1}(\mathbf{k}, \omega) &= (\omega - k^2 - \Sigma_e(\mathbf{k})) \left(1 - i \Xi(\mathbf{k}) \frac{\Sigma_{hole}(\mathbf{k})}{\omega - k^2 - \Sigma_e(\mathbf{k})}\right) \\ &= \omega - k^2 - \Sigma_e(\mathbf{k}) - i \Xi(\mathbf{k}) \Sigma_{hole}(\mathbf{k}). \end{aligned}$$

Plugging this expression into Eq. (B.1) the identification with Eq. (3.7) is straightforward. It is worth noting that the Taylor series is consistent with the expansion of the RPA self energy to lowest order in the Lindhard polarization.

Appendix C

Stationary electron distribution in the lower trion-polariton state

Here, we calculate the stationary spatial electron distribution in the lower trion-polariton state $|\text{LP}\rangle$:

$$n_e(\mathbf{r}) = \frac{\langle \text{LP} | \hat{n}_e(\mathbf{r}) \hat{n}_X(\mathbf{0}) | \text{LP} \rangle}{\langle \text{LP} | \hat{n}_X(\mathbf{0}) | \text{LP} \rangle},$$

where $\hat{n}(\mathbf{r}) = \hat{\psi}^\dagger(\mathbf{r}) \hat{\psi}(\mathbf{r})$ is the density operator. Because the exciton is assumed infinitely heavy, we can choose it as the origin of our reference frame without loss of generality. Starting from the unperturbed Fermi sea $|\Psi_0\rangle$ and treating the light-matter part of the Hamiltonian

$$\hat{V}_{LM} = gA_L e^{-i\omega_L t} \hat{\psi}_X^\dagger + \text{h.c.}$$

as a perturbation to the Fermi sea, we need to go second order in this perturbation to have a first non-zero contribution to the density-density correlation function needed in the above expression. Using second order Kubo response theory we find for the electron-exciton density correlation function

$$\langle \hat{n}_e(\mathbf{r}, t) \hat{n}_X(\mathbf{0}, t) \rangle = |gA_L|^2 \int_{t_0}^t ds \int_{t_0}^s d\tau \left[e^{i\omega_L(s-\tau)} \langle \Psi_0 | \hat{\psi}_X(\mathbf{0}, s) \hat{n}_e(\mathbf{r}, t) \hat{n}_X(\mathbf{0}, t) \hat{\psi}_X^\dagger(\mathbf{0}, \tau) | \Psi_0 \rangle + \text{h.c.} \right] \quad (\text{C.1})$$

Here, the time t_0 is the time at which the perturbation has been switched on.

Using the interaction picture for the time evolution of the operators we obtain

$$\langle \Psi_0 | \hat{\psi}_X(\mathbf{0}, s) \hat{n}_e(\mathbf{r}, t) \hat{n}_X(\mathbf{0}, t) \hat{\psi}_X^\dagger(\mathbf{0}, \tau) | \Psi_0 \rangle = e^{iE_0(s-\tau)} \langle \Psi_0 | e^{-i\bar{H}s} \hat{\psi}_e^\dagger(\mathbf{r}, t) \hat{\psi}_e(\mathbf{r}, t) e^{i\bar{H}\tau} | \Psi_0 \rangle,$$

where \bar{H} is the Hamiltonian governing the dynamics of the electrons in presence of the exciton scattering potential and E_0 is the ground state energy of the Fermi sea without the exciton.

Using the Fourier transform for the system enclosed in a box of area S , we obtain

$$\langle \Psi_0 | e^{-i\bar{H}s} \hat{\psi}_e^\dagger(\mathbf{r}, t) \hat{\psi}_e(\mathbf{r}, t) e^{i\bar{H}\tau} | \Psi_0 \rangle = \frac{1}{S} \sum_{\mathbf{k}, \mathbf{q}} e^{i(\mathbf{k}-\mathbf{q})\mathbf{r}} \langle \Psi_0 | e^{-i\bar{H}s} \hat{c}_{\mathbf{k}}^\dagger(t) \hat{c}_{\mathbf{q}}(t) e^{i\bar{H}\tau} | \Psi_0 \rangle,$$

where the plane wave creation operators satisfy $\{\hat{c}_{\mathbf{k}}, \hat{c}_{\mathbf{q}}^\dagger\} = \delta_{\mathbf{k}, \mathbf{q}}$. The time evolution of the operators is governed by the Hamiltonian in presence of the exciton:

$$\bar{H} = \sum_{\mathbf{k}} \varepsilon_{\mathbf{k}} \hat{c}_{\mathbf{k}}^\dagger \hat{c}_{\mathbf{k}} + \sum_{\mathbf{k}, \mathbf{k}'} V_{\mathbf{k}\mathbf{k}'}^{X-e} \hat{c}_{\mathbf{k}'}^\dagger \hat{c}_{\mathbf{k}}.$$

The eigenstates are no longer plane waves and we therefore make a unitary transformation from the plane wave basis to the basis of eigenstates of \bar{H} . The latter are characterized by their principal quantum number n and the angular momentum l , because the scattering potential under consideration is spheric symmetric.

$$\begin{aligned} & \frac{1}{S} \sum_{\mathbf{k}, \mathbf{q}} e^{i(\mathbf{k}-\mathbf{q})\mathbf{r}} \langle \Psi_0 | e^{-i\bar{H}s} \hat{c}_{\mathbf{k}}^\dagger(t) \hat{c}_{\mathbf{q}}(t) e^{i\bar{H}\tau} | \Psi_0 \rangle \\ &= \frac{1}{S} \sum_{\mathbf{k}, \mathbf{q}} e^{i(\mathbf{k}-\mathbf{q})\mathbf{r}} \sum_{n,m=0}^{\infty} \sum_{l,p=-\infty}^{\infty} \langle \mathbf{q} | n, l \rangle \langle m, p | \mathbf{k} \rangle \langle \text{FS} | e^{-i\bar{H}s} c_{mp}^\dagger(t) \hat{c}_{nl}(t) e^{i\bar{H}\tau} | \text{FS} \rangle. \end{aligned}$$

Since the Hamiltonian \bar{H} is diagonal in the operators \hat{c}_{nl}^\dagger we have a trivial time evolution. We further obtain

$$\begin{aligned} & \frac{1}{S} \sum_{\mathbf{k}, \mathbf{q}} e^{i(\mathbf{k}-\mathbf{q})\mathbf{r}} \sum_{n,m=0}^{\infty} \sum_{l,p=-\infty}^{\infty} \langle \mathbf{q} | n, l \rangle \langle m, p | \mathbf{k} \rangle \langle \Psi_0 | e^{-i\bar{H}s} c_{mp}^\dagger(t) \hat{c}_{nl}(t) e^{i\bar{H}\tau} | \Psi_0 \rangle \\ &= \frac{1}{S} \sum_{\mathbf{k}, \mathbf{q}} e^{i(\mathbf{k}-\mathbf{q})\mathbf{r}} \sum_{n,m=0}^{\infty} e^{i\bar{\epsilon}_m t} e^{-i\bar{\epsilon}_n t} \sum_{l,p=-\infty}^{\infty} \langle \mathbf{q} | n, l \rangle \langle m, p | \mathbf{k} \rangle \langle \Psi_0 | e^{-i\bar{H}s} \hat{c}_{mp}^\dagger \hat{c}_{nl} e^{i\bar{H}\tau} | \Psi_0 \rangle \\ &= \frac{1}{S} \sum_{\mathbf{k}, \mathbf{q}} e^{i(\mathbf{k}-\mathbf{q})\mathbf{r}} \sum_{n,m=0}^{\infty} e^{i\bar{\epsilon}_m t} e^{-i\bar{\epsilon}_n t} \sum_{l,p=-\infty}^{\infty} \langle \mathbf{q} | n, l \rangle \langle m, p | \mathbf{k} \rangle \langle \Psi_0 | e^{-i\bar{H}s} \hat{c}_{mp}^\dagger e^{i\bar{H}s} e^{-i\bar{H}(s-\tau)} e^{-i\bar{H}\tau} \hat{c}_{nl} e^{i\bar{H}\tau} | \Psi_0 \rangle \\ &= \frac{1}{S} \sum_{\mathbf{k}, \mathbf{q}} e^{i(\mathbf{k}-\mathbf{q})\mathbf{r}} \sum_{n,m=0}^{\infty} e^{i\bar{\epsilon}_m t} e^{-i\bar{\epsilon}_n t} \sum_{l,p=-\infty}^{\infty} \langle \mathbf{q} | n, l \rangle \langle m, p | \mathbf{k} \rangle \langle \Psi_0 | \hat{c}_{mp}^\dagger(-s) e^{-i\bar{H}(s-\tau)} \hat{c}_{nl}(-\tau) | \Psi_0 \rangle \\ &= \frac{1}{S} \sum_{\mathbf{k}, \mathbf{q}} e^{i(\mathbf{k}-\mathbf{q})\mathbf{r}} \sum_{n,m=0}^{\infty} e^{i\bar{\epsilon}_m t} e^{-i\bar{\epsilon}_n t} e^{-i\bar{\epsilon}_m s} e^{i\bar{\epsilon}_n \tau} \sum_{l,p=-\infty}^{\infty} \langle \mathbf{q} | n, l \rangle \langle m, p | \mathbf{k} \rangle \langle \Psi_0 | \hat{c}_{mp}^\dagger e^{-i\bar{H}(s-\tau)} \hat{c}_{nl} | \Psi_0 \rangle, \end{aligned}$$

where in the third line we introduced the unit operator. The initial state $|\Psi_0\rangle$ is built with plane waves, labelled with the linear momentum \mathbf{k} as quantum number. But the operator \hat{c}_{nl} destroys a scattering state. We therefore make again a transformation from scattering states to plane wave states, yielding

$$\begin{aligned} & \langle \Psi_0 | e^{-i\bar{H}s} \psi_e^\dagger(\mathbf{r}, t) \psi_e(\mathbf{r}, t) e^{i\bar{H}\tau} | \Psi_0 \rangle \\ &= \frac{1}{S} \sum_{\mathbf{k}, \mathbf{q}} e^{i(\mathbf{k}-\mathbf{q})\mathbf{r}} \sum_{n,m=0}^{\infty} e^{i\bar{\epsilon}_m t} e^{-i\bar{\epsilon}_n t} e^{-i\bar{\epsilon}_m s} e^{i\bar{\epsilon}_n \tau} \\ & \quad \times \sum_{l,p=-\infty}^{\infty} \langle \mathbf{q} | n, l \rangle \langle m, p | \mathbf{k} \rangle \sum_{\mathbf{K}, \mathbf{Q}} \langle n, l | \mathbf{K} \rangle \langle \mathbf{Q} | m, p \rangle \langle \Psi_0 | \hat{c}_{\mathbf{Q}}^\dagger e^{-i\bar{H}(s-\tau)} \hat{c}_{\mathbf{K}} | \Psi_0 \rangle. \end{aligned}$$

The sum over \mathbf{k}, \mathbf{q} defines the wave function in position space. Writing $\langle \mathbf{k} | n, l \rangle = \phi_{nl}(\mathbf{k})$, the eigenstates of the Hamiltonian \bar{H} in plane wave basis, we define

$$\phi_{nl}(\mathbf{r}) = \frac{1}{\sqrt{S}} \sum_{\mathbf{k}} e^{-i\mathbf{k}\mathbf{r}} \phi_{nl}(\mathbf{k}),$$

and we finally obtain

$$\begin{aligned}
& \langle \Psi_0 | \hat{\psi}_X(\mathbf{0}, s) \hat{n}_e(\mathbf{r}, t) \hat{n}_X(\mathbf{0}, t) \hat{\psi}_X^\dagger(\mathbf{0}, \tau) | \Psi_0 \rangle \\
&= e^{iE_0(s-\tau)} \langle \Psi_0 | e^{-i\bar{H}s} \hat{\psi}_e^\dagger(\mathbf{r}, t) \hat{\psi}_e(\mathbf{r}, t) e^{i\bar{H}\tau} | \Psi_0 \rangle \\
&= \sum_{n,m=0}^{\infty} \sum_{l,p=-\infty}^{\infty} \phi_{nl}(\mathbf{r}) \phi_{mp}^*(\mathbf{r}) e^{i\bar{\epsilon}_m t} e^{-i\bar{\epsilon}_n t} e^{-i\bar{\epsilon}_m s} e^{i\bar{\epsilon}_n \tau} \sum_{\mathbf{K}, \mathbf{Q}} \phi_{nl}^*(\mathbf{K}) \phi_{mp}(\mathbf{Q}) \langle \Psi_0 | \hat{c}_{\mathbf{Q}}^\dagger e^{-i(\bar{H}-E_0)(s-\tau)} \hat{c}_{\mathbf{K}} | \Psi_0 \rangle \\
&= \sum_{n,m=0}^{\infty} \sum_{l,p=-\infty}^{\infty} \phi_{nl}(\mathbf{r}) \phi_{mp}^*(\mathbf{r}) e^{i\bar{\epsilon}_m t} e^{-i\bar{\epsilon}_n t} e^{-i\bar{\epsilon}_m s} e^{i\bar{\epsilon}_n \tau} g_{nm}(s-\tau).
\end{aligned}$$

Here, we introduced shorthand notation for the double sum over \mathbf{K}, \mathbf{Q} (dropping the angular momentum indices in order not to overload the notation):

$$g_{nm}(t) = \sum_{\mathbf{K}, \mathbf{Q}} \phi_{nl}^*(\mathbf{K}) \phi_{mp}(\mathbf{Q}) \langle \Psi_0 | \hat{c}_{\mathbf{Q}}^\dagger e^{-i(\bar{H}-E_0)t} \hat{c}_{\mathbf{K}} | \Psi_0 \rangle.$$

The above expectation value should be plugged into equation (C.1). This gives

$$\begin{aligned}
& \langle \hat{n}_e(\mathbf{r}, t) \hat{n}_X(\mathbf{0}, t) \rangle \\
&= |gA_L|^2 \sum_{n,m=0}^{\infty} \sum_{l,p=-\infty}^{\infty} \phi_{nl}(\mathbf{r}) \phi_{mp}^*(\mathbf{r}) e^{i\bar{\epsilon}_m t} e^{-i\bar{\epsilon}_n t} \int_{t_0}^t ds \int_{t_0}^s d\tau e^{i\omega_L(s-\tau)} e^{-i\bar{\epsilon}_m s} e^{i\bar{\epsilon}_n \tau} g_{nm}(s-\tau) + \text{h.c.}
\end{aligned}$$

The hermitian conjugate term can be shown to be the same as interchanging s and τ , yielding

$$\begin{aligned}
& \langle \hat{n}_e(\mathbf{r}, t) \hat{n}_X(\mathbf{0}, t) \rangle \\
&= |gA_L|^2 \sum_{n,m=0}^{\infty} \sum_{l,p=-\infty}^{\infty} \phi_{nl}(\mathbf{r}) \phi_{mp}^*(\mathbf{r}) e^{i\bar{\epsilon}_m t} e^{-i\bar{\epsilon}_n t} \int_{t_0}^t ds \int_{t_0}^t d\tau e^{i\omega_L(s-\tau)} e^{-i\bar{\epsilon}_m s} e^{i\bar{\epsilon}_n \tau} g_{nm}(s-\tau),
\end{aligned}$$

where now we can both have $s < \tau$ and $s > \tau$. Introducing the Fourier transformation of g_{nm} , we can now easily do the integration over s, τ . Furthermore, in order to obtain the stationary state under the continuous excitation, we add a small exponential term, meaning we slowly (for example, as compared to the lifetime of the cavity mode) turn on the laser. If we then take $t_0 \rightarrow -\infty$, this will eliminate all transient behaviour, originating from the initial time t_0 . In other words, we do not want our result to depend on t_0 .

So, introducing the Fourier transformed pair for a function $\varrho(t)$,

$$\begin{aligned}
\rho(t) &= \int_{-\infty}^{\infty} d\omega e^{-i\omega t} \varrho(\omega) \\
\varrho(\omega) &= \frac{1}{2\pi} \int_{-\infty}^{\infty} dt e^{i\omega t} \rho(t),
\end{aligned}$$

we obtain, by adiabatically turning on the laser (only focus on the time integrals)

$$\begin{aligned}
& e^{i\bar{\epsilon}_m t} e^{-i\bar{\epsilon}_n t} \lim_{\eta \rightarrow 0^+} \lim_{t_0 \rightarrow -\infty} \int_{t_0}^t ds e^{\eta^+ s} \int_{t_0}^t d\tau e^{\eta^+ \tau} e^{i\omega_L(s-\tau)} e^{-i\bar{\epsilon}_m s} e^{i\bar{\epsilon}_n \tau} \int_{-\infty}^{\infty} d\omega e^{-i\omega(s-\tau)} g_{nm}(\omega) \\
&= e^{i\bar{\epsilon}_m t} e^{-i\bar{\epsilon}_n t} \lim_{\eta \rightarrow 0^+} \lim_{t_0 \rightarrow -\infty} \int_{-\infty}^{\infty} d\omega g_{nm}(\omega) \int_{t_0}^t ds e^{\eta^+ s} \int_{t_0}^t d\tau e^{\eta^+ \tau} e^{i\omega_L(s-\tau)} e^{-i\bar{\epsilon}_m s} e^{i\bar{\epsilon}_n \tau} e^{-i\omega(s-\tau)} \\
&= \int_{-\infty}^{\infty} d\omega g_{nm}(\omega) \frac{1}{\omega - (\omega_L - \bar{\epsilon}_m)} \frac{1}{\omega - (\omega_L - \bar{\epsilon}_n)}.
\end{aligned}$$

The last line follows from straightforward integration and taking the proper limits. Restoring the double sum over n, m , we obtain equation (4.12b). The exciton density can be calculated completely analogously.

Nederlandstalige samenvatting

Dit theoretische werk onderzoekt de sterke licht-materie koppeling tussen een optische mode in een microcaviteit en een ingebedde, gedopeerde kwantumput. In het bijzonder worden de eigenschappen van de resulterende quasideeltjes, het (exciton of trion)-polariton dat een coherente superpositie is van een foton en een exciton (trion), onderzocht als functie van de elektronendichtheid. Gedurende het laatste decennium hebben polaritonen veel aandacht gekregen omwille van hun sterke optische niet-lineariteit en hun bosonisch karakter. Sinds het experiment waarin een Bose-Einstein condensaat van polaritonen werd gerealiseerd, een echte mijlpaal in de polariton fysica, is er veel vooruitgang geboekt in de superfluïde eigenschappen van polaritonen. Meer recent wordt de mogelijkheid onderzocht om met polaritonen kwantum informatie over te brengen, alsook de mogelijkheid om met microcaviteit polaritonen een single-foton laser te construeren. De thesis focust enkel op de lineaire eigenschappen van de polaritonen, dit wil zeggen dat polariton-polariton interacties buiten beschouwing worden gelaten.

In het eerste inleidende hoofdstuk wordt een historisch overzicht gegeven van de vele mogelijkheden om sterke licht-materie koppeling te realiseren. We geven ook een overzicht van welk soort experimenten er uitgevoerd zijn om de polaritonen te karakteriseren. De basisconcepten en relevante grootheden worden geïntroduceerd om later met meer geavanceerde berekeningen overweg te kunnen. De microcaviteit, de kwantumput en zijn elementaire excitaties (het exciton en trion) worden uitgelegd. Het exciton-polariton als een gekoppeld twee-niveau systeem wordt ook kort gepresenteerd. Dan leggen we de focus op het toevoegen van elektronen in de kwantumput, waarbij verscheidene veeldeeltjeseffecten, zoals de Fermi-edge-singulariteit (FES) en Anderson Orthogonaliteits Katastrofe (AOK), worden ingeleid om dit werk te motiveren. Hoofdstuk 2 onderzoekt de polaritonen die het resultaat zijn van de sterke koppeling tussen een optische mode en een sterk gedopeerde kwantumput die een kwantum ontaard tweedimensionaal elektronengas (2DEG) bevat. Met sterk gedopeerd bedoelen we dat de gemiddelde afstand tussen de elektronen kleiner is dan de exciton Bohr straal. De minst eenvoudige stap in het beschrijven van de lineaire eigenschappen van de polaritonen is het berekenen van de optische eigenschappen van het tweedimensionaal elektronengas; door de absorptie van een foton worden een conductieband elektron en een valentieband gat gecreëerd. Het valentieband gat fungeert dan als een attractieve potentiaal voor alle elektronen. Binnen bepaalde benaderingen berekenen we de optische susceptibiliteit van het 2DEG, waarbij we de bovenvernoemde FES en AOK mee in rekening nemen. In een tweede stap koppelen we de kwantumput met het elektromagnetisch veld. De resulterende eigenmodes van het gekoppelde systeem worden berekend en de ééndeeltjeseigenschappen, zoals de effectieve massa en de Rabi frequentie van de polaritonen wordt onderzocht.

Eén van de belangrijkste aannames in het tweede hoofdstuk is dat het valentieband gat een oneindig grote massa heeft. Dit is in het algemeen niet waar en we gebruiken een perturbatieve berekening in hoofdstuk 3 om deze eindige massa in rekening te brengen. We introduceren het Mahan exciton en we berekenen een laagste orde bijdrage in de Lindhard polariseerbaarheid van het 2DEG voor de levensduur van het Mahan polariton. Zelfs zonder rekening te houden met de eindige massa van het gat, zullen de resultaten van dit hoofdstuk accuraat zijn indien de Fermi tijd groter is dan de periode van de Rabi oscillaties.

Wanneer de elektronendichtheid verlaagd wordt, zal er een regime zijn waarbij de gemiddelde afstand tussen de elektronen groter wordt dan de exciton Bohr straal. Het exciton kan dan beschreven worden als een bosonisch deeltje waaraan de elektronen kunnen verstrooien. Hoofdstuk 4 introduceert deze effectieve beschrijving van het exciton en het trion quasideeltje als een elektron gebonden aan het exciton. Opnieuw wordt de 2DEG optische susceptibiliteit berekend binnen dit model en we onderzoeken het trion-polariton, de coherente superpositie van de optische mode en het trion in de kwantumput. We zullen aantonen dat dit model verschillende experimenteel observeerbare resultaten produceert, zoals de transfer van oscillatorsterkte en asymmetrische lijnvormen. In het bijzonder zullen we ons richten op de ruimtelijke structuur (de grootte) van de trion component in de trion-foton superpositie als functie van Fermi energie en Rabi frequentie. Dit laatste is een belangrijke grootte die zinvol is om toekomstig onderzoek te doen naar polariton-polariton interacties, waar werd aangetoond dat de elektronen de interactie-sterkte tussen polaritonen zou kunnen vergroten. Door de grootte van het trion te berekenen, kunnen we een eerste afchatting maken van hoe polaritonen kunnen interageren in aanwezigheid van een 2DEG.

Bibliography

- [1] E. M. Purcell, H. C. Torrey, and R. V. Pound, *Phys. Rev.* **69**, 37 (1946).
- [2] J. J. Hopfield, *Phys. Rev.* **112**, 1555 (1958).
- [3] D. D. Sell, S. E. Stokowski, R. Dingle, and J. V. DiLorenzo, *Phys. Rev. B* **7**, 4568 (1973).
- [4] G. Rempe, H. Walther, and N. Klein, *Phys. Rev. Lett.* **58**, 353 (1987).
- [5] R. J. Thompson, G. Rempe, and H. J. Kimble, *Phys. Rev. Lett.* **68**, 1132 (1993).
- [6] Jean-Michel Raimond and Serge Haroche. *Exploring the quantum: atoms, cavities and photons*. Oxford University Press, 2006.
- [7] C. Weisbuch, M. Nishioka, A. Ishikawa, and Y. Arakawa, *Phys. Rev. Lett.* **69**, 3314 (1992).
- [8] E. Wertz, L. Ferrier, D. D. Solnyshkov, R. Johne, D. Sanvitto, A. Lemaître, I. Sagnes, R. Grousson, A. V. Kavokin, P. Senellart, G. Malpuech and J. Bloch, *Nat. Phys.* **6**, 860–864 (2010).
- [9] A. Trichet, E. Durupt, F. Médard, S. Datta, A. Minguzzi, and M. Richard, *Phys. Rev. B* **88**, 121407(R).
- [10] D. Bajoni, P. Senellart, E. Wertz, I. Sagnes, A. Miard, A. Lemaître, and J. Bloch, *Phys. Rev. Lett.* **100**, 047401 (2008).
- [11] A. Badolato, M. Winger, K. J. Hennessy, E. L. Hu, and A. Imamoglu, *C. R. Physique* **9**, 850–856 (2008).
- [12] A. Blais, R. Huang, A. Wallraff, S. M. Girvin and R. J. Schoelkopf, *Phys. Rev. A* **69**, 062320 (2004).
- [13] D. I. Schuster, A. A. Houck, J. A. Schreier, A. Wallraff, J. M. Gambetta, A. Blais, L. Frunzio, J. Majer, B. R. Johnson, M. H. Devoret, S. M. Girvin, and R. J. Schoelkopf. *Nature (London)* **445**, 515 (2007).
- [14] D. G. Lidzey, D. D. C. Bradley, T. Virgili, A. Armitage, M. S. Skolnick, and S. Walker, *Phys. Rev. Lett.* **82**, 3316 (1999).
- [15] A. I. Tartakovskii, M. Emam-Ismael, D. G. Lidzey, M. S. Skolnick, D. D. C. Bradley, S. Walker, and V. M. Agranovich, *Phys. Rev. B* **63**, 121302(R) (2001).
- [16] R. Balili, B. Nelsen, D. W. Snoke, R. H. Reid, L. Pfeiffer, and K. West, *Phys. Rev. B* **81**, 125311 (2010).
- [17] A. Gabbay, Y. Preezant, E. Cohen, B. M. Ashkinadze, and L. N. Pfeiffer, *Phys. Rev. Lett.* **99**, 157402 (2007).

- [18] D. Bajoni, M. Perrin, P. Senellart, A. Lemaître, B. Sermage, and J. Bloch, *Phys. Rev. B* **73**, 205344 (2006).
- [19] L. Nguyen-thê, S. De Liberato, M. Bamba, and C. Ciuti, *Phys. Rev. B* **87**, 235322 (2013).
- [20] S. Smolka, W. Wuester, F. Haupt, S. Faelt, W. Wegscheider, and A. Imamoglu, *Science* **346**, 332 (2014).
- [21] P. Bhattacharya, A. Das, S. Bhowmick, M. Jankowski, and Chi-sen Lee, *Appl. Phys. Lett.* **100**, 171106 (2012).
- [22] D. Tanese, H. Flayac, D. Solnyshkov, A. Amo, A. Lemaître, E. Galopin, R. Braive, P. Senellart, I. Sagnes, G. Malpuech, and J. Bloch, *Nat. Comm.* **4**, 1749 (2013).
- [23] C. Ciuti, V. Savona, C. Piermarocchi, A. Quattropani, and P. Schwendimann, *Phys. Rev. B* **58**, 7926 (1998).
- [24] G. Rochat, C. Ciuti, V. Savona, C. Piermarocchi, A. Quattropani, and P. Schwendimann, *Phys. Rev. B* **61**, 13856 (2000).
- [25] M. Vladimirova, S. Cronenberger, D. Scalbert, K. V. Kavokin, A. Miard, A. Lemaître, J. Bloch, D. Solnyshkov, G. Malpuech, and A. V. Kavokin, *Phys. Rev. B* **82**, 075301 (2010).
- [26] A. Amo, J. Lefrère, S. Pigeon, C. Adrados, C. Ciuti, I. Carusotto, R. Houdré, E. Giacobino, and A. Bramati, *Nat. Phys.* **5**, 805 - 810 (2009).
- [27] K. G. Lagoudakis, M. Wouters *et. al.*, *Nat. Phys.* **4**, 706-710 (2008).
- [28] W. Langbein, *Phys. Rev. B* **70**, 205301 (2004).
- [29] D. Bajoni, E. Peter, P. Senellart, J. L. Smirr, I. Sagnes, A. Lemaître and J. Bloch, *Appl. Phys. Lett.* **90**, 051107 (2007).
- [30] J. Kasprzak, M. Richard, S. Kundermann, A. Baas, P. Jeambrun, J. M. J. Keeling, F. M. Marchetti, M. H. Szymanski, R. André, J. L. Staehli, V. Savona, P. B. Littlewood, B. Deveaud and Le Si Dang, *Nature* **443**, 409-414 (2006).
- [31] I. Carusotto and C. Ciuti, *Rev. Mod. Phys.* **85**, 299 (2013).
- [32] A. Verger, C. Ciuti, and I. Carusotto, *Phys. Rev. B* **73**, 193306 (2006).
- [33] N. Takemura, S. Trebaol, M. Wouters, M. T. Portella-Oberli, and B. Deveaud, *Nat. Phys.* **10**, 500 (2014).
- [34] T. C. H. Liew and V. Savona, *Phys. Rev. Lett.* **104**, 183601 (2010).
- [35] Ferruccio Pisanello. Single Photon Sources Based on Colloidal Nanocrystals and Two Photon Polariton Laser. Atomic Physics. Université Pierre et Marie Curie - Paris VI, 2011.
- [36] M. Hofmann, D. Karaiskaj, C. Ellmers, T. Maxisch, F. Jahnke, H.-J. Kolbe, G. Weiser, R. Rettig, S. Leu, W. Stolz, S. W. Koch, and W. W. Rühle, *Phys. Stat. Sol. (a)* **178**, 179 (2000).
- [37] H. Deng, D. Snoke, J. Bloch, Y. Yamamoto, *Proc. Natl. Acad. Sci. U.S.A.* **100**, 15318 (2003).
- [38] R. Balili, V. Hartwell, D.W. Snoke, L. Pfeiffer and K. West, *Science* **316**, 5827 (2007).

- [39] B. R. Nag, *Physics of Quantum Well Devices*, Kluwer Academic Publishers, 2000.
- [40] B. Zaslav and M. E. Zandler, *Am. J. Phys.* **35**, 1118 (1967).
- [41] W. Martienssen and H. Warlimont, *Handbook of Condensed Matter and Materials Data*, Springer 2005.
- [42] A. I. Tartakovskii, D. N. Krizhanovskii, and V. D. Kulakovskii, *Phys. Rev. B* **62**, R13298(R) (2000).
- [43] R. M. Stevenson, V. N. Astratov, M. S. Skolnick, D. M. Whittaker, M. Emam-Ismael, A. I. Tartakovskii, P. G. Savvidis, J. J. Baumberg, and J. S. Roberts, *Phys. Rev. Lett.* **85**, 3680 (2000).
- [44] V. Savona, C. Piermarocchi, A. Quattropani, P. Schwendimann, and F. Tassone, *Optical properties of microcavity polaritons. Phase Transitions* **68**(1), 169–279 (1999).
- [45] J. C. Slater, *Phys. Rev.* **34**, 1293 (1929).
- [46] G. D. Mahan, *Phys. Rev.* **153**, 882 (1967).
- [47] G. D. Mahan, *Phys. Rev. Lett.* **18**, 448 (1967).
- [48] M. Combescot and P. Nozières, *Le Journal de Physique* **32**, 913 (1971).
- [49] P. Nozières and C. T. De Dominicis, *Phys. Rev.* **178**, 1097 (1969).
- [50] K. D. Schotte and U. Schotte, *Phys. Rev.* **182**, 479 (1969).
- [51] K. Ohtake and Y. Tanabe, *Rev. Mod. Phys.* **62**, 929 (1990).
- [52] M. S. Skolnick, J. M. Rorison, K. J. Nash, D. J. Mowbray, P. R. Tapster, S. J. Bass, and A. D. Pitt, *Phys. Rev. Lett.* **58**, 2130 (1987).
- [53] M. Knap, A. Shashi, Y. Nishida, A. Imambekov, D. A. Abanin, and E. Demler, *Phys. Rev. X* **2**, 041020 (2012).
- [54] G. Refael and E. Demler, *Phys. Rev. B* **77**, 144511 (2008).
- [55] A. Schirotzek, C. H. Wu, A. Sommer, and M. W. Zwierlein, *Phys. Rev. Lett.* **102**, 230402 (2009).
- [56] M. A. Lampert, *Phys. Rev. Lett.* **1**, 450 (1958).
- [57] K. Kheng, R. T. Cox, Y. Merle d’Aubigné, F. Bassani, K. Saminadayar, and S. Tatarenko, *Phys. Rev. Lett* **71**, 1752 (1993).
- [58] G. Finkelstein, H. Shtrikman, and I. Bar-Joseph, *Phys. Rev. Lett.* **74**, 976 (1995).
- [59] A. J. Shields, M. Pepper, D. A. Ritchie, M. Y. Simmons, and G. A. C. Jones, *Phys. Rev. B* **51**, 18049(R) (1995).
- [60] B. Stébé, G. Munschy, L. Stauffer, F. Dujardin and J. Murat, *Phys. Rev. B* **56**, 456 (1997).
- [61] C. Riva, F. M. Peeters, and K. Varga, *Phys. Rev. B* **61**, 873 (2000).
- [62] M. Combescot, O. Betbeder-Matibet, *Sol. State. Comm.* **126**, 687-691 (2003).

- [63] M. Combescot, O. Betbeder-Matibet, and F. Dubin, *Eur. Phys. J. B* **42**, 63-83 (2004).
- [64] P. G. Lagoudakis, M. D. Martin, J. J. Baumberg, A. Qarry, E. Cohen, and L. N. Pfeiffer, *Phys. Rev. Lett.* **90**, 206401 (2003).
- [65] M. Perrin, P. Senellart, A. Lemaître, and J. Bloch, *Phys. Rev. B* **72**, 075340 (2005).
- [66] A. Das, B. Xiao, S. Bhowmick, and P. Bhattacharya, *Appl. Phys. Lett.* **101**, 131112 (2012).
- [67] G. Malpuech, A. Kavokin, A. Di Carlo, and J. J. Baumberg, *Phys. Rev. B* **65**, 153310 (2002).
- [68] F. P. Laussy, A. V. Kavokin, and I. A. Shelykh, *Phys. Rev. Lett.* **104**, 106402 (2010).
- [69] R. Kubo, *Journal of the Physical Society of Japan* **12**, 570–586 (1957).
- [70] P. Anderson, *Phys. Rev. Lett.* **18**, 1049 (1967).
- [71] P. Hawrylak, *Phys. Rev. B* **44**, 3821 (1991).
- [72] G. D. Mahan, *Many-Particle Physics Third Edition*, Kluwer Academic/Plenum Publishers, 2000.
- [73] R. J. Elliott, *Phys. Rev.* **108**, 1384 (1957).
- [74] K. Chadan, N. N. Khuri, A. Martin, and T. T. Wu, *J. Math. Phys.* **44**, 406 (2003).
- [75] K. Yang and M. de Llano, *Am. J. Phys.* **57**, 85 (1989).
- [76] J. Friedel, *Comments Solid State Phys.* **2**, 40 (1969).
- [77] N. S. Averkiev and M. M. Glazov, *Phys. Rev. B* **76**, 045320 (2007).
- [78] D. S. Citrin and J. B. Khurgin, *Phys. Rev. B* **68**, 205325 (2003).
- [79] J. Gavoret, P. Nozières, B. Roulet, M. Combescot, *J. Phys. France* **30**, 987 (1969).
- [80] P. Nozières, *J. Phys. I France* **4**, 1275-1280 (1994).
- [81] T. Uenoyama and L. J. Sham, *Phys. Rev. Lett.* **65**, 1048 (1990).
- [82] A. Rosch and T. Kopp, *Phys. Rev. Lett.* **75**, 1988 (1995).
- [83] F. Stern, *Phys. Rev. Lett.* **18**, 546-548 (1967).
- [84] E. Burstein, *Phys. Rev.* **93**, 632 (1954).
- [85] T. S. Moss, *Proc. Phys. Soc. (London)* **B76**, 775 (1954).
- [86] A. E. Ruckenstein and S. Schmitt-Rink, *Phys. Rev. B*, **35**, 7551-7557 (1987).
- [87] H. Haug and S. W. Koch, *Quantum Theory of the Optical and Electronic Properties of Semiconductors*, World Scientific Publishing, Fourth ed.
- [88] N. d'Ambrumenil, and B. Muzykantskii, *Phys. Rev. B* **71**, 045326 (2005).
- [89] R. Rapaport, R. Harel, E. Cohen, Arza Ron, E. Linder, and L. N. Pfeiffer, *Phys. Rev. Lett.* **84**, 1607 (2000).
- [90] A. Imamoglu, H. Schmidt, G. Woods, and M. Deutsch, *Phys. Rev. Lett.* **79**, 1467 (1997).
- [91] K. Yamada and K. Yosida, *Prog. Theor. Phys.* **62**, No. 2, 1979.